Springer Proceedings in Physics 272

Kang-Ping Lin
Ren-Shyan Liu
Bang-Hung Yang *Editors*

Future Trends and Challenges of Molecular Imaging and AI Innovation

Proceedings of FASMI 2020

Springer

Springer Proceedings in Physics

Volume 272

Indexed by Scopus

The series Springer Proceedings in Physics, founded in 1984, is devoted to timely reports of state-of-the-art developments in physics and related sciences. Typically based on material presented at conferences, workshops and similar scientific meetings, volumes published in this series will constitute a comprehensive up-to-date source of reference on a field or subfield of relevance in contemporary physics. Proposals must include the following:

- name, place and date of the scientific meeting
- a link to the committees (local organization, international advisors etc.)
- scientific description of the meeting
- list of invited/plenary speakers
- an estimate of the planned proceedings book parameters (number of pages/articles, requested number of bulk copies, submission deadline).

Please contact:

For Americas and Europe: Dr. Zachary Evenson; zachary.evenson@springer.com
For Asia, Australia and New Zealand: Dr. Loyola DSilva; loyola.dsilva@springer.com

More information about this series at https://link.springer.com/bookseries/361

Kang-Ping Lin · Ren-Shyan Liu · Bang-Hung Yang
Editors

Future Trends and Challenges of Molecular Imaging and AI Innovation

Proceedings of FASMI 2020

Springer

Editors
Kang-Ping Lin
Department of Electrical Engineering
Chung Yuan Christian University (CYCU)
Taoyuan, Taiwan

Bang-Hung Yang
Department of Biomedical Imaging
and Radiological Sciences (BIRS)
National Yang Ming Chiao Tung University
(NYCU)
Taipei, Taiwan

Ren-Shyan Liu
Department of Nuclear Medicine
and Department of Biomedical Imaging
and Radiological Sciences (BIRS)
Cheng Hsin General Hospital and National
Yang Ming Chiao Tung University (NYCU)
Taipei, Taiwan

ISSN 0930-8989 ISSN 1867-4941 (electronic)
Springer Proceedings in Physics
ISBN 978-3-030-92785-1 ISBN 978-3-030-92786-8 (eBook)
https://doi.org/10.1007/978-3-030-92786-8

© The Editor(s) (if applicable) and The Author(s), under exclusive license to Springer Nature Switzerland AG 2022
This work is subject to copyright. All rights are solely and exclusively licensed by the Publisher, whether the whole or part of the material is concerned, specifically the rights of translation, reprinting, reuse of illustrations, recitation, broadcasting, reproduction on microfilms or in any other physical way, and transmission or information storage and retrieval, electronic adaptation, computer software, or by similar or dissimilar methodology now known or hereafter developed.
The use of general descriptive names, registered names, trademarks, service marks, etc. in this publication does not imply, even in the absence of a specific statement, that such names are exempt from the relevant protective laws and regulations and therefore free for general use.
The publisher, the authors and the editors are safe to assume that the advice and information in this book are believed to be true and accurate at the date of publication. Neither the publisher nor the authors or the editors give a warranty, expressed or implied, with respect to the material contained herein or for any errors or omissions that may have been made. The publisher remains neutral with regard to jurisdictional claims in published maps and institutional affiliations.

This Springer imprint is published by the registered company Springer Nature Switzerland AG
The registered company address is: Gewerbestrasse 11, 6330 Cham, Switzerland

Contents

Contributors

Najim Akhtar Institute of Biophotonics, National Yang Ming Chiao Tung University, Taipei, Taiwan

Hui-Wen Chan Department of Biomedical Imaging and Radiological Sciences, National Yang Ming Chiao Tung University, Taipei, Taiwan

Chi-Wei Chang Department of Nuclear Medicine and National PET/Cyclotron Center, Taipei Veterans General Hospital, Taipei, Taiwan

Chih-Hsien Chang Isotope Application Division, Institute of Nuclear Energy Research, Taoyuan, Taiwan

Deng-Yuan Chang Department of Biomedical Imaging and Radiological Sciences, National Yang Ming Chiao Tung University, Taipei, Taiwan

Teng-Bin Chang Department of Electrical Engineering, Chung Yuan Christian University, Taoyuan, Taiwan

Surojit Chattopadhyay Institute of Biophotonics, National Yang Ming Chiao Tung University, Taipei, Taiwan

Chao-Cheng Chen Department of Biomedical Imaging and Radiological Sciences, National Yang Ming Chiao Tung University, Taipei, Taiwan

Chuan Lin Chen Department of Biomedical Imaging and Radiological Sciences, National Yang Ming Chiao Tung University, Taipei, Taiwan

Ju-Yu Chen Department of Health Technology and Informatics, The Hong Kong Polytechnic University, Hong Kong, China

Mei-Fen Chen Department of Electrical Engineering, Chung Yuan Christian University, Taoyuan, Taiwan;
Technology Translation Center for Medical Device, Chung Yuan Christian University, Taoyuan, Taiwan

Ming-Wei Chen Isotope Application Division, Institute of Nuclear Energy Research, Taoyuan, Taiwan

Su-Jung Chen Isotope Application Division, Institute of Nuclear Energy Research, Taoyuan, Taiwan

Yi-An Chen Institute of Clinical Medicine, National Yang Ming Chiao Tung University, Taipei, Taiwan;
Molecular and Genetic Imaging Core, Mouse Clinic, National Comprehensive Mouse Phenotyping and Drug Testing Center, Taipei, Taiwan;
Department of Biomedical Imaging and Radiological Sciences, National Yang Ming Chiao Tung University, Taipei, Taiwan

Yi-Lun Chen Taipei Veterans General Hospital, National PET/Cyclotron Center and Department of Nuclear Medicine, Taipei, Taiwan;
Taipei Association of Radiological Technologists, Taipei, Taiwan

Chen-Han Cheng Institute of Nuclear Energy Research/Health Physics Division, Taoyuan, Taiwan

Hung-Wen Chiu Graduate Institute of Biomedical Informatics, Taipei Medical University, Taipei, Taiwan

Juri G. Gelovani Office of the Provost, United Arab Emirates University, Al Ain, United Arab Emirates

Sandip Ghosh Institute of Biophotonics, National Yang Ming Chiao Tung University, Taipei, Taiwan

Meilan Jimmy Hasugian Department of Electrical Engineering, Chung Yuan Christian University, Taoyuan, Taiwan

Wen-Sheng Huang Taipei Veterans General Hospital, National PET/Cyclotron Center and Department of Nuclear Medicine, Taipei, Taiwan

Yuan-Ruei Huang Isotope Application Division, Institute of Nuclear Energy Research, Taoyuan, Taiwan

Chien-Chih Ke Molecular and Genetic Imaging Core, Mouse Clinic, National Comprehensive Mouse Phenotyping and Drug Testing Center, Taipei, Taiwan;
Department of Medical Imaging and Radiological Sciences, Kaohsiung Medical University, Kaohsiung, Taiwan;
Department of Medical Research, Kaohsiung Medical University Hospital, Kaohsiung, Taiwan

Wing Sum Lau Department of Health Technology and Informatics, The Hong Kong Polytechnic University, Hong Kong, China

Shih-Ying Lee Isotope Application Division, Institute of Nuclear Energy Research, Taoyuan, Taiwan

Ming-Hsin Li Isotope Application Division, Institute of Nuclear Energy Research, Taoyuan, Taiwan

Hsin-Chin Liang Institute of Nuclear Energy Research/Health Physics Division, Taoyuan, Taiwan

Kang-Ping Lin Department of Electrical Engineering, Chung Yuan Christian University, Taoyuan, Taiwan;
Technology Translation Center for Medical Device, Chung Yuan Christian University, Taoyuan, Taiwan

Liang-Ting Lin Department of Health Technology and Informatics, The Hong Kong Polytechnic University, Hong Kong, China

Ren-Shyan Liu Program of Biomedical Science and Engineering, National Yang Ming Chiao Tung University, Taipei, Taiwan;
Institute of Clinical Medicine, National Yang Ming Chiao Tung University, Taipei, Taiwan;
Department of Biomedical Imaging and Radiological Sciences, National Yang Ming Chiao Tung University, Taipei, Taiwan;
Molecular and Genetic Imaging Core, Mouse Clinic, National Comprehensive Mouse Phenotyping and Drug Testing Center, Taipei, Taiwan;
Department of Nuclear Medicine, Cheng Hsin Hospital, Taipei, Taiwan;
Department of Nuclear Medicine and National PET/Cyclotron Center, Taipei Veterans General Hospital, Taipei, Taiwan

Sheng-Nan Lo Isotope Application Division, Institute of Nuclear Energy Research, Taoyuan, Taiwan

Shih-Wei Lo Isotope Application Division, Institute of Nuclear Energy Research, Taoyuan, Taiwan

Wei-Lin Lo Isotope Application Division, Institute of Nuclear Energy Research, Taoyuan, Taiwan

Cheng-Hsiu Lu Program of Biomedical Science and Engineering, National Yang Ming Chiao Tung University, Taipei, Taiwan;
Core Laboratory for Phenomics and Diagnostics, Kaohsiung Chang Gung Memorial Hospital, Kaohsiung, Taiwan;
Department of Medical Research, Kaohsiung Chang Gung Memorial Hospital, Kaohsiung, Taiwan

I-Ling Shih GE Healthcare, Taipei, Taiwan

Mao-Yuan Su Taipei Association of Radiological Technologists, Taipei, Taiwan;
Department of Medical Imaging, National Taiwan University Hospital, Taipei, Taiwan;
Department of Medical Imaging and Radiological Technology, Yuanpei University of Medical, Technology, Hsinchu, Taiwan

Wei-Fang Su Department of Materials Science and Engineering, National Taiwan University, Taipei, Taiwan;
Molecular Imaging Center, National Taiwan University, Taipei, Taiwan

Cheng-Chang Tsai Department of Materials Science and Engineering, National Taiwan University, Taipei, Taiwan

Cheng-Si Tsao Institute of Nuclear Energy Research, Longtan, Taoyuan, Taiwan

Yun-Hsiu Tseng Department of Materials Science and Engineering, National Taiwan University, Taipei, Taiwan

Hsin-Ell Wang Department of Biomedical Imaging and Radiological Sciences, National Yang Ming Chiao Tung University, Taipei, Taiwan

Shih-Min Wang Isotope Application Division, Institute of Nuclear Energy Research, Taoyuan, Taiwan

Hsiang-Ning Wu Institute of Nuclear Energy Research/Health Physics Division, Taoyuan, Taiwan

Ming-Chung Wu Department of Chemical and Materials Engineering, Chang-Gung University, Taoyuan, Taiwan

Ping-Yu Wu Department of Electrical Engineering, Chung Yuan Christian University, Taoyuan, Taiwan

Bang-Hung Yang Department of Nuclear Medicine and National PET/Cyclotron Center, Taipei Veterans General Hospital, Taipei, Taiwan;
Taipei Association of Radiological Technologists, Taipei, Taiwan;
Department of Biomedical Imaging and Radiological Sciences, National Yang Ming Chiao Tung University, Taipei, Taiwan

De-Ming Yang Microscopy Service Laboratory, Basic Research Division, Department of Medical Research, Taipei Veterans General Hospital, Taipei, Taiwan

Shun-Chung Yang Graduate Institute of Biomedical Informatics, Taipei Medical University, Taipei, Taiwan;
Taipei Association of Radiological Technologists, Taipei, Taiwan;
Department of Medical Imaging, National Taiwan University Hospital, Taipei, Taiwan

Tzu-Yi Yu Department of Materials Science and Engineering, National Taiwan University, Taipei, Taiwan

X-ray Tomography Study of 3D Hydrogel Structure

Cheng-Chang Tsai, Yun-Hsiu Tseng, and Wei-Fang Su

1 Introduction

There is a growing trend that millions of people suffer from glaucoma which is one of the neurodegenerative diseases [1]. The degeneration of optic nerves has limited regenerative capacity due to myelin and glial scar formation from lesion [2]. It is important to establish an efficient method to cure the optic nerve dysfunction. Neural tissue engineering is regarded as a hopeful method to transplant the cell containing a functional scaffold and restore the neural tissue function [3]. The optic nerve exhibits anisotropic hierarchical morphology to transmit the directional action potential signal [4]. Among the artificial biomimetic scaffolds used for neural tissue engineering, hydrogel is a preferred soft material because the 3D structure and water content are similar to the natural extracellular matrix (ECM) [5]. Also, the anisotropic structure is essential to the optic nerve due to the guidance of the neuron. Many methods have been developed to fabricate hydrogel with aligned structures such as self-assembled peptide and polymer under the magnetic field. For example, self-assembled peptide could be synthesized via solid-phase peptide synthesis with a precise peptide sequence [6–9]. However, the process is time-consuming, low yield, and high cost which limits the large-scale production. Then, the hydrogel made of magnetic responsive polymer combined with an external magnetic field is a non-invasive method [10–13]. However, the synthesis of polymer is complicated and the alignment of molecules using the cumbersome magnetic generator is not readily accessible. Herein, we propose to prepare self-assembly nanocomposite to obtain hydrogel with aligned structure. We first synthesized water-soluble

C.-C. Tsai · Y.-H. Tseng · W.-F. Su (✉)
Department of Materials Science and Engineering, National Taiwan University, Taipei, Taiwan
e-mail: suwf@ntu.edu.tw

W.-F. Su
Molecular Imaging Center, National Taiwan University, Taipei, Taiwan

© The Author(s), under exclusive license to Springer Nature Switzerland AG 2022

K.-P. Lin et al. (eds.), *Future Trends and Challenges of Molecular Imaging and AI Innovation*, Springer Proceedings in Physics 272,
https://doi.org/10.1007/978-3-030-92786-8_1

polypeptide containing the neurotransmitter of glutamate, named sodium salt of poly (γ-benzyl-L-glutamate)$_{40}$-r-poly (L-glutamic acid)$_{60}$ (PBGA60-Na). Then, it was used as a crosslinker to gel the cationic cellulose nanofibrils (CNF^+) to form nanocomposite hydrogel through static charge and hydrogen bonding. The hydrogel with anisotropic structure was fabricated under a shear force. The hydrogel prepared without shear force to exhibit isotropic structure served as a control in this study. The aligned morphology of hydrogel could be observed by polarized optical microscope, scanning electron microscope, and X-ray tomography analyses at different scales of size. Owing to the high transmission capacity and spatial resolution of synchrotron radiation, the X-ray tomography could be reconstructed the 3D structure of material in situ. As a result, this study describes the first example of using the X-ray tomography to precisely observe the hydrogel with the aligned structure, which could provide the useful information needed in the clinic application.

2 Materials and Methods

A. Materials

Chemicals used for synthesis including L-glutamic acid γ-benzyl ester (Sigma-Aldrich), triphosgene (Sigma-Aldrich), benzylamine (Alfa Aesar), dichloroacetic acid (DCA, Acros), 33 wt% hydrogen bromide (HBr) in acetic acid (Acros), sodium bicarbonate ($NaHCO_3$, Fisher Scientific), ethyl acetate (EA, Macron), dimethylformamide (DMF, Sigma-Aldrich), tetrahydrofuran (THF, Macron), diethyl ether (J. T. Baker), methanol (Macron), and hexane (Macron). Chemicals for instrument analysis included ruthenium tetroxide, 0.5% stabilized aqueous solution (RuO4, Polysciences Inc.), chloroform-d (Merck), and trifluoroacetic acid-d (Acros). Cationic cellulose nanofibrils were purchased from Cellulose Lab.

B. Nomenclature

The abbreviation of the polymers was shown as follows: poly (γ-benzyl-L-glutamate) (PBG), poly (α-L-glutamic acid) with 60 mol% of hydrolysis (PBGA60), sodium salt of PBGA60 (PBGA60-Na), and cationic cellulose nanofibrils (CNF^+). The crosslinker (PBGA60-Na) and CNF^+ were abbreviated as C and M, respectively. The prefix *iso-* represented the isotropic morphology of hydrogel. The anisotropic hydrogel and isotropic hydrogel with a composition of 1.0 wt% CNF^+ and 0.25 wt% PBGA60-Na were named as M(1.0)C(0.25) and iso-M(1.0)C(0.25), respectively.

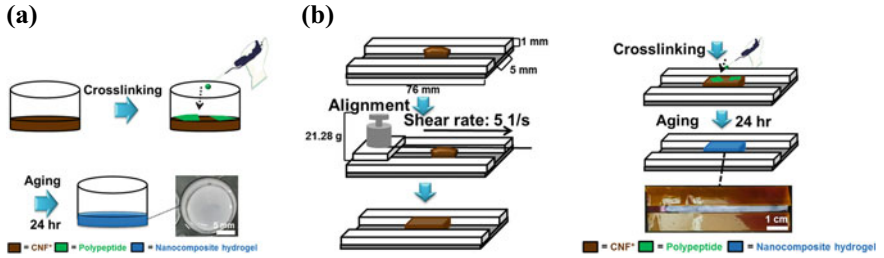

Fig. 1 Schematic diagram and actual sample diagram of **a** isotropic and **b** anisotropic hydrogel

C. Synthesis of PBGA60-Na

The PBGA60-Na was first prepared by a partial hydrolysis of PBG [14], and then a weak base treatment. The PBG (1 g) was dissolved in DCA (25 ml) first, and then adding HBr in acetic acid (33 wt%, 0.76 ml). After reacting at 31 °C for 2 h, the reaction solution was precipitated in cold ether, redissolved in THF, and recovered through precipitation in ether. The PBGA60 was purified five times from ether/THF cosolvent to obtain pure white solid, which was vacuum dried at 40 °C overnight (yield: 70%). The PBGA60 (0.2 g) was dissolved in $NaHCO_3$ solution (1 M, 6 ml) in a 25 ml two neck bottle. The solution was placed in dialysis membrane (MWCO 3500; Ordial D35; Orange Scientific) with deionized water to purify the polymer. The resulting product was freeze-dried at -53 °C by lyophilizer for two days to obtain a sponge-like white solid (yield: 88%).

D. Hydrogel preparation

For POM and SEM study, 100 μl of 1.0 wt% CNF^+ solution was placed in a 24 well plate first and then 100 μl of 0.25 wt% PBGA60-Na was added to the CNF^+ solution dropwise. The mixed solution was aged for 24 h to ensure complete gelation to prepare the isotropic hydrogel (iso-M(1.0)C(0.25)) by drop-casting as Fig. 1a shown. The anisotropic hydrogel (M(1.0)C(0.25)) was prepared by shear force shown as Fig. 1b. Two cover glasses (thickness ~ 1 mm) were pasted on each side of the glass substrate with a 5 mm wide groove between. 100 μl of 1.0 wt% CNF^+ solution was added in the groove. Shear the CNF^+ solution at 5 1/s shear rate under 21.28 g loading (Teflon piece and weight) to align CNF^+. 100 μl of 0.25 wt% PBGA60-Na was then added to the CNF^+ aligned solution dropwise throughout the CNF^+ solution. The mixed solution was aged for 24 h to ensure complete gelation. For the X-ray tomography study, only the halved volume (50 μl) of both PBGA60-Na and CNF^+ solution was needed for isotropic and anisotropic hydrogels.

E. Characterization of hydrogel morphology

The morphology of hydrogels at different scales was characterized using polarized optical microscope (POM, DM 2500 M, Leica), scanning electron microscope (SEM, JSM-6510, JEOL), and transmission X-ray microscope (TXM, NSRRC, Taiwan). For the POM study, the aqueous hydrogel sample was observed using cross-polar mode

at the magnification of 10x. For the SEM study, the hydrogel sample was frozen in liquid nitrogen for 1 min to fix the structure of the hydrogel and then was freeze-dried for three days to maintain the frozen structure. The dried samples were fixed on the holder by carbon tape and coated with platinum (60 s, 20 mA) to operate at 10 kV and 10 mm working distance between lens and sample. For the X-ray tomography study, the aqueous hydrogel sample was stained with 0.1% w/v ruthenium tetroxide in ddH_2O to enhance the contrast of the hydrogels. After 3 h of staining, the sample was washed with methanol. Tear off a piece of hydrogel with a thickness of about 14 ~ 17 μm to fix on the holder by polyamide tape. 20 μl gold particle solution (400 ~ 500 nm) was added to the hydrogel as the target of the rotation. The sample was rotated from -75˚ to 75˚. The 3D structure was reconstructed by computer simulation through 151 cross-section images taken per degree by TXM.

F. Statistical analysis of the alignment of the hydrogel

The azimuth angle of each fibril was counted in the same direction to get the angle distribution from -90˚ to 90˚ by ImageJ. The average azimuth angle was redefined as 0˚ to represent the direction of shear force. The alignment of anisotropic hydrogels can be determined by the azimuth angle distribution of the cellulose fibrils in POM images (n = 50) and TXM cross-section images (n = 10 at -75˚, -50˚, -25˚, 0˚, 25˚, 50˚, 75˚).

3 Results

The morphology of the isotropic (iso-M(1.0)C(0.25)) and anisotropic (M(1.0)C(0.25)) hydrogels under the same composition is observed by POM, SEM, and X-ray tomography at different scale. From POM images shown in Fig. 2a, the fibrils of the anisotropic hydrogel have more consistent birefringence (blue) and arrange in nearly the same direction as the shear force compared with the isotropic hydrogel. The alignment of hydrogels is defined by the percentage of the azimuth angle from -5˚ to 5˚. The statistical results of the azimuth angle distribution are shown in Fig. 2d. The alignment of the M(1.0)C(0.25) is 42.0%, while the iso-M(1.0)C(0.25) has no obvious directionality. The SEM images of the iso-M(1.0)C(0.25) and M(1.0)C(0.25) in Fig. 2b show the surface morphology of the dried hydrogels. The surface morphology is much more aligned after the shear force treatment. From the simulation results of the X-ray tomography shown in Fig. 2c, the fibrils arrangement of the isotropic hydrogel is disorder, while the direction of the shear force can be easily judged by the naked eye. The statistical alignment of the M(1.0)C(0.25) from the X-ray tomography in Fig. 2e is 23.3%.

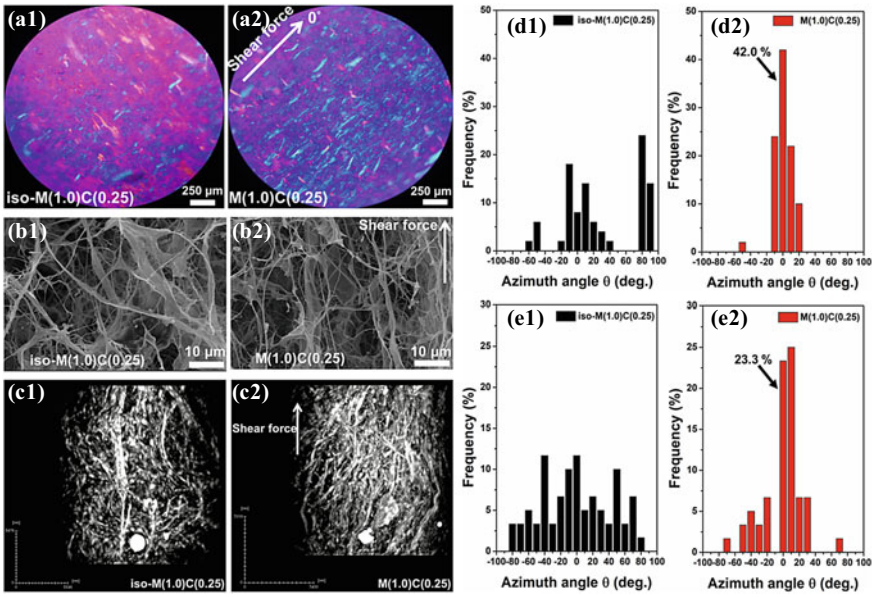

Fig. 2 The **a** POM **b** SEM **c** the simulation results of X-ray tomography images of (1) iso-M(1.0)C(0.25) and (2) M(1.0)C(0.25) and the statistical results from **d** POM and **e** TXM cross-section images

4 Discussion

The morphology of the biological scaffold is the critical factor in cell growth, including proliferation, differentiation, and migration [15, 16]. For neurons, the scaffold with specific directionality is a must to achieve the directional transmission of nerve signals. This study proposes an effective and low-cost method to prepare hydrogels with specific alignment. The shear force applied to the CNF^{+} solution shown in Fig. 1b successfully aligns the cellulose along the direction of the shear force. Due to the optically positive order structure of the fibrils, the POM technique is an appropriate method to analyze the distribution of the fibrils in hydrogels at the microscale. The hydrogel without applying shear force shows the random direction distribution of fibrils. Neither blue (1st and 3rd quadrant) nor orange (2nd and 4th quadrant) part dominates in Fig. 2a1, while the blue part dominates after applying the shear force shows in Fig. 2a2. The SEM technique shows the surface morphology from micro to nanoscale as Fig. 2b shown, however, freeze-dried samples are required under the limitation of a high vacuum. Freeze-dried samples may distort the high-water-content hydrogel. Therefore the X-ray tomography becomes a powerful technique to study the 3D structure in situ at the sub-micro scale. Through the TXM cross-section images at different degrees, the real 3D structure of aqueous hydrogels can be reconstructed as Fig. 2c shown. Performing statistical analysis on POM and TXM cross-section images, the alignment of the anisotropic hydrogel, M(1.0)C(0.25), can

be quantified as 42.0% as cellulose bundles arranged at the microscale and 23.3% as nanofibrils arranged at the sub-micro scale as Fig. 2d, e shown respectively. The alignment from TXM is lower than the one from POM. Since the result from TXM analyzed at different degree considers not only the azimuth angle but the elevation angle represented to the angle between the fibrils and the rotation axis. However, POM images are the result of fibrils projecting on the imaging plane which simplify the alignment without consideration the elevation angle effect causes the overestimation. In previous studies [17], micro-CT was widely used to identify the 3D structure of hydrogels at the microscale. Since the scale of neurons may be low to a few microns, the alignment at the sub-micro or nanoscale is desired to guide the directional growth of nerves. The sub-micro X-ray tomography used in this study helps us not only understand the 3D structure of hydrogels in situ, but the arrangement of cellulose nanofibrils similar to the nerves scale was successfully observed. The novel sub-micro X-ray tomography is the potential technique to identify the true 3D structure of biominic scaffolds for tissue engineering in the coming future.

5 Conclusions

The polypeptide with glutamate as a neurotransmitter has been proven to stimulate the growth and proliferation of neurons. This study successfully modified PBG to water-soluble polyelectrolyte, PBGA60-Na. The easily arranged cellulose nanofibrils (CNF^+) with good strength to support nerve growth can be quickly crosslinked into nanocomposite hydrogels through electrostatic force and hydrogen bonding force. An effective, low-cost method to align hydrogel along the direction of the shear force has been developed. The alignment of the cellulose bundles of aqueous hydrogels at the microscale observed by POM is up to 42.0%. To solve the distortion of freeze-dried samples, we chose the novel sub-micro X-ray tomography instead of SEM to observe the true 3D structure of aqueous hydrogels. The alignment of nanofibrils can reach 23.3% in the three-dimension. The novel sub-micro X-ray tomography is the potential technique to identify the true 3D structure of biominic scaffold to tissue engineering in the coming future.

Acknowledgements This research was supported financially by the Ministry of Science and Technology (MOST), Taiwan, under Contracts MOST 108–2221–E–002–027–MY3.

Conflict of Interest The authors declare that they have no conflict of interest.

References

1. Tham YC, Li X, Wong TY, Quigley HA, Aung T, Cheng CY (2014) Global prevalence of

glaucoma and projections of glaucoma burden through 2040: a systematic review and meta-analysis. Ophthalmology 121:2081–2090
2. Gokoffski KK, Peng M, Alas B, Lam P (2020) Neuro-protection and neuro-regeneration of the optic nerve: recent advances and future directions. Curr Opin Neurol 33:93–105
3. Amani H, Arzaghi H, Bayandori M, Dezfuli AS, Pazoki-Toroudi H, Shafiee A, Moradi L (2019) Controlling cell behavior through the design of biomaterial surfaces: a focus on surface modification techniques. Adv Mater Interfaces 6:1900572
4. Vrabec JP, Levin LA (2007) The neurobiology of cell death in glaucoma. Eye 21:S11–S14
5. Chimene D, Kaunas R, Gaharwar AK (2020) Hydrogel bioink reinforcement for additive manufacturing: a focused review of emerging strategies. Adv Mater 32:1902026
6. Sur S, Newcomb CJ, Webber MJ, Stupp SI (2013) Tuning supramolecular mechanics to guide neuron development. Biomaterials 34:4749–4757
7. Godbe JM, Freeman R, Burbulla LF, Lewis J, Krainc D, Stupp SI (2020) Gelator length precisely tunes supramolecular hydrogel stiffness and neuronal phenotype in 3D culture. ACS Biomater Sci Eng 6:1196–1207
8. Li A, Hokugo A, Yalom A, Berns EJ, Stephanopoulos N, McClendon MT, Segovia LA, Spigelman I, Stupp SI, Jarrahy R (2014) A bioengineered peripheral nerve construct using aligned peptide amphiphile nanofibers. Biomaterials 35:8780–8790
9. Berns EJ, Sur S, Pan L, Goldberger JE, Suresh S, Zhang S, Kessler JA, Stupp SI (2014) Aligned neurite outgrowth and directed cell migration in self-assembled monodomain gels. Biomaterials 35:185–195
10. Antman-Passig M, Shefi O (2016) Remote magnetic orientation of 3D collagen hydrogels for directed neuronal regeneration. Nano Lett 16:2567–2573
11. Omidinia-Anarkoli A, Boesveld S, Tuvshindorj U, Rose JC, Haraszti T, Laporte LD (2017) An injectable hybrid hydrogel with oriented short fibers induces unidirectional growth of functional nerve cells. Small 13:1702207
12. Rose JC, Gehlen DB, Haraszti T, Köhler J, Licht CJ, Laporte LD (2018) Biofunctionalized aligned microgels provide 3D cell guidance to mimic complex tissue matrices. Biomaterials 163:128–141
13. Rose JC, Cámara-Torres M, Rahimi K, Köhler J, Möller M, Laporte LD (2017) Nerve cells decide to orient inside an injectable hydrogel with minimal structural guidance. Nano Lett 17:3782–3791
14. Lin CY, Luo SC, Yu JS, Chen Ta, Su WF (2019) Peptide-based polyelectrolyte promotes directional and long neurite outgrowth. ACS Appl. Bio Mater, 518–526
15. Huang G, Li F, Zhao X, Ma Y, Li Y, Lin M, Jin G, Lu TJ, Genin GM, Xu F (2017) Functional and biomimetic materials for engineering of the three-dimensional cell microenvironment. Chem Rev 117:12764–12850
16. Li Y, Rodrigues J, Tomás H (2012) Injectable and biodegradable hydrogels: gelation, biodegradation and biomedical applications. Chem Soc Rev 41:2193–2221
17. Cengiz IF, Oliveira JM, Reis RL (2018) Micro-CT – a digital 3D microstructural voyage into scaffolds: a systematic review of the reported methods and results. Biomater Res 22:26

^{111}In-radiolabeling of Mesenchymal Stem Cell-derived Extracellular Vesicles for Quantitative In Vivo Imaging

Cheng-Hsiu Lu, Yi-An Chen, Chien-Chih Ke, Chao-Cheng Chen, and Ren-Shyan Liu

1 Introduction

Mesenchymal Stem Cells (MSCs) are multipotent stromal cells which can be found in different tissues including bone marrow, fat, cord blood and umbilical cord. MSCs are capable of self-renewal and have a great potential to differentiate into adipocytes, osteocytes, chondrocytes…, etc. [1–3]. Upon 2019, there were almost 920 clinical trials of using MSCs in the treatment of several types of disease, expounding that treatment of MSCs have been considered as a promising therapeutic strategy. MSCs exert their therapeutic effect by different mechanisms including immunomodulation, differentiation potential, homing and paracrine effect [4, 5]. Nevertheless, paracrine effect has been reported to be the major role in treatment of MSCs [6].

C.-H. Lu · R.-S. Liu (✉)
Program of Biomedical Science and Engineering, National Yang Ming Chiao Tung University, Taipei, Taiwan

Y.-A. Chen · R.-S. Liu
Institute of Clinical Medicine, National Yang Ming Chiao Tung University, Taipei, Taiwan

C.-C. Chen · R.-S. Liu
Department of Biomedical Imaging and Radiological Sciences, National Yang Ming Chiao Tung University, Taipei, Taiwan

Y.-A. Chen · C.-C. Ke · R.-S. Liu
Molecular and Genetic Imaging Core, Mouse Clinic, National Comprehensive Mouse Phenotyping and Drug Testing Center, Taipei, Taiwan

C.-C. Ke
Department of Medical Imaging and Radiological Sciences, Kaohsiung Medical University, Kaohsiung, Taiwan

R.-S. Liu
Department of Nuclear Medicine, Cheng Hsin Hospital, Taipei, Taiwan

© The Author(s), under exclusive license to Springer Nature Switzerland AG 2022

K.-P. Lin et al. (eds.), *Future Trends and Challenges of Molecular Imaging and AI Innovation*, Springer Proceedings in Physics 272,
https://doi.org/10.1007/978-3-030-92786-8_2

Extracellular vesicles (EVs) are naturally generated vesicles from cells. These vesicles mediate the cell-to-cell communication, and are capable of horizontal transfer of protein, nucleic acids as well as lipids from parental cells to recipient cells (Samanta et al. in Acta Pharmacol Sin 39:501–513, 2018). Based on these inherent characteristics, EVs-based remedy has been considered as a promising therapeutic candidate to treat variety of diseases (Yu et al. in Int J Mol Sci 15:4142–4157, 2014). Therapeutic effects of MSC-derived EVs (MSC-EVs) has been demonstrated on injury repair, regulation of immune system and inhibition of tumorigenesis (Maji et al. in Am J Physiol Gastrointest Liver Physiol 312:G194–G200, 2017). Therefore, knowing the pharmacokinetics biodistribution and the fate of EVs are worthy for pursuit.

As a potential future medical regimen for human disease, the information of EVs' behavior in the living subjects after administration needs to be urgently gathered. However, an effective method to monitor the *in vivo* behavior of EVs has not yet been developed. Despite that several approaches have tried to localize the distribution of EVs *in vivo*, including optical imaging with luminescent or fluorescent probes, most of the cases have limitations of signal penetration (Rocco et al. in Stem Cells Int 2016:5029619, 2016).

Herein, we have developed a simple and valid approach by combination of radiolabeled EVs and SPECT/CT imaging to access the *in vivo* biodistribution of EVs in small animal. ^{111}In-oxine is a commercially available clinical imaging agent for the use of radiolabeling leukocytes, lymphocytes, NK cells, MSCs as well as liposomes (Kraitchman et al. in Circulation 112:1451–1461, 2005;Malviya et al. in Mol Pharm 13:1329–1338, 2016;). Due to its lipophilic property, ^{111}In-oxine is easily able to penetrate the cell membrane, into the cells, then the complex disassembles and ^{111}indium is trapped in the cytoplasm. In addition, the 2.8 days half-life of ^{111}Indium allows a prolonged observation period to monitor dynamic behavior of MSC-EVs. In this study, we established a platform by radiolabeling MSC-EVs with ^{111}In-oxine for SPECT/CT imaging, which has the potential for MSC-EVs trafficking *in vivo*.

2 Materials and Methods

A. Preparation of EVs

Conditioned medium was collected and MSC-derived EVs were isolated using Exo-Prep (Lonza) according to the manufacturer's protocol. In brief, conditioned medium was mixed with equal volume of Exo-Prep reagent and incubated for 60 min. The mixture was centrifuged at 10,000 g for 60 min and the supernatant was aspirated. The residual solution was centrifuged at 10,000 g for 5 min, and polymeric materials were subsequently eliminated using Sephadex G-25 in PD-10 desalting columns (GE Healthcare) [13]. After concentration to appropriate volume with 100 kDa Amicon® Ultra-15 Centrifugal Filter Units, the EVs were stored at -80 °C. To isolate EVs by sequential centrifugation, the conditioned medium was centrifugated at 10,000 g for

30 min at 4 °C to remove cell debris, and the supernatant was then ultracentrifuged at 100,000 g for 70 min at 4 °C using SW 28 rotor (Beckman Coulter). The pellets were resuspended in 1 mL PBS and ultracentrifuged at 100,000 g for 70 min at 4 °C [14].

B. Preparation and Purification of ^{111}In-EVs

15 μl of 68 mM oxine (8-hydroxyquinoline) in ethanol was mixed with 10 μl of ^{111}In (Indium chloride in 0.05 M HCl) in 400 μl of 0.1 M sodium acetate buffer (pH 5.5) and then incubated at 50 °C for 30 min. The lipophilic components were extracted three times with 0.1 ml of chloroform and then dried using a rotary evaporator. The extracted ^{111}In-oxine in chloroform was evaporated to dryness. This was followed by the addition of 20 μl of ethanol and 180 μl of labeling buffer containing EVs into the vial for one hour at 37 °C. Each mL of the labeling buffer contains 100 μg polysorbate 80, and 6 mg of HEPES (N-2-hydroxyethyl-piperazine-N'-2-ethane sulfonic acid) buffer in 0.75% sodium chloride solution. The pH range of labeling buffer was restricted to 6.5 ~ 7.5. The radioactivity of ^{111}In-oxine was measured using either a dose calibrator (CRC-15R, Capintec, Bioscan) or a gamma scintillation counter (Cobra II Autogamma, Packard).

3 Results

A. *Radiolabeling of WJ-MSC-EVs using^{111} In-oxine*

Fraction 7–10, of which the radioactivity and protein were detected simultaneously, were considered as ^{111}In-oxine-EVs (Fig. 1a). The labeling efficiency was about 5%. ^{111}In-oxine-EVs incubated in the serum remained stable (85%) for at least 24 h (Fig. 1b), and the radiochemical purity of ^{111}In-oxine-EVs was higher than 90% as determined by the instant thin-layer chromatography (ITLC) method (Fig. 1c). In order to examine whether labeling procedure alter the characteristics of EVs, expression of surface markers and particle size of labeled EVs were assessed. The results showed that the size distribution of ^{111}In-oxine-EVs was similar to the unlabeled EVs and the peak of size distribution did not change markedly (Fig. 1d). Also, labeled EVs had similar expression of CD63 and HSP70 compared with those in parental EVs (Fig. 1e). In addition, to precisely calculate the dosage of EVs in radiolabeling process, the protein recovery rate was measured using PD-10 desalting columns followed by 100 kDa Amicon® Ultra-15 Centrifugal Filter Units. The result showed that PD-10 and 100 k filter retained 27% of EVs protein after labeling (Fig. 1f). These results suggested that labeling with ^{111}In-oxine did not alter the characteristics of WJ-MSC-EVs.

B. In vivo *imaging of WJ-MSC-EVs*

For in vivo imaging of WJ-MSC-EVs, 1.443 ± 0.13 MBq μCi ^{111}In-oxine-EVs were intravenously administrated into C57BL/6 mice followed by μSPECT/CT imaging

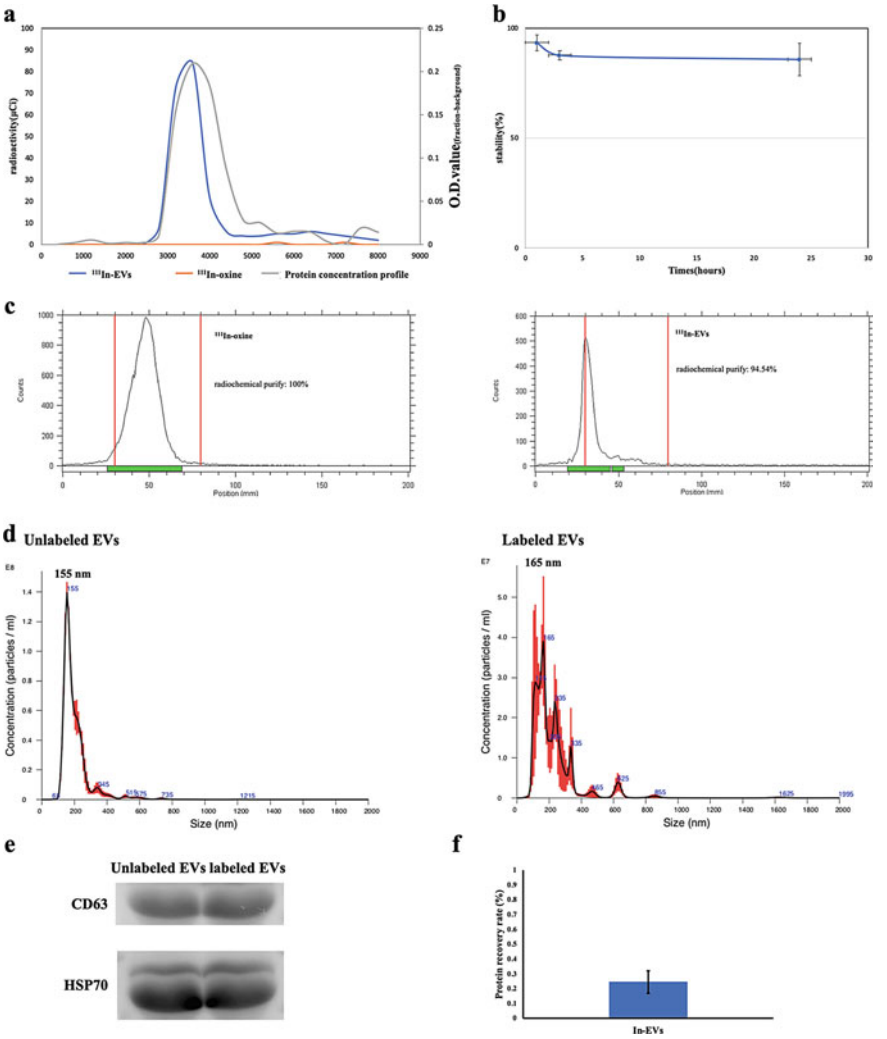

Fig. 1 Purification and characterization of ^{111}In-oxine labeled EVs. **a** Size exclusion was adopted to purify the ^{111}In-oxine labeled EVs through eluting PBS in PD-10 columns. The labeling efficiency was about 5%. **b** Stability of ^{111}In-oxine-EVs was examined in FBS. **c** ^{111}In-oxine and ^{111}In-oxine-EVs were analyzed by instant thin layered chromatography (ITLC) performing on a silica-gel-impregnated glass fiber sheet. The radiochemical purity of ^{111}In-oxine-EVs was general more than 90%. **d** The size distribution of ^{111}In-oxine-EVs was measured using NTA. **e** Representative western blot of labeled EVs and unlabeled EVs immunolabeled using CD63 and HSP70 antibody and visualized by ECL is shown. **f** Protein recovery rate was calculated by Bradford protein assay

at 1, 3, 6 and 24 h post-injection. A parallel imaging study was performed with ^{111}In-oxine, without labeling with EVs. One hour after the injection, ^{111}In-oxine-EVs mainly accumulated in the liver and spleen while most ^{111}In-oxine accumulated in the lung and kidney. The accumulated activity decreased gradually with time (Fig. 2a, b).

C. Ex vivo *biodistribution of WJ-MSC-EVs*

To further characterize the biodistribution, the mice were intravenously administrated ^{111}In-oxine-EVs or ^{111}In-oxine. After 1, 3, 6, 24 h, the mice were sacrificed to investigate biodistribution with ex vivo quantitation of radioactivity. Among all organs, the spleen, liver and kidney showed higher radioactivity in mice at one hour post iv injection of ^{111}In-oxine-EVs. The radioactivity accumulation in the liver, spleen and kidney gradually declined until 24 h post-injection (Fig. 3a). The radioactivity

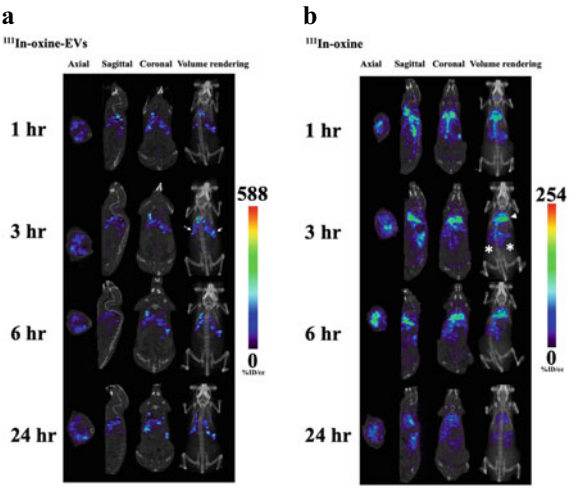

Fig. 2 In vivo μSPECT/CT imaging of ^{111}In-oxine-EVs. **a** After intravenous injection of ^{111}In-oxine-EVs, μSPECT/CT images was acquired at 1 h, 3 h, and 6 h as well as 24 h in C57BL/6 mice. **b** Micro-SPECT/CT images of ^{111}In-oxine administered groups. White arrow, spleen; dotted white arrow, liver; white arrow head, lung; white asterisk, kidney

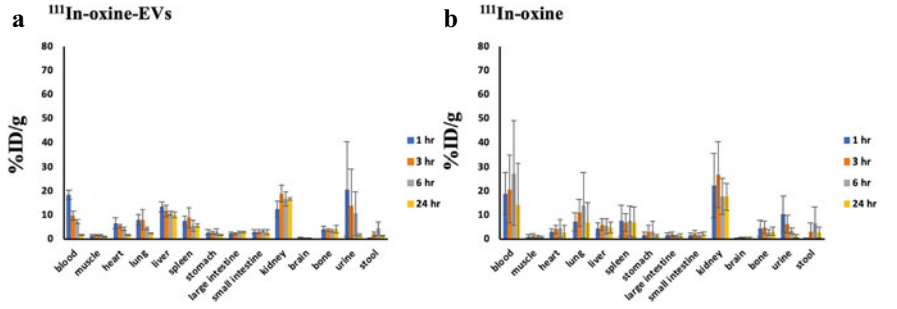

Fig. 3 Ex vivo biodistribution of ^{111}In-oxine-EVs. ^{111}In-oxine-EVs or ^{111}In-oxine were intravenously injected into mice and sacrificed at 1, 3, 6, and 24 h to assess ex vivo radioactivity of organs

in urine was much higher than that in stool indicating that the metabolites of ^{111}In-oxine-EVs were mainly eliminated via renal excretion. The different biodistribution profiles were observed specifically in the blood, lung and kidney in ^{111}In-oxine administered group (Fig. 3b).

4 Discussion

The present study demonstrated that WJ-MSC-EVs were able to be directly and simply labeled with ^{111}In-oxine, and retained the characteristics of MSC-EVs after radiolabeling. Moreover, in vivo μSPECT/CT imaging analysis and ex vivo quantitation demonstrated the exogenous WJ-MSC-EVs labeled with ^{111}In-oxine accumulated in the liver, spleen and kidney.

Several approaches have been established to monitor EVs in vivo using radiolabeling methods. However, most of them are complicated and time-consuming. Nikolopoulou et al. tried to use ^{131}I-phenylpropanoate to label EVs in 2015, but the article still remained unpublished. Besides, Hwang et al. developed a direct method to label exosome-mimetic nanovesicles (ENVs) using ^{99m}Tc-HMPAO. In that study, the in vivo μSPECT/CT imaging of ^{99m}Tc-HMPAO-ENVs highly accumulated in the liver and spleen. However, ENVs as alternatives to natural EVs, may not represent the biodistribution of the natural EVs labeled with ^{99m}Tc-HMPAO-ENVs. In the current study, we have developed an optimal approach by combination of ^{111}In-oxine-EVs and μSPECT/CT imaging, to demonstrate the biodistribution of WJ-MSC-EVs.

^{111}In-oxine is an appreciated potent agent for tracking of MSC-EVs. The *in vivo* imaging and *ex vivo* biodistribution demonstrated that ^{111}In-oxine-EVs clearly accumulated in the liver, spleen, and kidney. However, the safety and toxicity of continuously injected ^{111}In-oxine-EVs is still unknown, the more comprehensive studies is necessary.

5 Conclusions

In conclusion, we that established a simple method to label WJ-MSC-EVs with ^{111}In-oxine for in vivo imaging and quantitative analysis of exogenously administered EVs. Importantly, the characteristics of WJ-MSC-EVs were not altered during radiolabeling. ^{111}In-oxine-EVs have the potential for tracking of EVs by in vivo imaging.

Conflict of Interest The authors declare that they have no conflict of interest.

References

1. Lindner U, Kramer J, Rohwedel J, Schlenke P (2010) Mesenchymal stem or stromal cells: toward a better understanding of their biology? Transfus Med Hemother 37:75–83
2. Kern S, Eichler H, Stoeve J, Kluter H, Bieback K (2006) Comparative analysis of mesenchymal stem cells from bone marrow, umbilical cord blood, or adipose tissue. Stem Cells 24:1294–1301
3. Zeng R, Wang LW, Hu ZB et al. (2011) Differentiation of human bone marrow mesenchymal stem cells into neuron-like cells in vitro. Spine (Phila Pa 1976) 36:997–1005
4. Squillaro T, Peluso G, Galderisi U (2016) Clinical trials with mesenchymal stem cells: an update. Cell Transplant 25:829–848
5. Hoogduijn MJ, Lombardo E (2019) Mesenchymal stromal cells anno 2019: dawn of the therapeutic Era? Concise review. Stem Cells Transl Med 8:1126–1134
6. Linero I, Chaparro O (2014) Paracrine effect of mesenchymal stem cells derived from human adipose tissue in bone regeneration. PLoS One 9:e107001
7. Samanta S, Rajasingh S, Drosos N, Zhou Z, Dawn B, Rajasingh J (2018) Exosomes: new molecular targets of diseases. Acta Pharmacol Sin 39:501–513
8. Yu B, Zhang X, Li X (2014) Exosomes derived from mesenchymal stem cells. Int J Mol Sci 15:4142–4157
9. Maji S, Matsuda A, Yan IK, Parasramka M, Patel T (2017) Extracellular vesicles in liver diseases. Am J Physiol Gastrointest Liver Physiol 312:G194–G200
10. Di Rocco G, Baldari S, Toietta G (2016) Towards therapeutic delivery of extracellular vesicles: strategies for in vivo tracking and biodistribution analysis. Stem Cells Int 2016:5029619
11. Kraitchman DL, Tatsumi M, Gilson WD et al (2005) Dynamic imaging of allogeneic mesenchymal stem cells trafficking to myocardial infarction. Circulation 112:1451–1461
12. Malviya G, Nayak T, Gerdes C, Dierckx RA, Signore A, de Vries EF (2016) Isolation and (111)In-Oxine Labeling of Murine NK Cells for assessment of cell trafficking in orthotopic lung Tumor model. Mol Pharm 13:1329–1338
13. Li P, Kaslan M, Lee SH, Yao J, Gao Z (2017) Progress in exosome isolation techniques. Theranostics 7:789–804
14. Thery C, Amigorena S, Raposo G, Clayton A (2006) Isolation and characterization of exosomes from cell culture supernatants and biological fluids. Curr Protoc Cell Biol Chapter 3:Unit 3 22

A Comparative Study of Drug Distribution Using Photoacoustic Imaging and Radionuclide-Based Sampling in PEGylated Gold Nanostars-Mediated Photothermal Therapy

Wing Sum Lau, Chao-Cheng Chen, Ju-Yu Chen, Hui-Wen Chan, Deng-Yuan Chang, Hsin-Ell Wang, and Liang-Ting Lin

1 Introduction

Triple-negative breast cancer (TNBC) is aggressive with a poor prognosis and high relapse rate, contributing to 15–20% of overall breast carcinomas [1]. TNBC is defined by lacking estrogen receptors and progesterone receptors, as well as without overexpression of the human epidermal growth factor receptor 2 [2]. Conventional chemotherapy remains the mainstay of TNBC treatment regimen, which often conversely lead to systemic toxicity and chemoresistance [3]. Nanomedicine emerges as a novel therapeutic strategy to enhance the therapeutic efficacy and minimize side-effects [4]. Gold nanoparticles (AuNPs) are extensively studied as a theranostic agent for imaging and light-induced therapy, due to the tunable optical characteristics, simple surface modifications and biocompatibility [5]. AuNPs exhibit strong absorption of near-infrared (NIR) light. Upon laser irradiation, AuNPs convert the absorbed light into heat, which can be used in sensitizing tumor to photothermal therapy (PTT) [6]. Factors affecting the effectiveness of AuNPs-mediated PTT include the

W. S. Lau (✉) · J.-Y. Chen · L.-T. Lin
Department of Health Technology and Informatics, The Hong Kong Polytechnic University, Hung Hom, Hong Kong, China

L.-T. Lin
e-mail: lt.lin@polyu.edu.hk

C.-C. Chen · H.-W. Chan · D.-Y. Chang · H.-E. Wang
Department of Biomedical Imaging and Radiological Sciences, National Yang Ming Chiao Tung University, Taipei, Taiwan

© The Author(s), under exclusive license to Springer Nature Switzerland AG 2022

K.-P. Lin et al. (eds.), *Future Trends and Challenges of Molecular Imaging and AI Innovation*, Springer Proceedings in Physics 272,
https://doi.org/10.1007/978-3-030-92786-8_3

photothermal conversion efficiency and AuNPs concentration within the irradiated area. Gold nanostars have a large surface-to-volume ratio and superior photothermal conversion efficiency, which can be a promising candidate for PTT [7]. Moreover, AuNPs tend to accumulate in tumor via enhanced permeability and retention (EPR) effect. Therefore, the in vivo distribution of photosensitizer needs to be carefully evaluated, in order to achieve tumor-selective PTT.

Molecular imaging plays a crucial role in guiding preclinical PTT studies by non-invasively tracking the photothermal agent accumulation along time. Photoacoustic imaging (PAI) is an advanced imaging modality combining the use of NIR light and ultrasound. AuNPs in tissue absorb light from the pulsed laser and generate acoustic waves by thermoelastic expansion [8]. Meanwhile, the changes in tumor microenvironment can be examined by analyzing PAI signals from oxyhemoglobin (HbO_2) and deoxyhemoglobin (Hb).

On the other hand, radiolabeling of AuNPs allows an investigation of the biodistribution and pharmacokinetics profile, conducted ex vivo or non-invasively using positron emission tomography (PET) and single photon emission computed tomography (SPECT), which are highly sensitive and extensively used in clinical applications. In the present work, we monitored the distribution of PEGylated gold nanostars (pAuNSs) using PAI and radionuclide-based biodistribution, thus determined the optimal treatment window for pAuNSs-mediated PTT. Afterwards, the therapeutic efficacy was evaluated and the potentials of theranostic pAuNSs for TNBC were discussed.

2 Methods & Materials

A. *Preparation of PEGylated Gold Nanostars*

The gold nanostars (AuNSs) were synthesized and modified as previously elaborated [9]. Briefly, AuNSs were formed by reducing hydrogen tetrachloroaurate solution with HEPES buffer, and followed by PEGylation to obtain pAuNSs. For radionuclide-based analysis, pAuNSs was tagged with indium-111 using DTPA as chelator, in order to acquire indium-111 labelled pAuNSs (^{111}In-DTPA-pAuNSs). The absorption spectrum of pAuNSs was validated by UV–visible spectrophotometer (Agilent 8453; Agilent Technologies, CA, USA). The labelling efficiency of radioactive surrogate was measured using the instant thin-layer chromatography (iTLC) with radio–thin-layer chromatography scanner (Bioscan AR2000; Bioscan, TriFoil Imaging Inc., CA, USA).

B. *Orthotopic Triple-Negative Breast Cancer Animal Model*

4T1_PB3R murine mammary tumor cell line was used for establishing the orthotopic TNBC model in female BALB/c nude mice (6 weeks old) [10]. Cells were cultured in RPMI-1640 medium with 10% fetal bovine serum and 1% penicillin–streptomycin solution, maintained in 37 °C, 5% CO2 incubator. 1×10^6 4T1_PB3R cells were harvested and suspended in 50 μl of phosphate buffered saline solution, then injected into the mammary pad. Animal weight and tumor size were measured and recorded every three days, until the tumor volume reached 100 mm^3 for in vivo studies. Animal experiments were in compliance with the ethical approval granted from the Animal Subjects Ethics Sub-Committee (ASESC) of The Hong Kong Polytechnic University (19–20/45-HTI-R-GRF).

III. In vivo *Biodistribution Study*

The distribution of ^{111}In-DTPA-pAuNSs (36.4 ± 0.8 μCi/mice) in the 4T1 tumor-bearing mice ($n = 2$) was investigated at 1, 4, 24, and 48 h post-intravenous injection. At each designated time point, two tumor-bearing mice was sacrificed, and the tissues/organs of interest were harvested, washed with water and weighted, followed by radioactivity measurement with radioactive decay correction using the Wallace 1470 Wizard Gamma counter (GMI, Inc., Ramsey, MN, USA). Data were expressed as the percentage injected dose per gram of tissues/organs (%ID/g).

IV. In vivo *Photoacoustic Imaging*

PAI scan was performed using Multispectral Optoacoustic Tomography (MSOT) inVision 128 system (iThera Medical, Germany). The tumor-bearing mice ($n = 2$) were anesthetized with 2% isoflurane and secured inside a designated animal holder, then placed inside the imaging chamber filled with 34 °C deionized water. Pre and post-injection MSOT scans of tumor region were acquired at a series of time intervals (1, 2, 4, 24, 48 h) upon pAuNSs administration via tail vein (10 mg Au/kg). MSOT images were reconstructed by model-based method and component signals were spectrally unmixed.

E. *Evaluation of Photothermal Therapy Efficacy*

For treatment, tumor-bearing mice were randomly divided into pAuNSs-PTT and laser-only group ($n = 3$), which received intravenous injection of pAuNSs (10 mg Au/kg) or normal saline respectively. The tumor was irradiated by 808 nm laser (1 W/cm^2) repeatedly for 3 min twice with a 2 min rest in between at 24 h post-injection. The surface temperature of tumor was recorded by infrared camera during irradiation (Fluke Corp., WA, USA). To assess the therapeutic efficacy of pAuNSs-mediated PTT, the tumor growth was monitored twice a week, with the volume determined by caliper measurement and calculated as volume = (width^2 × length)/2. The tumor burden was also evaluated using bioluminescent imaging upon the intraperitoneal injection of D-luciferin (150 mg/kg) (VivoGlo Luciferin; Promega Corp., WI, USA) and imaged with IVIS In Vivo Animal Imaging Systems (Perkin Elmer Inc., MA, USA).

3 Results and Discussion

A. *Synthesis of PEGylated Gold Nanostars*

The UV–visible-NIR spectrum in Fig. 1 demonstrated a strong absorption of pAuNSs within the first NIR window (650–950 nm), where the transparent window of least photon attenuation from Hb and HbO_2 locates [11]. The absorption peak was at 820 nm. The labelling efficiency of ^{111}In-DTPA-pAuNSs was greater than 85%.

B. In vivo *Biodistribution Study*

According to the biodistribution results reported in Table 1, ^{111}In-DTPA-pAuNSs eliminated rapidly from blood after receiving the intravenous injection. The radioactivity dropped from 21.51 ± 0.99%ID/g at 1 h post-injection (p.i.) to 0.48 ± 0.12%ID/g at 24 h p.i.. The reticuloendothelial system exhibited high uptake of ^{111}In-DTPA-pAuNSs within the experimental period. In addition, significant radioactivity in urine could be attributed to the ^{111}In-DTPA-pAuNSs and their radiolabeled PEG fragments. The highest tumor uptake was demonstrated at 4 h p.i. (2.08 ± 0.17%ID/g), remained plateau till 24 h p.i., and then dropped to 1.34 ± 0.12%ID/g at 48 h p.i.. The calculated concentration of pAuNSs in 4T1 tumor reached approximately 4 ppm at 4 h p.i.

III. *Detection of pAuNSs Photoacoustic Signals*

Pre-injection MSOT images of tumor were taken with baseline signals of pAuNSs, Hb and HbO_2 resolved (Fig. 2a). During 2–24 h p.i., pAuNSs signals in large vessels diminished and the tumor periphery was gradually enhanced, enabling a good differentiation of tumor vasculature (Fig. 2b). Heterogenous probe distribution in tumor was noticed, where pAuNSs predominantly accumulated in the perivascular spaces. Moreover, the quantification of pAuNSs signal intensities showed a gradual saturation during 2-24 h (Fig. 2c). MSOT signals in tumor reached a four-fold increment at 24 h (2.53 ± 0.71 a.u.) comparing to the baseline (0.56 ± 0.02 a.u.), which could

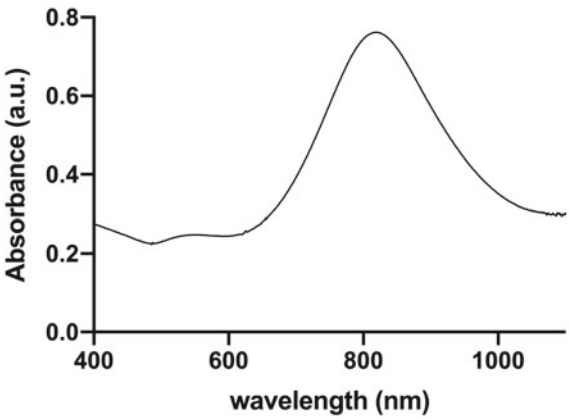

Fig. 1 Absorption spectrum of PEGylated gold nanostars (pAuNSs) characterized by UV–vis spectrophotometer

Table 1 Biodistribution of ^{111}In-DTPA-pAuNSs in the 4T1 tumor-bearing mouse model ($n = 2$)

	1 h	4 h	24 h	48 h
Blood	21.51 ± 0.99	5.45 ± 0.94	0.48 ± 0.12	0.13 ± 0.01
Liver	17.81 ± 1.35	21.36 ± 0.34	19.75 ± 0.18	26.43 ± 1.71
Spleen	34.49 ± 9.35	32.58 ± 5.57	22.97 ± 0.47	23.87 ± 1.08
Kidney	4.50 ± 0.10	4.64 ± 0.36	2.71 ± 0.16	2.26 ± 0.00
Muscle	0.30 ± 0.07	0.23 ± 0.04	0.19 ± 0.19	0.06 ± 0.00
Urine	135.77 ± 18.25	67.36 ± 23.83	3.81 ± 0.55	3.58 ± 0.90
Feces	0.03 ± 0.01	1.29 ± 0.43	0.57 ± 0.07	0.34 ± 0.11
Tumor	1.39 ± 0.23	2.08 ± 0.17	2.07 ± 1.21	1.34 ± 0.12
Data expressed as the percentage of the injected dose per gram of an organ (%ID/g)				

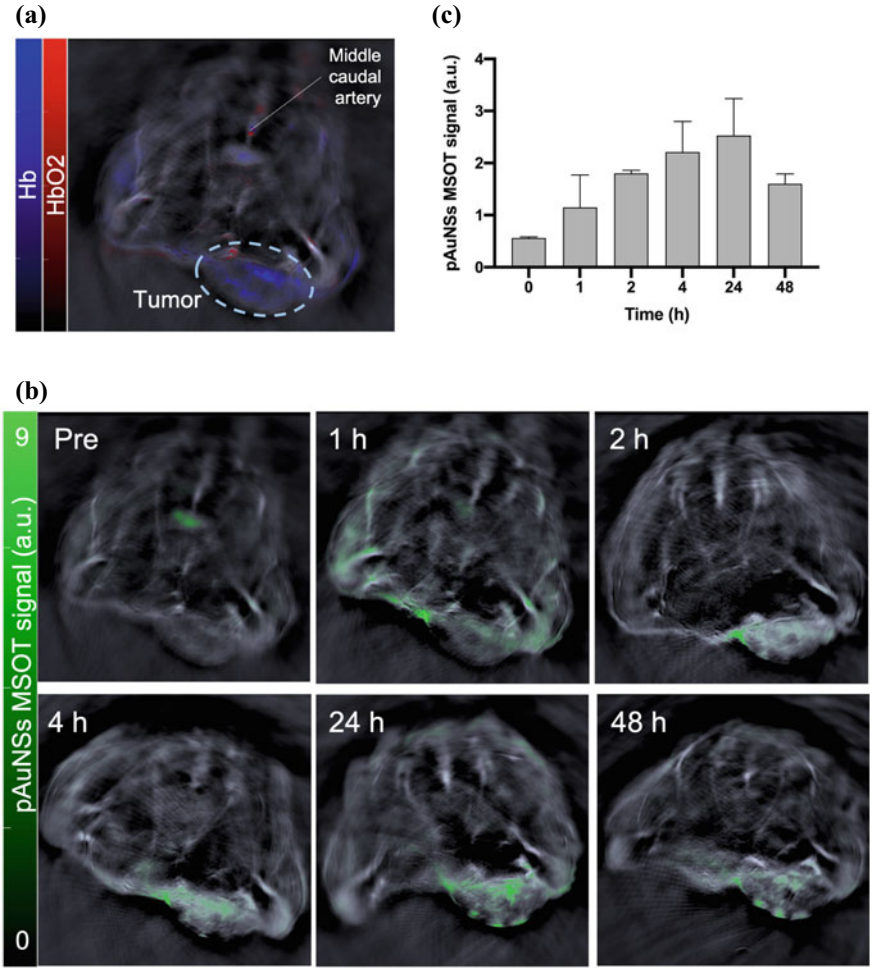

Fig. 2 In vivo MSOT tracking of pAuNSs uptake in 4T1 tumor. **a** Pre-injection image of the deoxyhemoglobin (blue) and oxyhemoglobin (red) distribution ($n = 2$). **b** Transverse images of tumor at different time intervals upon i.v. injection of pAuNSs (green) (10 mg Au/kg, green). **c** MSOT intensity of pAuNSs signals in tumor over time ($n = 2$)

be attributed to the EPR effect usually taking 6-24 h [12]. From the biodistribution analysis and MSOT images, most pAuNSs in bloodstream had eliminated at 24 h, explaining the MSOT signals at 24 h could be contributed by pAuNSs predominantly trapping in the tumor, suggesting the best treatment timepoint for tumor-selective PTT.

IV. *Evaluation of Photothermal Therapy Efficacy*

The surface temperature of the tumor region during laser exposure was recorded using infrared camera as shown in Fig. 3. The maximal tumor temperature after

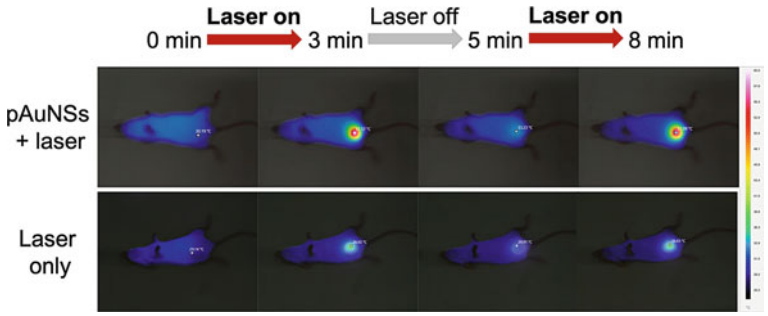

Fig. 3 In vivo photothermal conversion effect. Thermal images of 4T1 tumor-bearing mice receiving laser irradiation with administration of pAuNSs and normal saline respectively ($n = 3$)

808 nm laser irradiation reached 55.3 ± 2.88 °C in mice administered with pAuNSs, comparing to 36.8 ± 0.24 °C in the laser-only group. The tumor temperature rise repeatedly exceeded 50 °C, which could cause irreversible thermal ablation of the tumor tissue, thus inducing cellular death by necrosis [13].

Bioluminescent images revealed a significant reduction of luciferase activity in PTT-treated group, indicating suppression of the tumor viability (Fig. 4a). On the contrary, the laser-only group exhibited distant metastases on day 21 post-laser irradiation. Furthermore, the tumor burden became undetectable by caliper measurement in pAuNSs-mediated PTT group, until day 14 post-PTT where local recurrence occurred in one of the three mice (Fig. 4b). However, no sign of tumor shrinkage was noticed in the laser-only group, suggesting that laser alone did not have killing effect on 4T1 tumor. There was no apparent loss in body weight after treatment in both groups, indicating that there was no observable acute toxicity caused by pAuNSs-mediated PTT or laser irradiation (Fig. 4c). Both tumor volume and bioluminescent signals corroborated a remarkable tumor suppressive effect brought by pAuNSs-mediated PTT, whereas the mechanism of cellular damage required further investigation by immunohistochemistry studies.

4 Conclusion

Herein, we presented the photoacoustic imaging and radiolabeling technique to investigate the distribution of PEGylated gold nanostars in orthotopic 4T1-tumor bearing mice at different time intervals. Both methods revealed that the maximum accumulation of pAuNSs in tumor sustained within 2-24 h, ascribed to the EPR effect. MSOT images demonstrated a predominant accumulation in perivascular spaces, which could potentially be a treatment strategy of disrupting vessels focally. With the intrinsic optical property, pAuNSs could simultaneously act as a photoacoustic contrast and photothermal sensitizer. This work shed light on the theranostic options

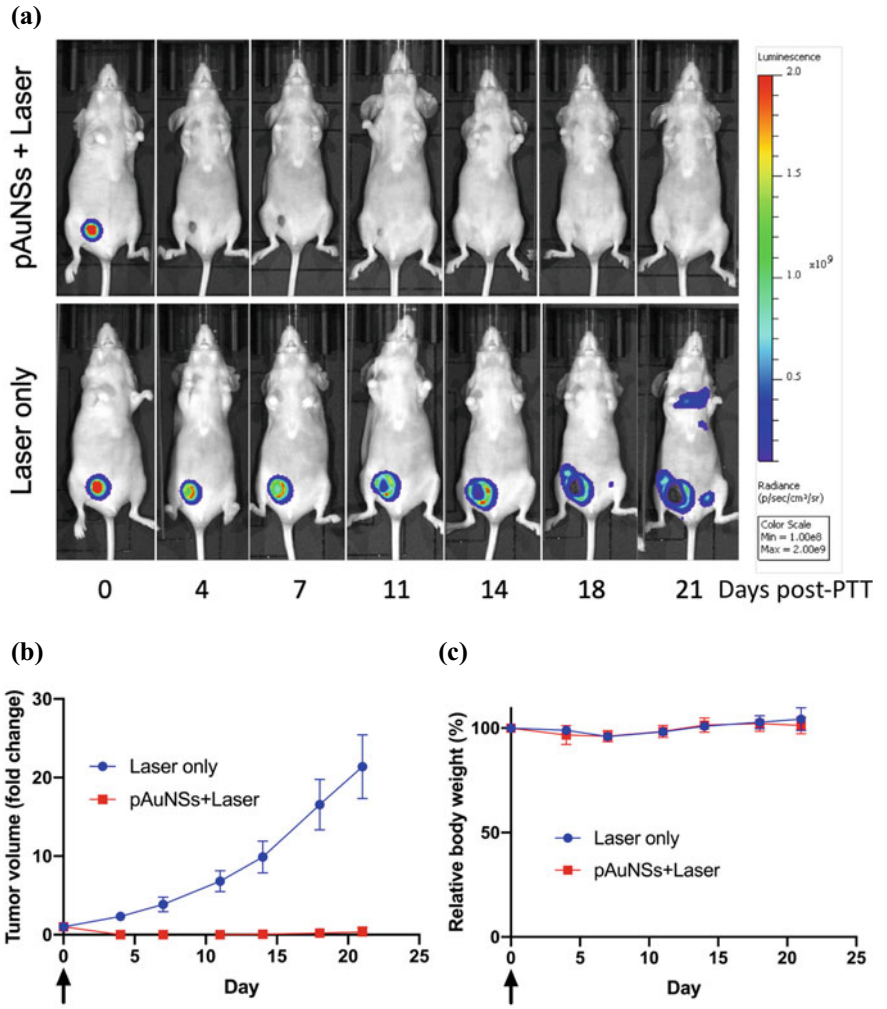

Fig. 4 Therapeutic efficacy and toxicity of pAuNSs-mediated photothermal therapy (PTT). **a** Bioluminescent images of orthotopic 4T1 tumor growth. Relative changes of tumor volume (**b**) and body weight (**c**). Tumor volume was measured by a caliper ($n = 3$). Data were represented as mean ± S.D. The black arrow indicates the initial time point of treatment

of using pAuNSs as a potential nanoplatform for image-guided cancer therapy, also unveiled the promising antitumor effect of pAuNSs-mediated PTT in orthotopic TNBC model.

Acknowledgements This work is supported by Early Career Scheme (25103719) by the Research Grant Council, HKSAR.

Conflicts of Interest The authors declare that there are no conflicts of interests regarding this study.

References

1. Jitariu A-A, Cîmpean AM, Ribatti D, Raica M (2017) Triple negative breast cancer: the kiss of death. Oncotarget 8:46652
2. Abramson VG, Lehmann BD, Ballinger TJ, Pietenpol JA (2015) Subtyping of triple-negative breast cancer: implications for therapy. Cancer 121:8–16
3. Gangi A, Mirocha J, Leong T, Giuliano AE (2014) Triple-negative breast cancer is not associated with increased likelihood of nodal metastases. Ann Surg Oncol 21:4098–4103
4. Thakur V, Kutty RV (2019) Recent advances in nanotheranostics for triple negative breast cancer treatment. J Exp Clin Cancer Res 38:1–22
5. Knights OB, McLaughlan JR (2018) Gold nanorods for light-based lung cancer theranostics. Int J Mol Sci 19:3318
6. Li W, Chen X (2015) Gold nanoparticles for photoacoustic imaging. Nanomedicine 10:299–320
7. Hao F, Nehl CL, Hafner JH, Nordlander P (2007) Plasmon resonances of a gold nanostar. Nano Lett 7:729–732
8. Valluru KS, Chinni BK, Rao NA, Bhatt S, Dogra VS (2009) Basics and clinical applications of photoacoustic imaging. Ultras Clin 4:403–429
9. Chen C-C, Chang D-Y, Li J-J et al (2020) Investigation of biodistribution and tissue penetration of PEGylated gold nanostars and their application for photothermal cancer treatment in tumor-bearing mice. J Mater Chem B 8:65–77
10. Chen Y-L, Wang C-Y, Yang F-Y et al (2014) Synergistic effects of glycated chitosan with high-intensity focused ultrasound on suppression of metastases in a syngeneic breast tumor model. Cell Death Dis 5:e1178–e1178
11. Ntziachristos V, Razansky D (2010) Molecular imaging by means of multispectral optoacoustic tomography (MSOT). Chem Rev 110:2783–2794
12. Maeda H, Nakamura H, Fang J (2013) The EPR effect for macromolecular drug delivery to solid tumors: improvement of tumor uptake, lowering of systemic toxicity, and distinct tumor imaging in vivo. Adv Drug Deliv Rev 65:71–79
13. Kaur P, Aliru ML, Chadha AS, Asea A, Krishnan S (2016) Hyperthermia using nanoparticles–promises and pitfalls. Int J Hyperth 32:76–88

CMR-Derived Extracellular Volume Fraction is Associated with the Ventricular Wall Thickness in Patients with Hypertrophic Cardiomyopathy

Shun-Chung Yang, Hung-Wen Chiu, and Mao-Yuan Su

1 Introduction

Hypertrophic cardiomyopathy (HCM) is a hereditary heart disease [1, 2]. The main cause is abnormal muscle alignment of the heart muscle [3–5], which leads to poor contraction of the heart and compensatory hypertrophy of the myocardium, resulting in thickening of the myocardium and the appearance of ventricular hypertrophy [6, 7]. This hypertrophy and lack of elasticity may lead to difficulty in ventricular relaxation and heart failure [1, 8, 9]. Left ventricular hypertrophy can develop due to factors such as hypertension, aortic stenosis or diffuse myocardial fibrosis (DMF) etc. [10–12]. Myocardial fibrosis refers to tissue damage and scarring caused by ischemia, inflammation and hypertension of the myocardium. Previous studies have demonstrated that HCM presents the DMF, which correlate with estimated LV filling pressure, suggesting a mechanistic link between DMF and abnormal diastolic function. However, it remains unknown whether the degree of DMF is associated with LVH in patients with HCM.

Cardiovascular magnetic resonance (CMR) has been widely used to quantify DMF by calculating the extracellular volume fraction (ECV) of the myocardium [13, 14].

S.-C. Yang (✉) · H.-W. Chiu
Graduate Institute of Biomedical Informatics, Taipei Medical University, Taipei, Taiwan

H.-W. Chiu
e-mail: hwchiu@tmu.edu.tw

S.-C. Yang · M.-Y. Su
Taipei Association of Radiological Technologists, Taipei, Taiwan
e-mail: maoyuansu@gmail.com

Department of Medical Imaging, National Taiwan University Hospital, Taipei, Taiwan

M.-Y. Su
Department of Medical Imaging and Radiological Technology, Yuanpei University of Medical, Technology, Hsinchu, Taiwan

© The Author(s), under exclusive license to Springer Nature Switzerland AG 2022

K.-P. Lin et al. (eds.), *Future Trends and Challenges of Molecular Imaging and AI Innovation*, Springer Proceedings in Physics 272,
https://doi.org/10.1007/978-3-030-92786-8_4

In this study, our aim was to investigate whether the severity of LVH is associated with the degree of DMF in patients with HCM.

2 Material and Methods

A. Patient selection

This study is a retrospective analysis and the CMR was performed at the National Taiwan University Hospital. A total of 125 patients who had a clinical evidence of HCM and 58 patients with Brugada syndrome (Brs) which was considered as the relative normal heart control were enrolled in this study. Patient with Brs had abnormal electrical potential activity in the heart, resulting in arrhythmias, but showed no significant different in the structure and function with healthy subjects were treated as control group. All study participants provided written informed consent.

B. CMR sequences

We performed CMR using a clinical 1.5-T scanner (Area 1.5 T, Siemens, Erlangen, Germany). Cine CMR was performed using a segmented balanced steady-state gradient echo pulse sequence with a retrospective electrocardiography (ECG)-R-wave trigger. The scanning parameters were as follows: repetition time (TR), 3.0 ms; echo time (TE), 1.5 ms; matrix size, 256 × 208; and spatial resolution, 1.21 mm. Multiple short-axis (SA) slices were prescribed in the left ventricle (LV) from the mitral orifice to apex with slice thickness of 8 mm and gap of 2 mm. The true temporal resolution was 63 ms, and 30 cardiac phases were reconstructed retrospectively for each slice level.

Myocardial T1 mapping was performed with an electrocardiography (ECG)-triggered modified Look-Locker inversion recovery (MOLLI) sequence before and 10 min after 0.15 mmol/kg intravenous administration of the gadolinium-based contrast agent (Dotarem, Guerbet, France). The MOLLI protocol used 2 Look-Locker cycles to acquire 7 images over 11 heartbeats, and the scanning parameters were as follows: TR/TE, 1.9 ms/1.0 ms; minimum inversion time, 110 ms; inversion time increment, 80 ms; matrix size, 256 × 192; slice thickness, 6 mm; spatial resolution, 1.28 mm; number of inversions, 2; images acquired after first inversion, 5; pause, 4 heartbeats; and images acquired after second inversion, 2 [15]. Three evenly spaced SA slices were acquired from the LV base to the apex. After postcontrast T1 acquisition, late gadolinium enhancement (LGE) images were acquired using an ECG-triggered phase-sensitive inversion recovery prepared segmented fast gradient-echo pulse sequence to identify the focal fibrosis or scarring.

C. Image analysis

Cine images were used to quantify the LV function and mass by determination of the endocardial and epicardial borders for each diastolic and systolic frame on all SA slices and then normalized by body surface area (BSA). Quantitative analysis of

ECV and regional wall thickness (WT) were performed on T1 maps. The ECV was calculated from pre- and postcontrast T1 maps using a region-based method and was then calibrated with the last available hematocrit (Hct) data. Four different regions, including the anterior, septal, posterior and lateral wall regions of the LV, and the area in the central area of the LV cavity were drawn on the T1 map at the mid-ventricular slice. The average T1 values of the segmented regions of interest were then computed. After obtaining the pre- and postcontrast T1 values, ECV values were calculated by using the following formula [16]:

$$ECV = \frac{\frac{1}{T1_{post}^{myo}} - \frac{1}{T1_{native}^{myo}}}{\frac{1}{T1_{post}^{blood}} - \frac{1}{T1_{native}^{blood}}} * (1 - Hct)$$

The WTs of the same regions were measured at the same level of the T1 mapping. Group comparisons in LV function, ECV and WT were compared between two group. The correlation between ECV and WT, including averaged and each segment, were assess for each group. In addition, the regional ECV was excluded if the regional myocardium showed hyper-enhancement on the LGE image. Image analysis was performed using software developed in-house provided by MATLAB 7.9 (MathWorks, Inc., Natick, Massachusetts) and Image J (NIH, USA).

D. Statistical analysis

Data are expressed as mean ± standard deviation (SD). Group comparisons in the myocardial ECV, WT and LV functional indexes were tested by the nonparametric Mann–Whitney U test. Linear regression was used to obtain a correlation coefficient between regional ECV and WT for each group. The statistical tests were two-tailed, and statistical significance was defined as $p < 0.05$. Statistical analyses were performed using SPSS software package version 20.0 (SPSS Inc., Chicago, IL, USA).

3 Results

A. Patient characteristics and Group comparisons

The demographics of the study population are summarized in Table 1. The HCM group was older but body surface area was similar as compared with control group. There were significant differences in LV function and mass between the patient and control groups (Table 1). For the group comparison, HCM group had a significant higher averaged ECV compared to that in control group (27.5 ± 4.9% vs. 25.0 ± 2.3%, $p < 0.001$). This finding was similar in averaged WT between HCM and control groups (11.3 ± 5.1 mm vs. 6.0 ± 2.3 mm, $p < 0.001$).

Table 1 Study population characteristics

	HCM(n = 125)	Control (n = 58)	p-value
Age (y)	58. ± 16	51. ± 14	$p < 0.05$
BSA (kg/m^2)	1.77 ± 0.2	1.67 ± 0.2	$p = 0.026$
ECV	27.5 ± 4.9	25 ± 2.3	$p < 0.001$
WT (mm)	11.3 ± 5.1	6 ± 2.2	$p < 0.001$
LV MASS	170.4 ± 76.2	97.3 ± 31.1	$p < 0.001$
LVEDV	94.7 ± 26.4	102.7 ± 22.6	$p < 0.001$
LVESV	18.5 ± 17	25.9 ± 12.5	$p < 0.001$
nLVEDV	53.6 ± 14.6	60.7 ± 11.9	$p < 0.001$
nLVESV	10.5. ± 10.1	15.3 ± 6.9	$p < 0.001$
CI	2876 ± 537	3313 ± 585	$p < 0.001$
LVEF	82.3. ± 9.8	75.9 ± 7.7	$p < 0.001$
LVPER	−4.9 ± 1.3	−3.8 ± 0.7	$p < 0.001$
LVPFR	3.9 ± 1.5	4.6 ± 1	$p < 0.001$

BSA, Body Surface Area; ECV, Extracellular Volume Fraction; WT, Myocardial Wall Thickness; LV, left ventricular; EDV, end-diastolic volume; ESV, end-systolic volume; nLVEDV, normalized LVEDV; CI, cardiac index; EF, ejection fraction; PER, peak ejection rate; PFR, peak filling rate.

B. Extracellular Volumes and Wall thickness

The regional ECV and regional WT measurements from the four different regions in each group are listed in Table 2. For regional comparisons, the septal region had the highest ECV compared with the other three regions in all the groups. To further investigate the correlation between the myocardial ECV and WT, we performed linear correlation analysis for each group. Our results demonstrated that the regional ECV significantly correlated with the regional WT in HCM group ($r = 0.381$, $p = 0.0001$) (Fig. 1). In contrast, no significant correlation ($r = 0.139$, $p = 0.297$) was found between regional ECV and WT in control group.

Table 2 The regional ECV and wall thickness in HCM group

	HCM(n = 125)	Controls(n = 58)	p-value
ECV(A) (%)	27 ± 4.9	24.4 ± 2.8	$p < 0.001$
ECV(S) (%)	28.5 ± 5.4	25.7 ± 2.3	$p < 0.001$
ECV(P) (%)	27.9 ± 5.6	25.3 ± 3.2	$p < 0.001$
ECV(L) (%)	26.5 ± 4.9	24.5 ± 2.6	$p < 0.001$
WT (A) (mm)	11.4 ± 6.7	4.8 ± 2.2	$p < 0.001$
WT (S) (mm)	14.5 ± 6.6	8 ± 3.1	$p < 0.001$
WT (P) (mm)	9.6 ± 5.0	5.5 ± 2.3	$p < 0.001$
WT (L) (mm)	9.5 ± 5.4	5.5 ± 2.2	$p < 0.001$

ECV, Extracellular Volume Fraction; WT, Myocardial Wall Thickness; A, anterior; S, septal; P, posterior; L, lateral.

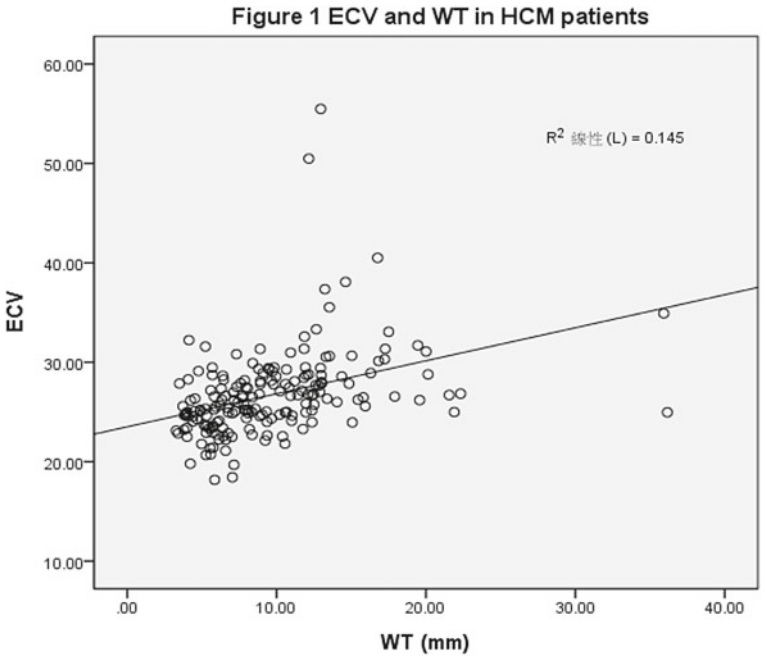

Fig. 1 Linear regression between the averaged ECV (extracellular volume fraction) and the averaged WT (wall thickness) in HCM group (N = 125)

4 Discussion

In this study, we demonstrated that CMR-derived ECV was significantly correlated with the myocardial wall thickness. This finding suggests that LVH is significant associated with the severity of DMF in patients with HCM. Myocardial fibrosis is defined as a significant increase in the collagen content in the myocardium. HCM are known to develop diffuse, as well as regional myocardial fibrosis. Once fibrosis develops, it increases myocardial stiffness and eventually deteriorates diastolic and systolic functions [17, 18].

Our results also showed that ECV varies with the myocardial region, suggested that regional ECV may lead to clinically significant errors if ECV was assessed and compared in different myocardial regions. Therefore, caution must be exercised in estimating the ECV in patients with significant ventricular hypertrophy.

5 Study Limitations

First, our study was done with a single T1 pulse sequence (MOLLI). Different sequences of T1 mapping have been reported to yield different absolute ECV values.

Whether our findings are identical in different pulse sequences is unknown and needs further investigation. Second, regional variation of ECV was only performed in one representative mid-ventricular slice, future studies should consider apical and basal slices for more comprehensive assessments. Third, although all subjects were carefully controlled in data acquisition and analysis, our results do not have histological evidence to support the suggestion that this interregional variation of ECV reflects a pathophysiological difference rather than a technical difference.

6 Conclusions

In conclusion, our study demonstrated that CMR-derived ECVs vary with myocardial region in patient with HCM. This interregional variation is associated with the severity of ventricular hypertrophy. Regional ECV is feasible for differentiating myocardial abnormalities and the position of the ROI is essential for comparing ROIs within the same region.

Acknowledgements I'm very grateful to my teacher, Mr. Mao-Yuan Su. He taught me a lot about MRI. He also helped me with this research project. I would like to thank Mr. Chiu for his constant encouragement and guidance.

Conflict of Interest The authors declare that they have no conflict of interest.

References

1. Maron BJ (2002) Hypertrophic cardiomyopathya systematic review. JAMA 287(10):1308–1320. https://doi.org/10.1001/jama.287.10.1308
2. Maron BJ et al (2003) American college of cardiology/European society of cardiology clinical expert consensus document on hypertrophic cardiomyopathy: a report of the American college of cardiology foundation task force on clinical expert consensus documents and the European S. J Am Coll Cardiol 42(9):1687–1713. https://doi.org/10.1016/S0735-1097(03)00941-0
3. Alcalai R, Seidman JG, Seidman CE (2008) Genetic basis of hypertrophic cardiomyopathy: From bench to the clinics. J Cardiovasc Electrophysiol 19(1):104–110. https://doi.org/10.1111/j.1540-8167.2007.00965.x
4. Seidman CE, Seidman JG (2011) Identifying sarcomere gene mutations in HCM: a personal history. Breast Dis 108(6):1–15. https://doi.org/10.1161/CIRCRESAHA.110.223834.Identifying
5. Richard P et al (2003) Hypertrophic cardiomyopathy distribution of disease genes, spectrum of mutations, and implications for a molecular diagnosis strategy. https://doi.org/10.1161/01.CIR.0000066323.15244.54
6. M. S.Maron *et al.*, "Hypertrophic Cardiomyopathy Phenotype Revisited After 50 Years With Cardiovascular Magnetic Resonance," *J. Am. Coll. Cardiol.*, vol. 54, no. 3, pp. 220–228, 2009, doi: https://doi.org/10.1016/j.jacc.2009.05.006.
7. Klues HG, Schiffers A, Maron BJ (1995) Phenotypic spectrum and patterns of left ventricular hypertrophy in hypertrophic cardiomyopathy: morphologic observations and significance as

assessed by two-dimensional echocardiography in 600 patients. J Am Coll Cardiol 26(7):1699–1708. https://doi.org/10.1016/0735-1097(95)00390-8
8. Maron BJ, Rowin EJ, Udelson JE, Maron MS (2018) Clinical spectrum and management of heart failure in hypertrophic cardiomyopathy. JACC: Heart Failure 6(5). Elsevier Inc., pp. 353–363. https://doi.org/10.1016/j.jchf.2017.09.011
9. Ellims AH, Iles LM, Ling LH, Hare JL, Kaye DM, Taylor AJ (2012) Diffuse myocardial fibrosis in hypertrophic cardiomyopathy can be identified by cardiovascular magnetic resonance, and is associated with left ventricular diastolic dysfunction. J Cardiovasc Magn Reson 14(1):1. https://doi.org/10.1186/1532-429X-14-76
10. Moon JC (2017) Left ventricular hypertrophy revisited cell and matrix expansion have disease-specific relationship. Circulation 136:2519–2521. https://doi.org/10.1161/CIRCULATIONAHA.117.029895
11. Lazzeroni D, Rimoldi O, Camici PG (2016) From left ventricular hypertrophy to dysfunction and failure focus reviews on heart failure. Circ J 80. https://doi.org/10.1253/circj.CJ-16-0062
12. Lovic D et al (2017) Left ventricular hypertrophy in athletes and hypertensive patients. J Clin Hypertens 19:413–417. https://doi.org/10.1111/jch.12977
13. Mewton N, Liu CY, Croisille P, Bluemke D, Lima JAC (2011) Assessment of myocardial fibrosis with cardiovascular magnetic resonance. J Am Coll Cardiol 57(8):891–903. https://doi.org/10.1016/j.jacc.2010.11.013
14. Kellman P, Hansen MS (2014) T1-mapping in the heart: accuracy and precision. https://doi.org/10.1186/1532-429X-16-2
15. Messroghli DR, Greiser A, Fröhlich M, Dietz R, Schulz-Menger J (2007) Optimization and validation of a fully-integrated pulse sequence for modified look-locker inversion-recovery (MOLLI) T1 mapping of the heart. J Magn Reson Imaging 26(4):1081–1086. https://doi.org/10.1002/jmri.21119
16. Wong TC et al (2012) Imaging association between extracellular matrix expansion quantified by cardiovascular magnetic resonance and short-term mortality. https://doi.org/10.1161/CIRCULATIONAHA.111.089409
17. RMA (1998) Pathologic fibrosis and connective tissue matrix in left ventricular hypertrophy due to chronic arterial hypertension in humans. J Hypertens Jul, 6(7):1031–1041. https://doi.org/10.1097/00004872-199816070-00018
18. Su MYM et al (2014) CMR-verified diffuse myocardial fibrosis is associated with diastolic dysfunction in HFpEF. JACC Card Imag 7(10):991–997. https://doi.org/10.1016/j.jcmg.2014.04.022
19. Brouwer WP et al (2014) In-vivo T1 cardiovascular magnetic resonance study of diffuse myocardial fibrosis in hypertrophic cardiomyopathy. J Cardiovasc Magn Reson 16(1):1–7. https://doi.org/10.1186/1532-429X-16-28

Upconversion Nanoformulation for Functional Imaging

Surojit Chattopadhyay, Sandip Ghosh, Najim Akhtar, De-Ming Yang, Chuan Lin Chen, and Ren-Shyan Liu

1 Introduction

Biomolecular imaging techniques is a powerful tool for diagnosis of cancers, and may have high specificity and sensitivity [1]. Among different varieties of metallic/metaloxide nanoparticles, upconversion nanoparticles (UCNPs) are superior for fluorescence imaging as they shows anti-Stokes shifted emission upon low energy NIR excitation, and are extremely stable even in physiological conditions [2]. The visible fluorescence that forms the basis of bioimaging with the UCNPs can be tuned from blue to red by changing the dopant type and concentration to suit multiplexing and has been reported before. The NIR excitation of these UCNPs result is negligible autofluorescence that increases the imaging contrast. The fluorescence in the UCNPs are also accompanied by non-radiative decay that results in heat in the UCNPs. This heat can also be imaged using a simple infrared thermal camera. On the other hand, the size and composition of the UCNPs promote easy cellular uptake, and offers minimum cytotoxicity. The easy incorporation of rare-earth ions such as Gd^{3+} and Yb^{3+} into UCNPs makes them active under magnetic resonance imaging (MRI) [3] and computed tomography (CT) [2]. Besides, they also provide an excellent platform for further functionalization [2] to combine with radio isotopes for single-photon emission computed tomography (SPECT) or positron

S. Chattopadhyay (✉) · S. Ghosh · N. Akhtar
Institute of Biophotonics, National Yang Ming Chiao Tung University, Taipei 112, Taiwan
e-mail: sur@nycu.edu.tw

D.-M. Yang
Microscopy Service Laboratory, Basic Research Division, Department of Medical Research, Taipei Veterans General Hospital, Taipei 112, Taiwan

C. L. Chen · R.-S. Liu
Department of Biomedical Imaging and Radiological Sciences, National Yang Ming Chiao Tung University, Taipei 112, Taiwan

© The Author(s), under exclusive license to Springer Nature Switzerland AG 2022

K.-P. Lin et al. (eds.), *Future Trends and Challenges of Molecular Imaging and AI Innovation*, Springer Proceedings in Physics 272,
https://doi.org/10.1007/978-3-030-92786-8_5

emission tomography (PET) imaging, in order to improve the sensitivity of diagnosis. Such unique properties of these UCNPs makes them ideal candidate for the multimodal imaging which is essentially required to acquire biological information for identifying cancer at an early stage. UCNPs also found applications in photoenabled therapies. Overall, a control over the chemistry, surface functionalization, and knowledge of the photophysics in these UCNPs opens up a wide range of possibilities for biomedical applications.

In this work, we have done functional modification of the UCNPs with select proteins to achieve FRET which can be used for intracellular pH imaging. Next, we have modified the UCNP with another chelator (chl) protein and loaded radioisotopes therein to make the nanoformulation work as multimodal imaging agents.

2 Experimental Part

A. *Synthesis of UCNPs*

First, oleic acid (OA) capped UCNPs (dispersible in cyclohexane) were synthesized following a published report [4]. Typically, $GdCl_3$ (80%), $YbCl_3$ (18%), $ErCl_3$ (2%) were mixed with 14 mL of OA and 16 mL of octadecene in a three-necked flask, and heated to 150 ˚C under nitrogen atmosphere. Subsequently, 10 mL of methanol solution of NaOH (2.5 mmol) and NH_4F (4 mmol) is added dropwise while stirring for 30 min maintaining reaction temperature at 50 ˚C. Finally, the mixture was heated to 300 ˚C for 1 h, and washed with ethanol, and the precipitate redispersed in cyclohexane.

Next, the OA-capping was replaced with citrate (Cit-UCNPs) to make the UCNPs hydrophilic by ligand exchange reaction [5].

B. *Synthesis of mOrange fluorescent proteins and construction of UCNPs-mOrange FRET nanoprobes*

The His6-tagged mOrange fluorescent proteins were derived from pRSET-b mOrange plasmid. mOrange proteins were expressed in E. coli (BL21) competent cells. Later, we lysed the bacterial cell membrane, by performing mechanical lysis, using mechanical probe sonicator. Finally, we collected the proteins after centrifugation of the sample and purifird under known protocols. The Cit-UCNP-mOrange FRET nanoprobes were constructed via EDC (1-ethyl-3-(3-dimethylaminopropyl) carbadimide) (Sigma Aldrich, USA) chemistry [6]. For the FRET nanoprobe construction, we have used 2 mL of Cit-UCNPs (1.5 mg/mL) with 2 mL of mOrange FPs (0.35 mg/mL), and 3 mL of EDC (6 mg/mL) were incubated overnight at 4 ˚C with gentle shaking (200 rpm).

III. *Conjugation of radioisotope specific chelator (chl)*

1 mg of EDC was added into 5 mL aqueous solution of cit-UCNPs (0.2 mg/ml), and the solution was stirred at 340 rpm for 1 h at room temperature. 2 mg of as-purchased

Tc specific chelator was then added into the solution, and the solution was stirred under 200 rpm for 8 h at room temperature. The obtained UCNP@chl, formulation was collected by centrifuging the resultant mixture at 15,000 rpm for 30 min with the precipitation re-dispersed in 5 mL deionized water. $SnCl_2$ (1 mg/ml) and Tc-pertechnetate in DI water were sequentially added to the UCNP@chl solution and allowed to react for 30 min with shaking at room temperature. The precipitate of ^{99m}Tc labeled UCNP@chl (UCNP@chl-^{99m}Tc) was redispersed in 0.5 mL DI water for final use.

IV. *Characterization of UCNPs*

The morphology and crystal structures were imaged by High Resolution Transmission Electron Microscope (HR-TEM, JEM-2010F, JEOL, Japan). Fluorescence spectra were recorded by a Fluorolog spectrophotometer (JY Fluorolog 3 with iHR 320, Horiba, Japan), equipped with a 980 nm cw laser excitation (SDL, China). For the FRET imaging, we have used an inverted fluorescence microscope (Zeiss Axiovert 200) equipped with a 980 nm cw laser (CNI, China), and compatible optics and a wide-view dual-mode CMOS camera (Hamamatsu, Japan) to record high resolution images. 2 ml of as prepared UCNP@chl-^{99m}Tc (1 mg/mL) was taken in a quartz cuvette and 980 nm laser (SDL-5000 T, Shanghai, China) was used to observe the UCL. For the UCL imaging, the external 980 nm laser (SDL-5000 T, Shanghai China) along with optical fiber and a 10 mm laser collimator was installed in the IVIS (Xenogen IVIS 50, PerkinElmer, Inc. Massachusetts, U.S.A.).

E. *Cellular uptake and Intracellular pH imaging.*

For in situ calibrations of the pH nanoprobes, 100 μL of nanoprobe solution were incubated with HeLa cells (10^4 cells/well) for 24 h at 37 ˚C, and 5% CO_2. Later, intracellular pH was adjusted to that of the extracellular pH environment controlled by an ionophore 'Nigericin' (481,990, Calbiochem, Merck, USA). For this purpose, HeLa cells (incubated with UCNP-mOrange nanoprobes) were washed (by 1 × PBS) and incubated in pH (3.0, 5.0, and 7.0) controlled citrate/phosphate buffer medium. Afterwards, each well was treated with 20 μM of Nigericin and incubated for another 30 min at 37 ˚C, and 5% CO_2 before heading for the microscopic imaging.

3 Results and Discussion

A. Materials characterisations of UCNP, mOrange, and UCNP-mOrange FRET nanoprobes.

The UCNP formulation is schematically shown in Fig. 1. Figure 2 represents the morphological and FRET characteristics of UCNP-mOrange nanoprobes. Figure 2a shows the TEM image of Cit-UCNPs. The average size of this nanoparticles is 15 nm. Inset in Fig. 2a shows a colloidal solution of Cit-UCNPs (dispersed in DI water) emitting green upconversion luminescence (UCL) under 980 nm laser excitation.

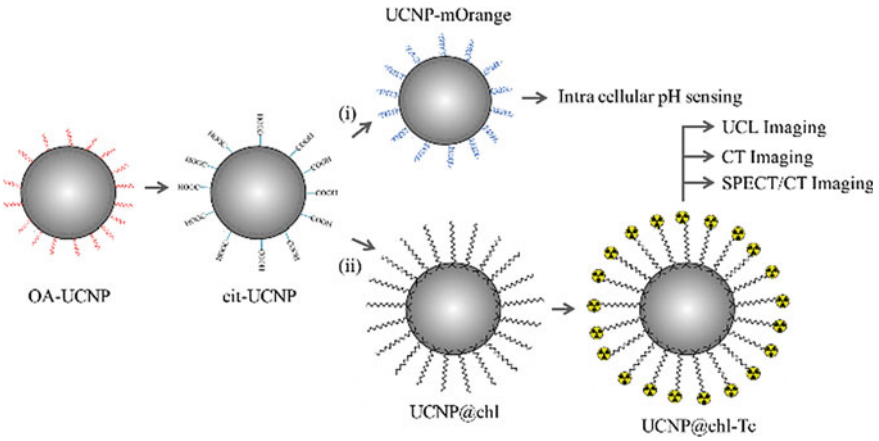

Fig. 1 Schematic of the UCNP formulation: (i) UCNP-mOrange for pH imaging, and (ii) UCNP-chl-Tc for multimodal imaging

Figure 2b, shows the HR-TEM image of a single UCNP-mOrange nanoprobe. Under TEM, the UCNPs (yellow circle) appears darker than a layer of mOrange protein coated outside (red circle). The overall size of the nanoprobe has increased to 25 nm because of the mOrange protein shell of 4.8 nm thickness around Cit-UCNPs.

Figure 2c shows the spectral overlap between UCNP (FRET donor) emission, and mOrange (FRET acceptor) excitation spectrum. We can observe that the broad excitation spectrum of mOrange fluorescent proteins is straddling the green emission band of Cit-UCNPs, satisfying the first condition of FRET. Figure 2d presents the spectroscopic FRET characteristics of UCNP-mOrange nanoprobe. Under the illumination of 980 nm laser, 5 distinct emission band has been observed. Out of these bands, peaks at 520, 521, 540, and 548 nm resembles to the characteristic peaks of UCNPs, and emission peak it 566 nm corresponds to the sensitized emission from mOrange fluorescent proteins. The confirmation of energy transfers between UCNPs and mOrange fluorescent protein is therefore established.

3.1 Intercellular pH Sensing Using UCNP-MOrange FRET Nanoprobe

Next, in addition to spectroscopic confirmation of FRET, we have investigated the in-vitro FRET imaging under different pH environment. To demonstrate the sensitivity of the nanoprobes to estimate the intracellular pH accurately, we have used Nigericin to modulate the intracellular pH with that of extracellular medium. Figure 3 presents the FRET images of HeLa cells in different pH (7.0, 5.0, and 3.0) buffers. The use of Nigericin ionophore would ensure an identical pH value inside and outside of the cells.

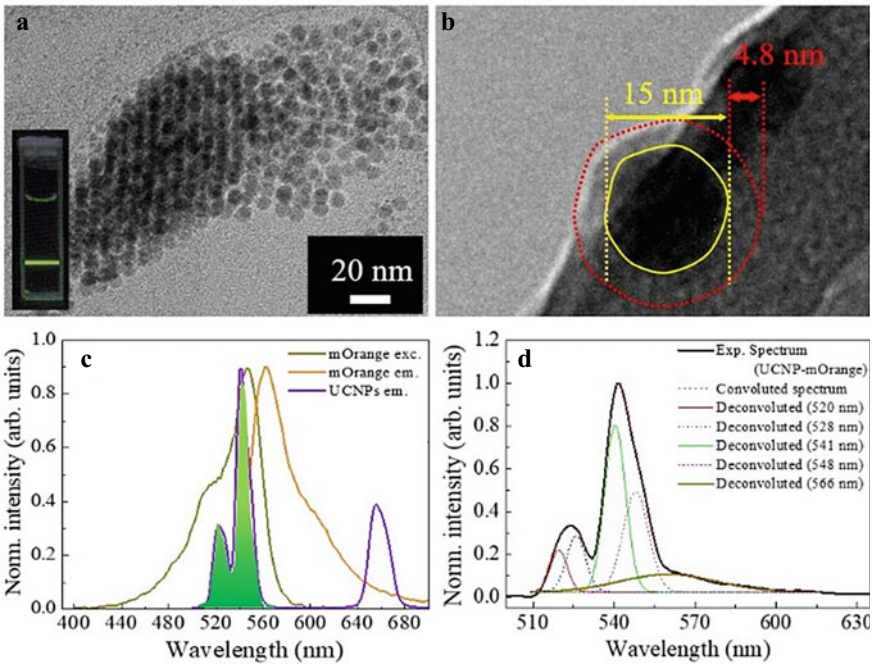

Fig. 2 Morphology and FRET characteristics of UCNP-mOrange nanoprobes. **a** TEM image of Cit-UCNPs. Inset shows a colloidal solution of Cit-UCNP (DI water) emitting green emission when illuminated with 980 nm laser. **b** High-resolution TEM image of a single UCNP-mOrange nanoprobe. The yellow circle shows the single Cit-UNCP, and a layer or mOrange protein with red circle. **c** Spectral overlapping between the emission of FRET donor (Cit-UCNPs), excitation of FRET acceptor (mOrange), respectively. **d** Convoluted and deconvolution FRET emission spectrum of UCNP-mOrange, under the excitation of 980 nm laser, which shows a sensitized emission band at 566 nm, and is coming from mOrange FPs. Reproduced with permission from Ref [7]. Copyright 2020 Elsevier B.V.

At alkaline pH (7.0, Fig. 3a), we could observe the individual signals from both UCNPs (green channel), and mOrange (red channel) from the nanoprobes uptaken in the HeLa cells. The FRET ratio (red to green channel signal) obtained is ~ 0.71. For the case of mildly acidic pH (5.0, Fig. 3b), the FRET intensity ratio dropped to ~ 0.52 as mOrange loses their ability to absorb energy from UCNP. At the high acidic pH (~3.0, Fig. 3c), the FRET ratio is observed to as low as ~ 0.30. Other than the drop in the FRET ratio at low pH, the overlay emission color has also been affected. The inactivity of the mOrange protein in acidic pH (3.0) would decrease the energy transfer efficiency making the emission green (Fig. 3c) dominated by the UCNPs. In basic pH, the emission will be relatively orange (Fig. 3a). The above results indicate that the UCNP-mOrange FRET nanoprobes can be used for accurate estimation of intracellular pH.

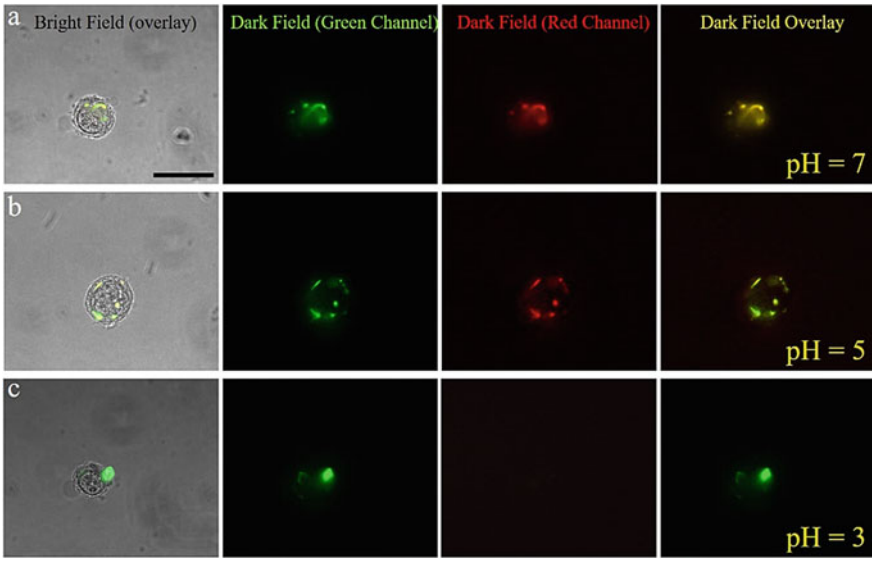

Fig. 3 Nigericin mediated in situ pH imaging in HeLa cells. Fluorescence imaging of UCNP-mOrange nanoprobes internalized HeLa cell(s) with nigericin modulated pH of **a** 7.0, **b** 5.0, and **c** 3.0, respectively. From left to right (L to R): Bright field image, green (UCNP) channel, red (mOrange) channel, and dark field overlay of the red and green channel images. Common scale bar of 10 μm. Reproduced with permission from Ref [7]. Copyright 2020 Elsevier B.V.

3.2 Multimodal Imaging Using UCNP-chl-^{99m}Tc Nanoformulation

Multi-modal imaging property of the UCNP@chl-^{99m}Tc is demonstrated by observing the UCL from the nanoformulation dispersed in water under 980 nm laser irradiation (Fig. 4a). UCL property of this nanocomposite was further investigated under small animal in vivo imaging system (IVIS) where only water containing glass vial shows no signal (Fig. 4b) under GFP filter, however, the vial containing 1 mg/mL of UCNP@chl-^{99m}Tc nanoformulation shows strong luminescence (Fig. 4c).

The Eppendorf containing the UCNP formulation without the radiolabel ^{99m}Tc (Fig. 4d) only shows the CT contrast because of the Yb^{3+} content in the formulation. The final formulation with the radio label (UCNP@chl-^{99m}Tc) shows strong SPECT signals (Fig. 4e). These results show proof-of-concept that the formulation could be used for multimodal imaging.

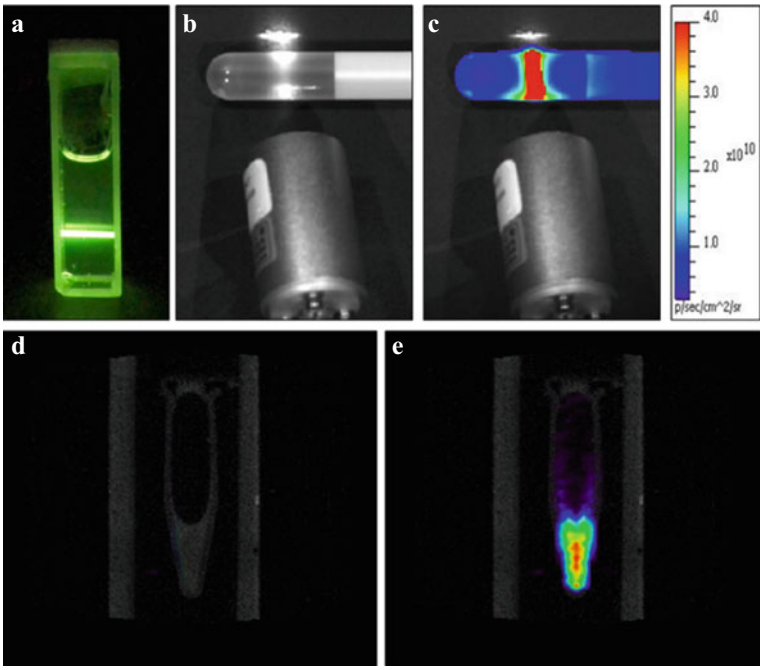

Fig. 4 Multimodal imaging of UCNP@chl-^{99m}Tc formulation. **a** Picture of quartz cuvette containing green fluorescent UCNP@chl-^{99m}Tc solution upon 980 nm irradiation. UCL image of glass vial containing **b** water, and **c** UCNP@chl-^{99m}Tc in water; laser power = 1 W. SPECT/CT image of **d** UCNP@chl and **e** UCNP@chl-^{99m}Tc

4 Conclusions

In conclusion, we demonstrate two UCNP based nanoformulation having functional imaging capabilities under deep penetrating 980 nm illumination. First, we have constructed a highly sensitive FRET based nanoprobe using UCNP as the donor and mOrange fluorescent protein as the acceptor. The UCNPs are internalized in HeLa cells. Upon changing the cellular pH by using an ionophore the emission from the UCNP-mOrange conjugate change from green at acidic pH and orange at alkaline pH. This UCNP based FRET imaging provides accurate estimation of intracellular pH. The results are reproducible, stable, and reversible indicating usability in early detection of cancer and other pH malfunctions in cells.

The second nanoformulation showed strong green fluorescence image contrast under 980 nm excitation. The component Yb^{3+} in the host $NaGdF_4$ of the UCNP makes the nanoformulation CT active. Radiolabelling of the UCNP obtained by chelating Tc in the protein network enabled SPECT/CT imaging. In short, the UCNP nanoformulation could demonstrate multimodal imaging.

Acknowledgements The authors would like to thank Ministry of Science and Technology, Taiwan (MOST-107-2112-M-010-003-MY3) for the research funding.

Conflict of Interest The authors declare no conflict of interest.

References

1. Ashok AH, Mizuno Y, Howes OD (2019) Tobacco smoking and dopaminergic function in humans: a meta-analysis of molecular imaging studies. Psychopharmacology 236(4):1119–1129
2. Gupta A, Lam CW, Wu CT, Yang DM, Chattopadhyay S (2018) Photothermal disintegration of 3T3 derived fat droplets by irradiated silica coated upconversion nanoparticles. Part Part Syst Charact 35:1800294
3. Bi H, He F, Dai Y, Xu J, Dong Y et al (2018) Quad-model imaging- guided high-efficiency phototherapy based on upconversion nanoparticles and ZnFe2O4 integrated graphene oxide. Inorg Chem 57(16):9988–9998
4. Ghosh S, Chiang WC, Fakhri MY, Wu CT, Chen RS, Chattopadhyay S (2020) Ultrasensitive broadband photodetector using electrostatically conjugated MoS_2-upconversion nanoparticle nanocomposite. Nano Energy 67:104258
5. Cao T, Yang T, Gao Y, Yang Y, Hu H, Li F (2010) Water-soluble $NaYF_4$:Yb/Er upconversion nanophosphors: synthesis, characteristics and application in bioimaging. Inorg Chem Commun 13:392–394
6. Dennis AM, Rhee WJ, Sotto D, Dublin SN, Bao G (2012) Quantum dot-fluorescent protein FRET probes for sensing intracellular pH. ACS Nano 6:2917–2924
7. Ghosh S, Chang YF, Yang DM, Chattopadhyay S (2020) Upconversion nanoparticle-mOrange protein FRET nanoprobes for self-ratiometric/ratiometric determination of intracellular pH, and single cell pH imaging. Bios Bioelectron 155:112115

Three-Dimensional Tomography of Cellulose Nanofibers- Polypeptides Nanocomposite Hydrogels

Tzu-Yi Yu, Yun-Hsiu Tseng, Ming-Chung Wu, Cheng-Si Tsao, and Wei-Fang Su

1 Introduction

In tissue engineering, researchers employ biomaterials to accelerate the rate of self-regeneration of damaged tissues [1–4]. This approach is practical if the biomaterials are similar to the environment supporting the target cells [5]. Extracellular matrix, ECM, is the matter between cells. It balances the chemical environment between cells, supports cell growth, and provides stimuli to guide cell differentiation. Most of the polymeric biomaterials for tissue engineering can hardly mimic both the microstructure and the biochemical environment of ECM. Recently, a type of nanomaterial derived from nature cellulose called "cellulose nanofiber" is an emerging ECM-mimic biomaterials. Cellulose nanofibers, CNFs, are synthesized by applying physical and chemical treatments to nature cellulose, such as woods and pulps [6]. This nanomaterial features its tunable crystallinity and surface chemistry according to the physical and chemical treatments during its synthesis [7–9]. Though many groups reported its excellent biocompatibility and applied CNFs hydrogels in tissue engineering, so far, these CNFs hydrogels crosslinked by cationic ions lack of biochemical stimuli leading to malfunction organoids [10–12]. Here, a new CNFs hydrogel system crosslinked with polypeptides is proposed to demonstrate the possibility of combining a synthetic polypeptide in CNFs hydrogels. In this research, the CNFs hydrogels were crosslinked with two types of crosslinkers—calcium cation (from calcium chloride, $CaCl_2$) and poly L-lysine-*random*-L-glutamic acid (PLLGA). The

T.-Y. Yu · Y.-H. Tseng · W.-F. Su (✉)
Department of Materials Science and Engineering, National Taiwan University, Taipei, Taiwan
e-mail: suwf@ntu.edu.tw

M.-C. Wu
Department of Chemical and Materials Engineering, Chang-Gung University, Taoyuan, Taiwan

C.-S. Tsao
Institute of Nuclear Energy Research, Longtan, Taoyuan, Taiwan

© The Author(s), under exclusive license to Springer Nature Switzerland AG 2022

K.-P. Lin et al. (eds.), *Future Trends and Challenges of Molecular Imaging and AI Innovation*, Springer Proceedings in Physics 272,
https://doi.org/10.1007/978-3-030-92786-8_6

effect of crosslinker types on the CNFs hydrogels' microstructure in different scale was studied using four imaging techniques: small angle X-ray scattering (SAXS), scanning electron microscope (SEM), transmission X-ray microscope (TMX), and polarized optical microscope (POM).

2 Materials and Method

A. Nomenclature

CNF stands for "cellulose nanofiber", $PLL_{80}GA_{20}$ (or PLLGA) stands for the random copolymer of L-lysine and glutamic acid in the ratio of 4 to 1. CNF is the main component of hydrogels, and PLLGA is a synthetic polypeptide as one of crosslinkers to CNF hydrogel. The CNF hydrogel crosslinked by PLLGA is named CNF/PLLGA. Similarly, the CNF hydrogel crosslinked by $CaCl_2$ is named CNF/$CaCl_2$. POM is the abbreviation to "polarized optical microscope", and SAXS represents "small angle x-ray scattering".

B. Materials and Hydrogel Fabrication

The calcium chloride was used as purchased. PLLGA was synthesized by the ring-opening polymerization (ROP) and the hydrolysis of protecting groups. The detail of PLLGA synthesis refers to the literature [13]. The numbers of PLLGA repeating units were controlled around 100 ~ 150. The CNFs suspension was synthesized with TEMPO oxidation and $NaBH_4$ reduction. Before fabricating the CNFs hydrogels, the crosslinkers ($CaCl_2$ and PLLGA) were dissolved in DI water to prepare the crosslinker solution in 50 mM effective charge concentration.

The CNFs hydrogels were fabricated with the dropped method reported in the literature about CNFs hydrogels [10, 12, 14]. The crosslinker solution was gently dropped in the container with CNFs suspension to form the CNFs hydrogels. After immersion for one night, the supernatant was removed, and the CNFs hydrogel was immersed in DI water for another night to remove the excessive crosslinker. The CNFs composite hydrogels were prepared with 1 ml of CNFs suspension and 2 ml of crosslinker precursors.

C. Polarized Optical Microscope

The hydrogels were observed under POM (DM 2500 M, LEICA). To prevent the hydrogels from desiccation, they were immersed in DI water before characterization. In this research, the hydrogels were characterized under two modes: "Cross Polar" and "Cross Polar + Compensator". In cross-polar mode, the polarity of analyzer was vertical to of polarizer. While the black region represents amorphous or isotropic crystal phases, the white area represents anisotropic structure from oriented polymer chain or, in this study, nanofibers. By adding a compensator in the light path, the orientation of microstructures was distinguished by their colors. Purple regions were amorphous or isotropic crystals. In blue areas, polymer chains or nanofibers

were oriented from right-up to left-down in images. For those in orange areas, their orientation is from left-up to right-down.

D. Small Angle X-Ray Scattering

The transmission SAXS data of CNFs hydrogels were obtained at 23A work station in National Synchrotron Radiation Research Center, NSRRC. The beam energy was 15 keV, the sample-to-detector distance was 3.875 m, and the q range was from 0.005 Å-1 to 0.35 Å-1. For good SAXS results, hydrogels' desiccation should be prevented, and the hydrogel samples should be characterized in minutes. The 2D SAXS pattern was further converted into 1D integral by software. The background transmission and scattering image were necessary for 1D integration. The SAXS 1D integral can be fitted by the following Eq. (1), which combines Ornstein–Zernike model and wormlike chain model [15–17].

$$I(q) = \frac{l_1}{1 + q^2\xi^2} + p(q) \tag{1}$$

E. Transmission X-Ray Microscope

The transmission X-ray microscope data of CNFs hydrogels were obtained at the 1B work station in National Synchrotron Radiation Research Center, NSRRC, Taiwan. For the X-ray tomography study, the aqueous hydrogel sample was stained with 0.1% w/v ruthenium tetroxide in ddH2O to enhance the hydrogels' contrast. After 3 h of staining, the sample was washed with methanol. Tear off a hydrogel piece with a thickness of about 14 ~ 17 μm to fix on the holder by polyamide tape. 20 μl gold particle solution (400 ~ 500 nm) was added to the hydrogel as the rotation target. The sample was rotated from -75° to 75°. The 3D structure was reconstructed by computer simulation through 151 cross-section images taken per degree by TXM.

3 Results and Discussion

A. Nanometer-scale Structure of CNF Hydrogels

SAXS is a nanostructure characterization method based on the x-ray scatter resulted from the electron density between phases in materials. Since CNF hydrogels comprise two phases, dense cellulose nanofibers and water in interconnected pores, the 2D scatter patterns present the reciprocal structure of CNF hydrogels network. In literature, a fibrous hydrogel network can be fitted with Eq. (1) [17]. The first term in equation represents the structure factor (fibers network structure), and the slope in low q region ($q < 0.01$ Å^{-1}) is related to the hydrogel mesh size (ξ). The smaller mesh size (ξ) results in the slope in low region (b) closer to -2. In Fig. 1a, the slope of CNF/PLLGA is close to the one of pristine CNF, high than -1. However, the CNF hydrogel crosslinked by $CaCl_2$ exhibits a slope close to -2. It indicates that $CaCl_2$ leads to a CNF network with a smaller mesh size (ξ). This structural change is a

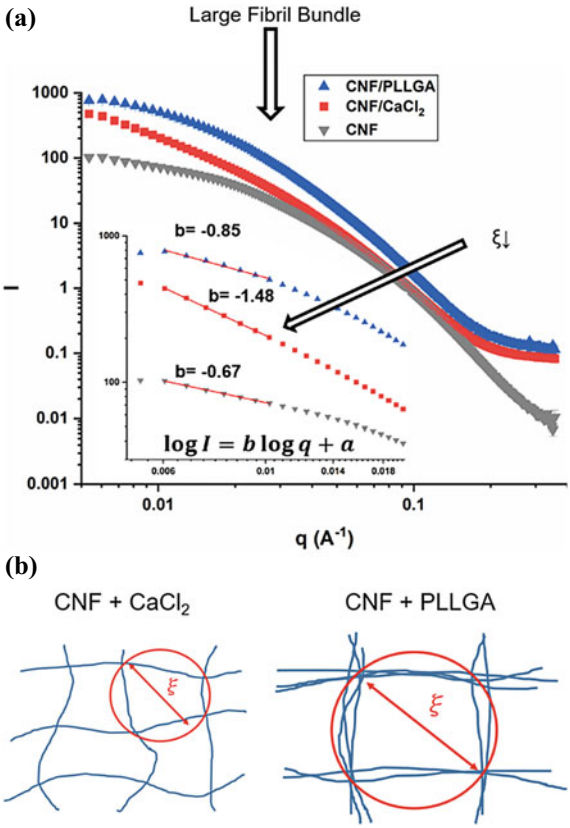

Fig. 1 Microstructure of CNF hydrogel in nanometer scale. **a** SAXS 1D integral of CNFs hydrogels crosslinked by different crosslinker precursors under 50 mM effective charge concentration. The slope at low-q region is related to the mesh size of network,ξ. **b** Simplified illustration of $CNF/CaCl_2$ and CNF/PLLGA. CNF assembles into bundles after adding PLLGA while CNF forms dense network after adding $CaCl_2$

typical result when polymer backbones are crosslinked by adding crosslinkers. On the other hand, the CNF/PLLGA SAXS result suggests a different hydrogel network structure from typical polymeric hydrogels. The second term in Eq. (1) is credited to the morphology of individual CNFs. Because it shows stronger scattering in middle q region, CNF/PLLGA SAXS result leads to a hypothesis that CNFs assembled into bundles when they crosslinked by PLLGA. Two CNF hydrogel networks resulted from either $CaCl_2$ or PLLGA are summarized in Fig. 1b. The network structure difference might lead to different physical properties, such as mechanical strength and water content.

B. Micrometer Scale Structure of CNF Hydrogels

Freeze-dried hydrogel samples are commonly used for structural analysis under scanning electron microscope. The morphologies of dried $CNF/CaCl_2$ and CNF/PLLGA hydrogels are shown in Fig. 2a and b, respectively. In SEM images, the type of crosslinkers has no significant effect on hydrogel structure in network morphologies. However, these images might not present the real network structure due to the distortion of hydrogel structure during sample preparation. To prepare SEM imaging

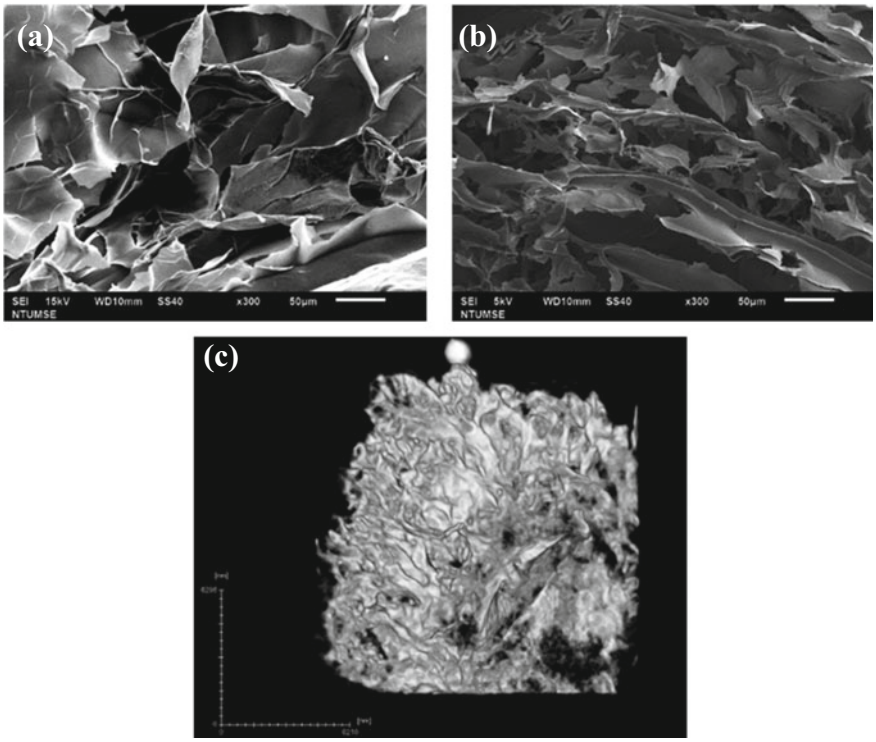

Fig. 2 Interconnected porous structure in CNF hydrogels in the micrometer scale. SEM image of (**a**) CNF/$CaCl_2$ hydrogels and (**b**) CNF/PLLGA. Scale bar represents 50 μm in (**a**) and (**b**). (**c**) Reconstructed 3D model of CNF/$CaCl_2$ hydrogel from Transmission X-ray Microscope. Scale bar represents 6 μm

sample, hydrogel samples have to be frozen and lyophilized to remove water. Ice crystallization brings distortion to its network structure. Scientist still use the pore size in hydrogel SEM image to estimate the hydrogel network density.

Transmission X-ray Microscope (TXM) is an emerging technique to construct hydrogel network images without distortion. In TXM, hydrogel samples are located on a rotatory holder, and the images are collected with different x-ray incident angles. 3D tomography structure of hydrogels can be constructed by compiling these images with a numerical method. In Fig. 2c, the 3D tomography model of CNF/$CaCl_2$ is shown. The hydrogel samples were immersed in a ruthenium tetroxide aqueous solution to enhance contrast. Thus, the region in white represents the interconnected pore filled with water. Comparing with morphology in Fig. 3a, CNF/$CaCl_2$ exhibits high network density and, unlike the flake structure in the SEM image, anomalous CNF domains in TXM. Because hydrogels can be observed by TXM under ambient conditions, the structural distortion during freeze-drying can be prevented. It leads to a realistic image of three-dimensional hydrogel networks in the micrometer scale.

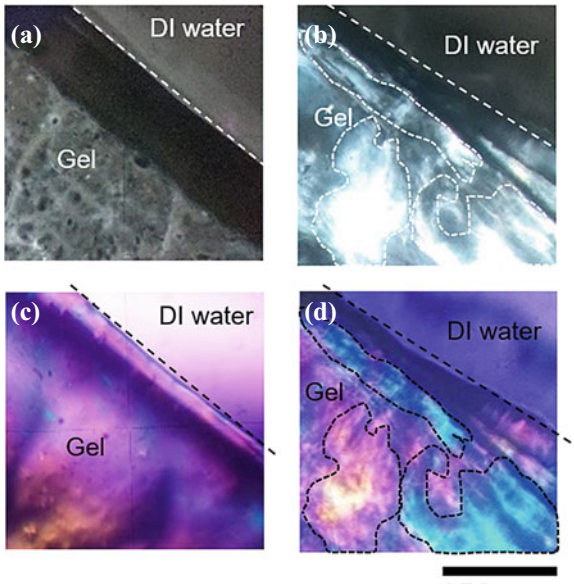

Fig. 3 Birefringence domains in CNF/PLLGA hydrogel induced by PLLGA. Cross-polar image of (**a**) CNF/$CaCl_2$ and (**b**) CNF/PLLGA hydrogel without the compensator. Cross-polar image of (**c**) CNF/$CaCl_2$ and (**d**) CNF/PLLGA hydrogel with compensator. Scale bar represents 250 μm

C. CNF Hydrogels under Polarized Optical Microscope

Most polymeric hydrogels have little optical structure under an optical microscope because they are composed of random coil polymer chains without ordered structures. However, some exhibit birefringence under POM for their order molecular orientation or liquid–crystal-like microstructure [18]. When CNFs are oriented into an ordered structure, CNF hydrogels show such property for the cellulose anisotropic crystal domain within CNF [7, 8, 19]. In Fig. 3b, there are several birefringence regions (white region) in CNF/PLLGA hydrogel, while DI water (background) shows no optical signal. By adding a compensator in the light path, these birefringence regions can be distinguished into two domains in either blue or orange, labeling two orientations. On the other hand, there is no significant birefringence observed in CNF/$CaCl_2$ in Fig. 3a and c. This result supports the previous hypothesis - CNFs assembles into bundles after crosslinked by PLLGA- because CNFs must form ordered structures for birefringence. In contrast, CNFs remain single nanofibers after adding $CaCl_2$, so it shows no birefringence in POM.

4 Conclusions

Four structure characterization methods, SAXS, SEM, TXM, and POM, were used to investigate the crosslinker effect on CNF hydrogel network in different scales. Based on SAXS results, we made a hypothesis that CNFs assemble into bundles after crosslinked by PLLGA. Its birefringence confirmed this hypothesis in POM images.

This microstructural difference might lead to a substantial difference in the physical properties of CNF hydrogels. We also demonstrated using TXM 3D tomography on CNF/$CaCl_2$ hydrogel to construct its in situ network structure without distortion during sample preparation.

Acknowledgements This research was supported financially by the Ministry of Science and Technology (MOST), Taiwan, under Contracts MOST 108–2221–E–002–027–MY3.

Conflict of Interest The authors declare that they have no conflict of interest.

References

1. Shekaran A, Garcia AJ (2011) Biochimica et Biophysica Acta (BBA)-General Subjects 1810(3):350–360
2. Lu H, Hoshiba T, Kawazoe N, Chen G (2011) Biomaterials 32(10):2489–2499
3. Pratt AB, Weber FE, Schmoekel HG, Müller R, Hubbell JA (2004) Biotechnol Bioeng 86(1):27–36
4. Sell S et al (2007) Polym Int 56(11):1349–1360
5. Xu C, Inai R, Kotaki M, Ramakrishna S (2004) Tissue Eng 10(7–8):1160–1168
6. Chirayil CJ, Mathew L, Thomas S (2014) Rev Adv Mater Sci 37(1–2):20–28
7. Shak KPY, Pang YL, Mah SK (2018) Beilstein J Nanotechnol 9:2479–2498
8. Isogai A, Saito T, Fukuzumi H (2011) Nanoscale 3(1):71–85
9. Khatri Z, Mayakrishnan G, Hirata Y, Wei K, Kim I-S (2013) Carbohyd Polym 91(1):434–443
10. Zander NE, Dong H, Steele J, Grant JT (2014) Acs Appl Mater Inter 6(21):18502–18510
11. Yang J, Zhang XM, Ma MG, Xu F (2015) Acs Macro Lett 4(8):829–833
12. Basu A, Lindh J, Alander E, Stromme M, Ferraz N (2017) Carbohyd Polym 174:299–308
13. Blout ER, Idelson M (1958) J Am Chem Soc 80(18):4909–4913
14. Masruchin N, Park B-D, Causin V, Um IC (2015) Cellulose 22(3):1993–2010
15. Geng L et al (2017) Cellulose 24(12):5417–5429
16. Mao Y, Liu K, Zhan C, Geng L, Chu B, Hsiao BS (2017) J Phys Chem B 121(6):1340–1351
17. Schoenmakers DC, Rowan AE, Kouwer PHJ (2018) Nat Commun 9(1):2172
18. Wu ZL et al (2011) Macromolecules 44(9):3542–3547
19. Parker RM et al (2016) ACS Nano 10(9):8443–8449

Deep CNN with Conditional Random Field in Breast Cancer Metastasis Detection

Meilan Jimmy Hasugian, Ping-Yu Wu, Teng-Bin Chang, Bang-Hung Yang, Ren-Shyan Liu, Mei-Fen Chen, and Kang-Ping Lin

1 Introduction

In 2020, WHO released the global health estimates and reported that breast cancer is one of the top 10 leading causes of death among female in most of countries [1]. Early cancer diagnosis plays significant role in improving patients' survival rate [2]. One essential step in early breast cancer diagnosis is to detect metastasis in lymph nodes (Fig. 1 [3]) through analyzing the hematoxylin and eosin (H&E) stained histopathology slides. Whole slide images (WSIs) have been widely used to identify the normal and tumor cells [4], even more in localizing the malignant lesions (Fig. 2) [5]. However, examining extra-large WSIs (e.g., 20 GPixels) would impede the diagnosis process.

In this decade, the utilization of deep convolutional neural network (deep CNN) in computer vision problem has increased rapidly with a broad range from natural images to medical images [5].

M. J. Hasugian · P.-Y. Wu · T.-B. Chang · M.-F. Chen · K.-P. Lin (✉)
Department of Electrical Engineering, Chung Yuan Christian University, Taoyuan, Taiwan
e-mail: kplin@cycu.edu.tw

B.-H. Yang · R.-S. Liu
Department of Biomedical Imaging and Radiological Sciences, National Yang Ming Chiao Tung University, Taipei, Taiwan

Department of Nuclear Medicine and National PET/Cyclotron Center, Taipei Veterans General Hospital, Taipei, Taiwan

R.-S. Liu
Department of Nuclear Medicine, Cheng Hsin General Hospital, Taipei, Taiwan

M.-F. Chen · K.-P. Lin
Technology Translation Center for Medical Device, Chung Yuan Christian University, Taoyuan, Taiwan

© The Author(s), under exclusive license to Springer Nature Switzerland AG 2022

K.-P. Lin et al. (eds.), *Future Trends and Challenges of Molecular Imaging and AI Innovation*, Springer Proceedings in Physics 272,
https://doi.org/10.1007/978-3-030-92786-8_7

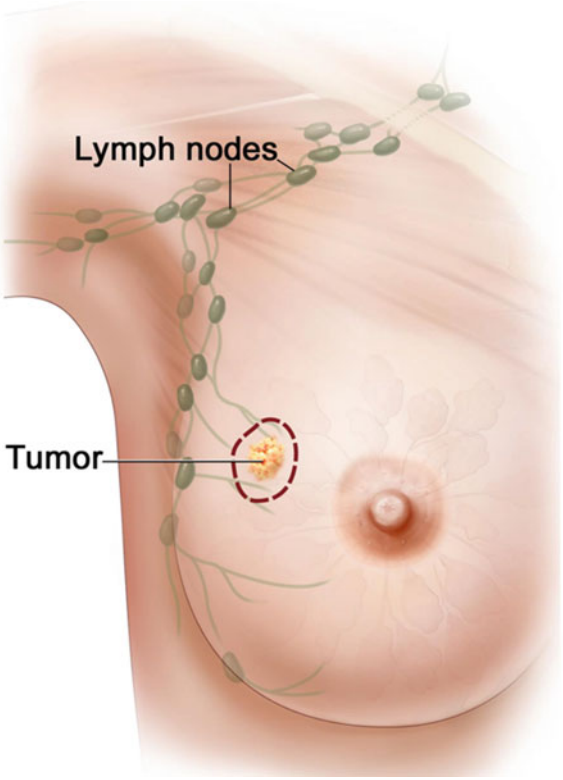

Fig. 1 Tumor and lymph nodes in breast cancer

Here, we present a deep learning-based approach combined with conditional random field for the identification of tumor metastasis from whole slide images of breast sentinel lymph nodes. In this study we compare performance several state-of-the-art CNNs models as feature extractor and combined with conditional random field (CRF) on the top as a framework to detect tumor metastasis in WSIs. Due to the extremely large size of the WSIs, every slide is segregated into numerous patches and perform the classification process on each patch independently. CRF is employed to preserve the spatial correlations between the adjacent classified patches.

To obtain the goals, every patch is divided into several sub-patches to retain the spatial connectivity during the training process. Then from these patches level predictions, tumor probability heatmaps is obtained to make the slide-based predictions dan tumor localization task.

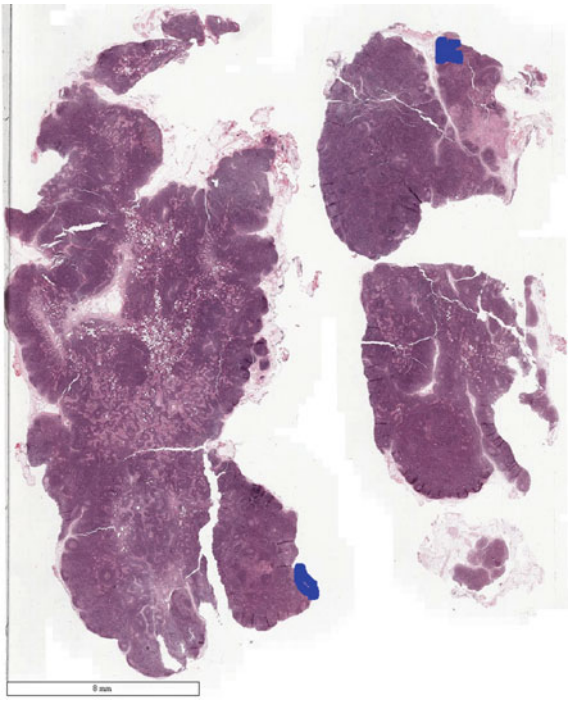

Fig. 2 Whole slide image with metastasis label (blue color)

2 Materials and Methods

A. Dataset

In this section, we describe the whole slide images provided in Camelyon16 dataset. The Camelyon16 dataset [6] consists of a total of 399 whole slide images (WSIs) split into 270 for training and 129 for testing. Both splits contain samples from two institutions (Radbound UMC and UMC Utrecht) with specific details provided in Table 1 [7].

The ground truth data for the training slides consists of a pathologist's delineation of metastatic tumor area on WSIs of sentinel lymph nodes. The ground truth (labels) data are provided in XML files format that contains annotated contours vertices of the metastases' location. Figure 3 shows the visualization of the tumor metastasis label on the top of WSI image.

Table 1 WSI in the Camelyon16 dataset

Institution	Train (normal)	Train (tumor)	Test
Radboud UMC	100 slides	70 slides	79 slides
UMC Utrecht	60 slides	40 slides	50 slides
Total	160 slides	110 slides	129 slides

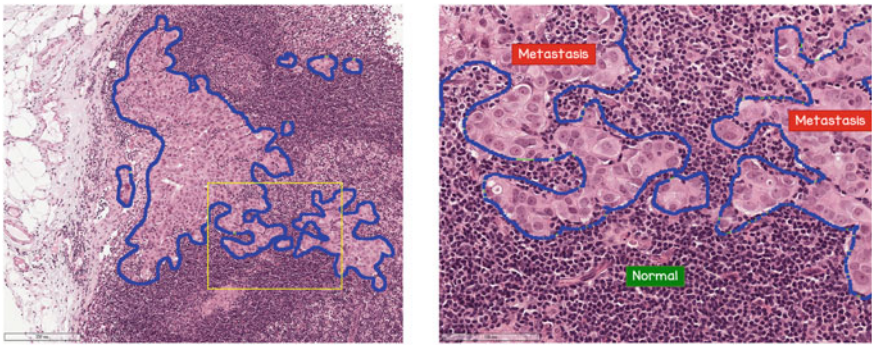

Fig. 3 Visualization of tumor metastasis label on the of a tumor slide image that contains the metastasis region and the normal region

As shown in the figure above, in the tumor slide image contains tumor metastasis region and the normal region.

B. Method

Mostly the WSIs have enormous numbers of pixels (around 100,000 × 200,000 pixels) that contains large area as the whitespace background. To focus the analysis, first we exclude the background and identify the tissue since the tumor metastasis exists in the tissue. This was achieved by implementing Otsu method [8] for each RGB channel then find the intersection between them.

Figure 4 shows the tissue area (right) from a slide image (left) as the focus in localizing the tumor metastasis. On average, approximately 85% of the WSI is the background region. Removing the background and aiming the process to the tissue area decreases the computation time.

To set up the patches for the training process, we randomly select 200,000 patches from tumor regions of tumor slides with size 768 × 768 pixels. For the normal patches we combined from normal slides and non-tumor regions from tumor slides total 200,000 patches with 768 × 768 pixels. The example of each patches is presented in Figs. 5 and 6.

Each patch is divided into nine sub-patches with size 256 × 256 pixels as the input of the model. In this study, we compare the impact of two frameworks in metastasis detection. The first framework is the baseline model with only using CNN as feature extractor then embedded the prediction into heatmap image as the prediction probability (Fig. 7).

In the feature extractor we deployed several well-known deep network architectures: VGG16 [9], GoogLeNet [10], ResNet-18 and ResNet-34 [11].

The second framework is depicted in Fig. 8. In this framework, a conditional random field (CRF) is added at the top of the baseline model. CRF is a probabilistic graphical model that used undirected graph representation and parameterization that encode a conditional distribution P(Y|X), where Y is a set of target variables given X

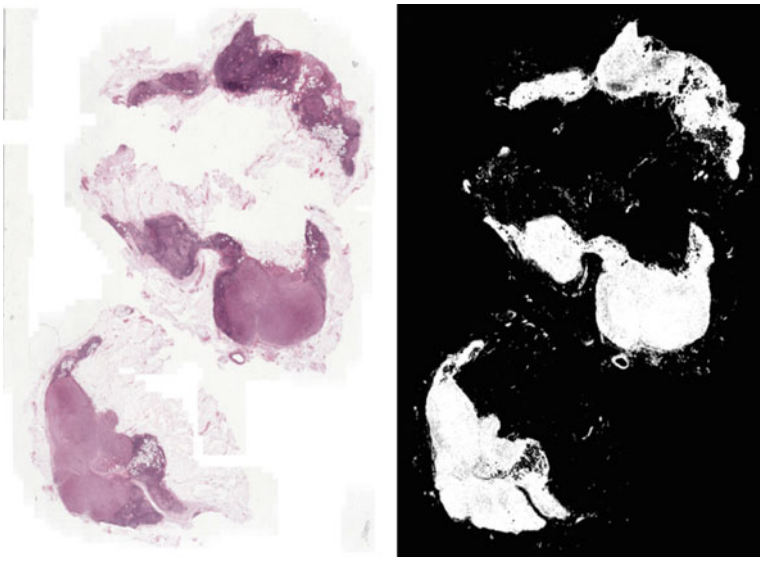

Fig. 4 The tissue area (right) as the focus of analysis, is obtained from the whole slide image (left)

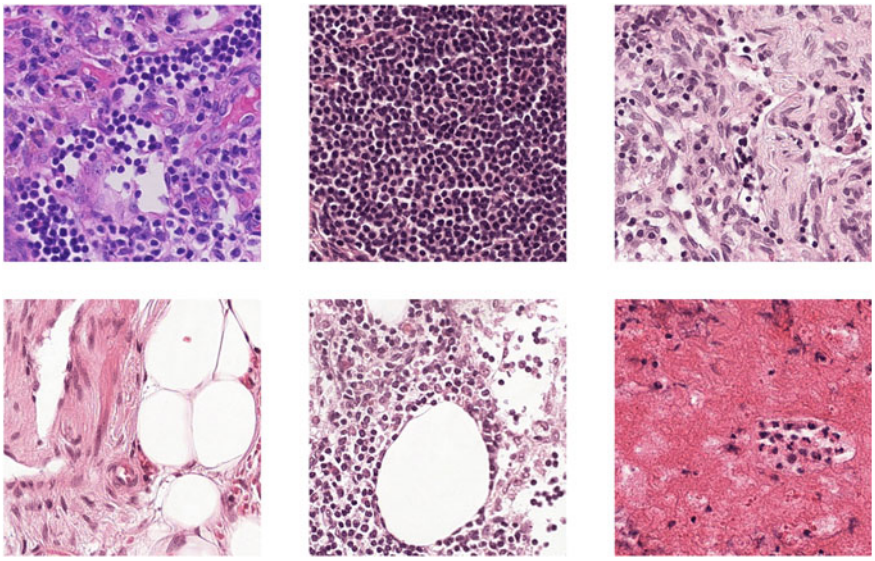

Fig. 5 Several patches from normal WSI

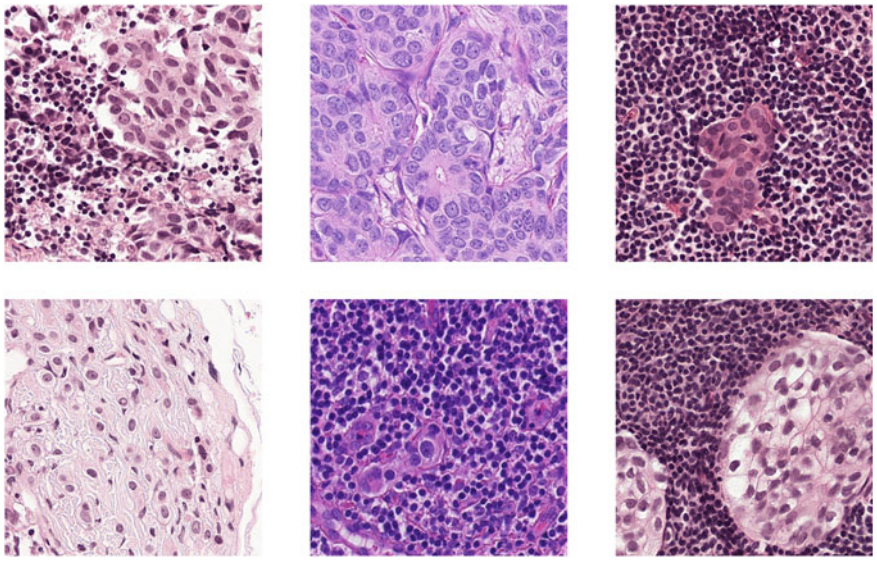

Fig. 6 Several patches from tumor WSI

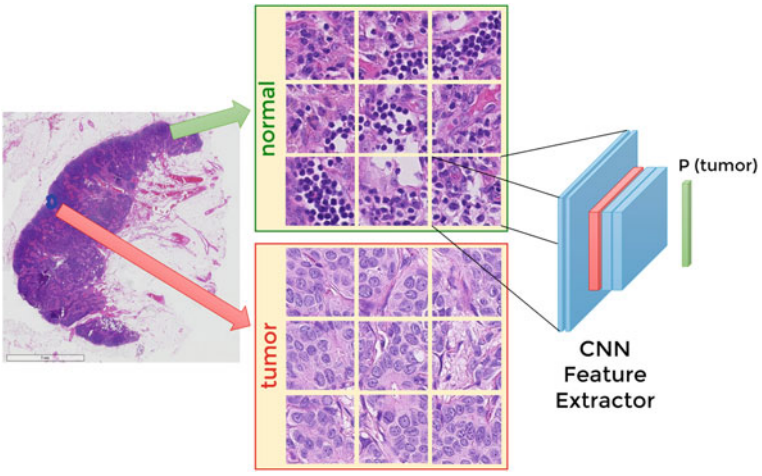

Fig. 7 The baseline model in metastasis detection

is a set of observed variables [12]. The image patches are divided into nine (N) sub-patches denoted as $x = \{x_i\}$ for $i = 1, \ldots, 9$. Let $Y = \{y_i\}$ be the random variables associated with sub-patches i, that represents the label of patch i takes a value of {*normal, tumor*}.

The conditional distribution P(Y|X) can be modeled as CRF with the Gibbs distribution of

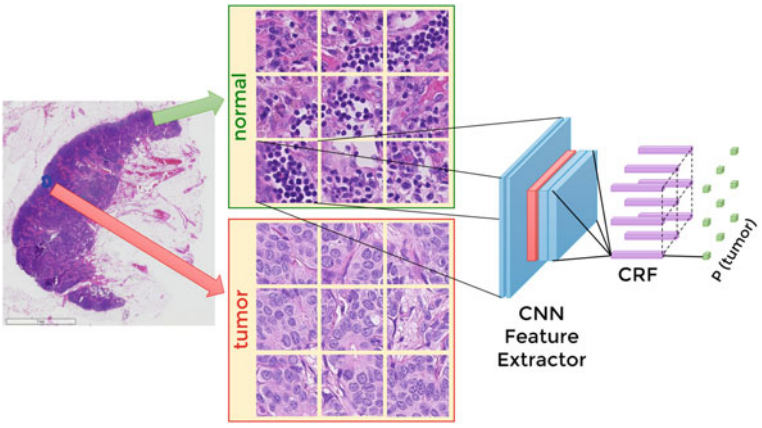

Fig. 8 The combination of deep CNN and CRF for metastasis detection

$$P(Y = y|x) = \frac{1}{Z(x)} e^{(-E(y,x))} \tag{1}$$

where E(y,x) is the energy function that measures the cost of Y taking a specific configuration y given x, and Z(x) is the partition function that insures P(Y = y | x) is a valid probability distribution. In the context of fully-connected CRF [13]. The energy function defined as:

$$E(y, x) = \sum_i \psi_u(y_i) + \sum_{i<j} \psi_p(y_i, y_j) \tag{2}$$

where i, j ranges from 1 to N. The unary potential $\psi_u(y_i)$ measures the cost of sub-patch i taking the label y_i given the sub-patch embedding x_i. The pairwise potential $\psi_p(y_i, y_j)$ measures the cost of jointly assigning sub-patch i, j with label y_i, y_j given the sub-patch embedding x_i, x_j. The pairwise potential models the spatial correlations between adjacent sub-patches.

3 Results

The framework was implemented with PyTorch 1.4.0 + cu92 and trained with NVIDIA GeForce RTX 2070 SUPER, 8 GB on the Ubuntu 20.04 LTS platform. The results of the baseline model with CRF on the slide Test_001 is displayed in Fig. 9. The patch classification accuracy of the baseline model and baseline + CRF on the validation slides dataset is presented in Table 2. The average free response receiver operating characteristic (FROC) score for the baseline model and baseline +

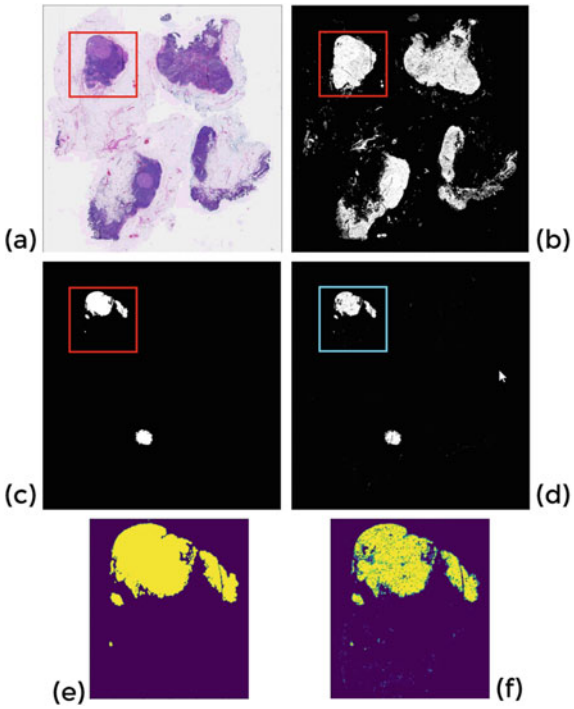

Fig. 9 The visualization on slide Test_001 **a** original slide, **b** tissue mask, **c** ground truth of tumor location, **d** the probability map using baseline model + CRF, **e** & **f** the ground truth and the probability map of the cropped box

Table 2 Patch classification accuracy on the validation slides

CNN	Baseline	Baseline + CRF
VGG16	0.8789 ± 0.0023	0.8809 ± 0.0021
GoogLeNet	0.8847 ± 0.0022	0.8924 ± 0.0021
ResNet-18	0.8903 ± 0.0022	0.8973 ± 0.0021
ResNet-34	0.8871 ± 0.0022	0.8910 ± 0.0021

CRF is reported in Table 3. The results show that the CNN baseline feature extractor is improved from the end-to-end joint training with CRF.

Table 3 Average FROC score on the test slides

CNN	Baseline	Baseline + CRF
VGG16	0.6989 ± 0.0113	0.6989 ± 0.0152
GoogLeNet	0.7102 ± 0.0112	0.7102 ± 0.0148
ResNet-18	0.7503 ± 0.0104	0.7503 ± 0.0139
ResNet-34	0.7391 ± 0.0107	0.7491 ± 0.0144

4 Conclusions and Discussion

In this study, we evaluated the influence of conditional random field on the top of CNN model for the detection of tumor metastasis on whole slide images. WSIs are the extra-large image with size around 20 GPixels. To reduce the computation time, each slide is randomly selected on the tumor and non-tumor region with size 768 × 768 pixels patch. This patch then divided into nine sub-patches with size 256 × 256 pixels to take the spatial correlation into consideration.

Compared to the baseline model, conditional random field enhances the ability of CNN feature extractor by integrating spatial correlations between adjacent sub-patches during the training process and improve the accuracy rate.

On the further development, increasing the numbers of patches image and including the borderline patch that contains tumor and non-tumor region is intuitively will enhance the accuracy together with taking more than nine sub-patches as well.

Conflict of Interest The authors declare that they have no conflict of interest.

References

1. WHO (2020) Global Health Estimates 2020: Deaths by Cause, Age, Sex, by Country and by Region, 2000–2019. Geneva, World Health Organization; 2020. https://www.who.int/data/gho/data/themes/mortality-and-global-health-estimates/ghe-leading-causes-of-death
2. Gecer B, Aksoy S, Mercan E et al (2018) Detection and classification of cancer in whole slide breast histopathology images using deep convolutional networks. Pattern Recogn 84:345–356
3. National Cancer Institute at https://www.cancer.gov/
4. Araujo T, Aresta G, Castro E et al (2017) Classification of breast cancer histology images using convolutional neural networks
5. Hou L, Samaras D, Kurc TM et al (2016) Patch-based convolutional neural network for whole slide image classification. In: IEEE conference on computer vision and pattern recognition 2016, pp 770–778
6. Camelyon Grand Challenge at https://camelyon16.grand-challenge.org
7. Bejnordi BE, Veta M et al (2017) Diagnostic assessment of deep learning algorithms for detection of lymph node metastases in women breast cancer. J Am Med Assoc:2199–2210
8. Otsu N (1979) A threshold selection method from gray-level histograms. IEEE Trans Syst Man Cybern 9(1):62–66
9. Simonyan K, Zisserman A (2015) Very deep convolutional networks for large-scale image recognition. In: ICLR 2015
10. Szegedy C, Liu W, Jia Y, Sermanet P et al (2015) Going deeper with convolutions. In: CVPR 2015
11. He K, Zhang X, Ren S, Sun J (2016) Deep residual learning for image recognition. In: Proceedings of the IEEE conference on computer vision and pattern recognition, pp 770–778
12. Koller D, Friedman N (2009) Probabilistic graphical models: Principles and techniques. MIT Press, Cambridge
13. Krähenbühl P, Koltun V (2011) Efficient inference in fully connected CRFS with Gaussian edge potentials. In: Advances in neural information processing systems, pp 109–117

Monitoring HDAC4 Expression in Alzheimer's Disease Using [^{18}F]TFAHA-PET

Yi-An Chen, Cheng-Hsiu Lu, Chien-Chih Ke, Chi-Wei Chang, Bang-Hung Yang, Juri G. Gelovani, and Ren-Shyan Liu

1 Introduction

Amyloid-β (Aβ) is widely considered as a key contributor to the pathophysiology of AD [1]. Despite various therapeutic approaches targeting Aβ through either secretase inhibitors or immunotherapy, the cognitive functions of patients failed to be

Y.-A. Chen · B.-H. Yang · R.-S. Liu
Department of Biomedical Imaging and Radiological Sciences, National Yang Ming Chiao Tung University, Taipei, Taiwan

Y.-A. Chen (✉)
Molecular and Genetic Imaging Core/Taiwan Mouse Clinic, National Comprehensive Mouse Phenotyping and Drug Testing Center, Taipei, Taiwan

C.-H. Lu
Core Laboratory for Phenomics and Diagnostics, Kaohsiung Chang Gung Memorial Hospital, Kaohsiung, Taiwan

Department of Medical Research, Kaohsiung Chang Gung Memorial Hospital, Kaohsiung, Taiwan

C.-C. Ke
Department of Medical Imaging and Radiological Sciences, Kaohsiung Medical University, Kaohsiung, Taiwan

Department of Medical Research, Kaohsiung Medical University Hospital, Kaohsiung, Taiwan

C.-W. Chang · B.-H. Yang · R.-S. Liu
PET center, Department of Nuclear Medicine, Taipei Veterans General Hospital, Taipei, Taiwan

J. G. Gelovani
Office of the Provost, United Arab Emirates University, P.O. BOX 1551, Al Ain, United Arab Emirates

R.-S. Liu
Department of Nuclear Medicine, Cheng Hsin General Hospital, Taipei, Taiwan

© The Author(s), under exclusive license to Springer Nature Switzerland AG 2022

K.-P. Lin et al. (eds.), *Future Trends and Challenges of Molecular Imaging and AI Innovation*, Springer Proceedings in Physics 272,
https://doi.org/10.1007/978-3-030-92786-8_8

improved effectively [2]. Recent findings indicated the abnormal epigenetic modifications contribute to the impaired learning and deterioration of memory [3]. Epigenetic dyregulation causes the widespread decline in gene expression through post-translational histone modifications including epigenetic modifying enzymes, histone deacetylases (HDACs) [4]. Among these histone-modifying enzymes, HDAC4, belongs to HDAC class IIa enzymes, is highly enriched in brain and its homeostasis is associated with regulating the transcription of synaptic plasticity-related gene, neuronal survival and neuron development [5]. Studies have shown that the nuclear HDAC4 level is markedly increased in brains of AD patients and the total HDAC4 levels are highly expressed in AD mouse model [6, 7]. It suggests that abnormal HDAC4 expression or its nuclear localization may contribute to learning and memory deficits.

Given that the importance of HDAC class IIa in epigenetic regulation involved in brain function and HDAC inhibitor treatments restore cognitive performance, it is necessary to develop molecular imaging agents for evaluation of HDACs activity in the brain. Consequently, this has led to the development of a second generation of HDAC class IIa–specific radiotracer, 6-(tri-fluoroacetamido)-1-hexanoicanilide ([^{18}F]TFAHA), which shows significantly higher selectivity for HDAC class IIa enzymes [8]. Recent study has described that PET imaging with [^{18}F]TFAHA enable quantitative assessment of HDAC class IIa enzymes expression-activity in intracerebral 9L and U87-MG gliomas in rats [9]. However, whether PET imaging with [^{18}F]TFAHA can be used to monitor HDAC class IIa enzymes in AD brain needs to be investigated.

The aim of this study is to investigate the role of HDAC4 using 3D human neural cell model of AD by analysis of expression and treatment of specific inhibitor. We also evaluate HDAC4 expression in 3xTg AD mice compared with age-matched WT mice by performing PET imaging with [^{18}F]TFAHA and immunohistochemical analysis. The results suggest that [^{18}F]TFAHA is a useful tool for in vivo monitoring epigenetic deregulation, especially HDAC4, in AD progression.

2 Materials and Methods

A. Establishment of 3D human neural cell culture model of AD and relevant assays

3D culture models were set up for subsequently IF and biochemical analysis according to the method described previously [10]. To further investigate the effects of Tasquinimod on neuronal memory and synaptic plasticity-related genes, 3D-differentiated FAD cells were treated with Tasquinimod at doses between 30 and 100 μM for 48 h. Subsequently, RT-qPCR for gene expression was performed.

B. Animals

3xTg-AD mice (JAX-34830) and age-matched control group were used in this study. All animal procedures were performed in accordance with the institutional guidelines for care and use of laboratory animals.

C. Small animal PET/CT imaging experimental procedures

In PET image study, each AD mouse and age-matched WT mouse was injected intravenously with 8.04 ± 0.75 MBq/0.1 ml of [^{18}F]TFAHA. Subsequently, regional retention and uptake of these radioligands were processed and analyzed with PMOD 3.5 software package (Pmod Technologies, Zu¨rich, Switzerland).

D. Immunofluorescent staining

Brain Sects. (10 μm) or cell culture slides were incubated with the primary antibodies followed by fluorescence conjugated secondary antibodies (Abcam) and DAPI. All slides were observed under a confocal fluorescence microscopy (Zeiss LSM 880).

E. Statistical analysis

Data were statistically analyzed with GraphPad Prism (Version 5.0; GraphPad, La Jolla, USA) using Student's *t* test or by a one-way ANOVA, followed by Tukey's post hoc test.

3 Results

A. In vivo monitoring of HDAC4 using [^{18}F]TFAHA in 3xTg AD

To monitor HDAC4 expression in AD progression, we performed PET imaging with [^{18}F]TFAHA in AD transgenic mouse and age-matched wild type mouse. 3xTg AD mouse model, which exhibits progressive Aβ deposition and age-related changes in neuropathologies, is suitable to observe the changes of HDAC4 with age. Visual interpretation of [^{18}F]TFAHA-PET results showed greater uptake of [^{18}F]TFAHA in the whole brains of 3xTg AD mice compared with age-matched WT mice at 8, 11 and 16 months of age (Fig. 1a–c). Higher uptake were found in 3xTg AD mice consistently, suggesting that [^{18}F]TFAHA-PET imaging could be used to differentiate AD and WT control.

All brains were further anatomically parcellated according to a standard atlas and [^{18}F]TFAHA uptake in each region of cortex, hippocampus, striatum, basal forebrain, thalamus and cerebellum was evaluated as for whole brain analysis (Fig. 2). The 3xTg AD mice exhibited significantly higher [^{18}F]TFAHA uptake in most areas examined, including hippocampus ($t = 3.45$, $p = 0.04$), basal forebrain ($t = 5.61$, $p = 0.0112$), thalamus ($t = 4.36$, $p = 0.0224$) and cerebellum ($t = 2.38$, $p = 0.146$) compared to wild-type mice. Despite the [^{18}F]TFAHA uptake in neither cortex ($t = 2.67$, $p = 0.12$) nor striatum ($t = 4.06$, $p = 0.056$) reached statistical significance, both of these two regions of 3xTg AD mice showed higher [^{18}F]TFAHA uptake.

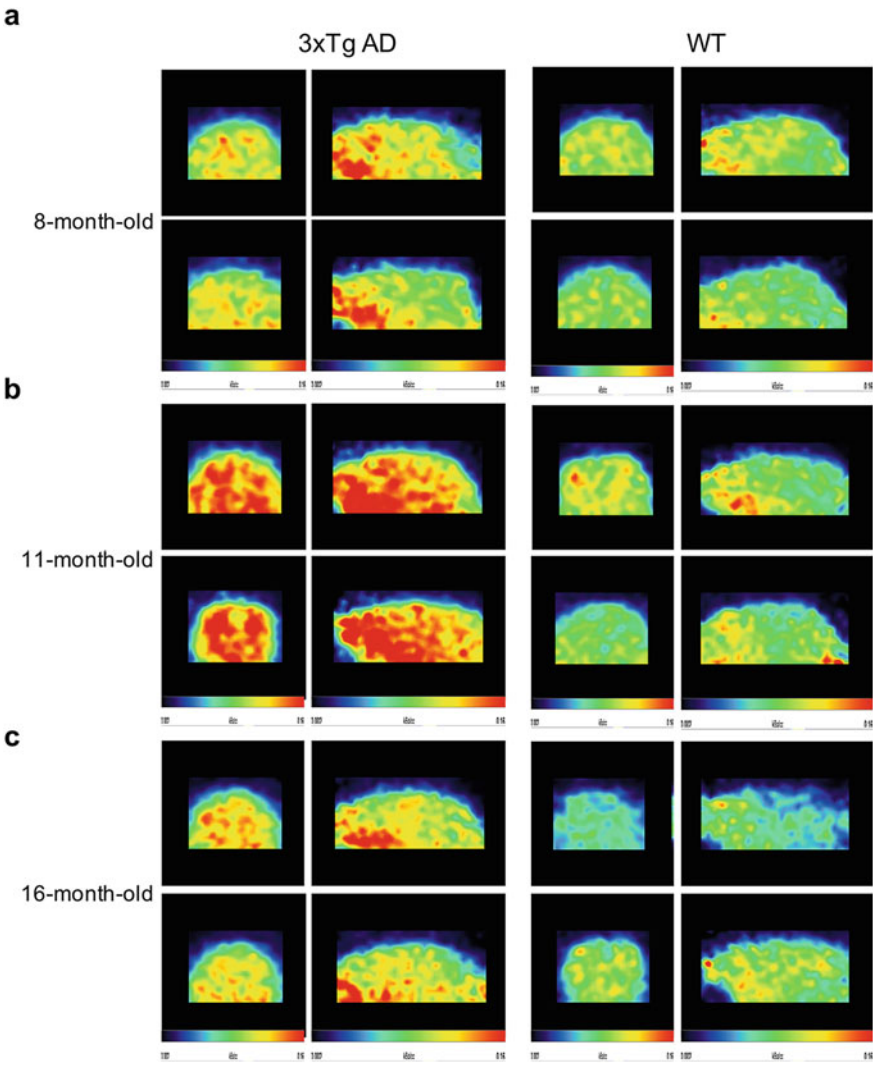

Fig. 1 In vivo PET imaging of HDAC4 using [^{18}F]TFAHA. Representative [^{18}F]TFAHA PET imaging of 3xTg AD mouse and WT mouse at **a** 8, **b** 11, **c** 16 months of age

To investigate whether the level of HDAC4 coincides with the uptake of [^{18}F]TFAHA, immunostaining with HDAC4 specific antibody was performed in brain sections. In line with the PET studies, differences in levels of HDAC4 were visually detectable between 3xTg AD and wild-type mice (Fig. 3).

B. In vitro characterization of HDAC4 expression in cell model of Alzheimer's disease

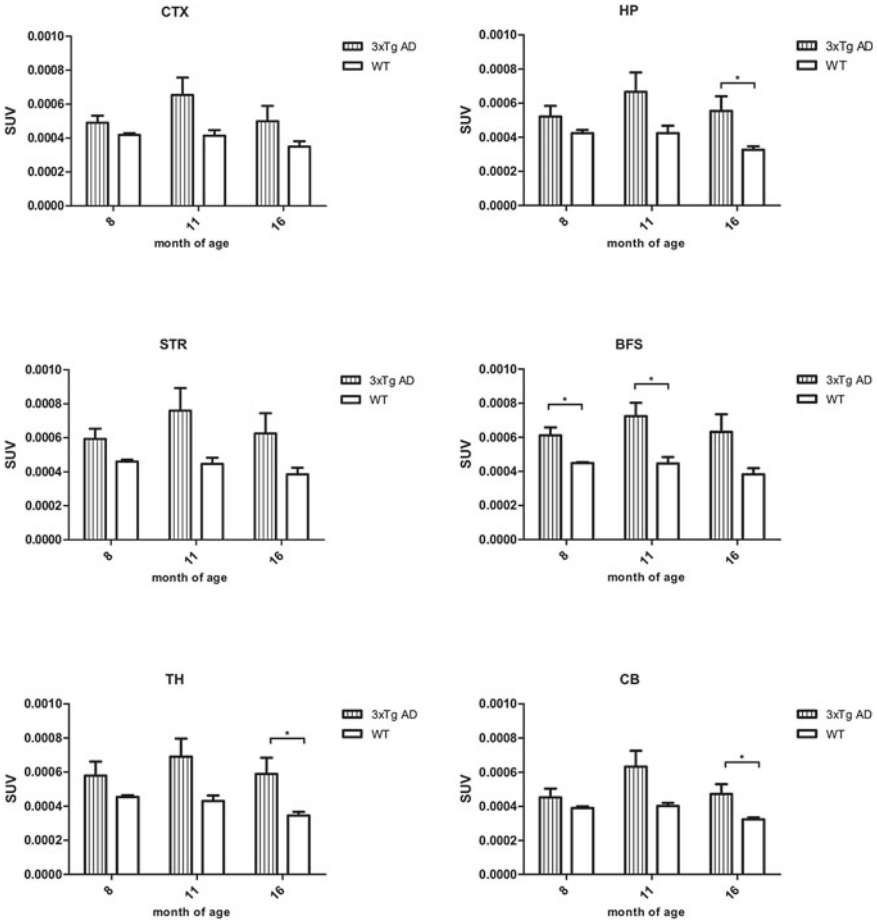

Fig. 2 The quantification of whole brain and different brain regions in SUV. SUV means standardized uptake value. Abbreviation: CTX, cortex; HP, hippocampus; STR, striatum; BFS, basal forebrain; TH, thalamus; CB, cerebellum

To investigate the HDAC4 expression following neuronal differentiation, a human neural cell culture model of AD that mimicked AD pathology by overexpressing human amyloid precursor protein with both Swedish (K670N/M671L) and London (V717I) FAD mutations in SH-SY5Y cell line was used (namely 3D-differentated FAD cells) in this experiment. IF staining and western blot analysis showed that HDAC4 was increased in 3D-differentated cells during neuronal differentiation either FAD or WT (Fig. 4a). By contrast, the level of HDAC1 remained largely unaffected. In addition, increased Hdac4 at the mRNA level was found in 3D-differentated FAD cells (Fig. 4b).

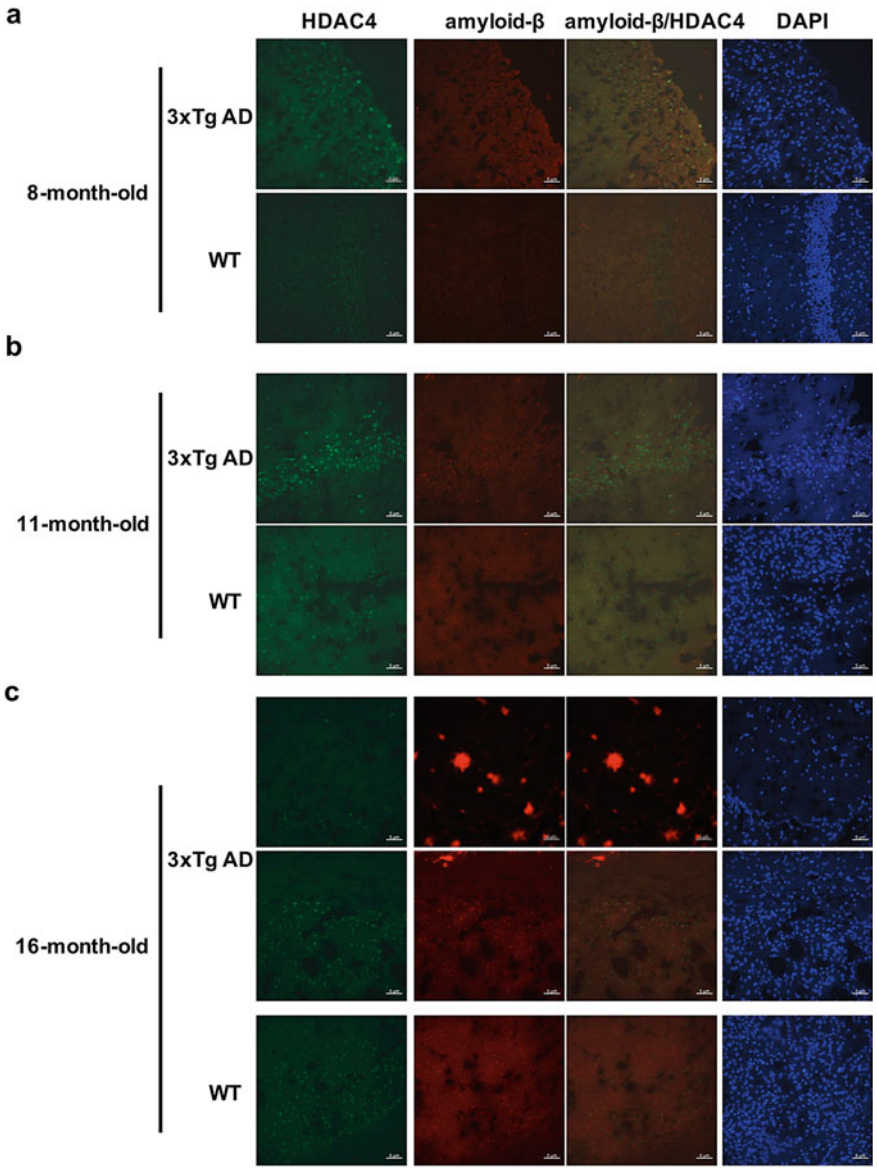

Fig. 3 Expression of HDAC4 and amyloid-β were increased in cortex of 3xTg AD mouse

C. HDAC4 inhibitor treatment up-regulates memory and synaptic plasticity-related genes

Given that the level of HDAC4 was elevated in cell model of AD, whether inhibition of HDAC4 can restore the levels of AD related affected genes is worthy of pursuit.

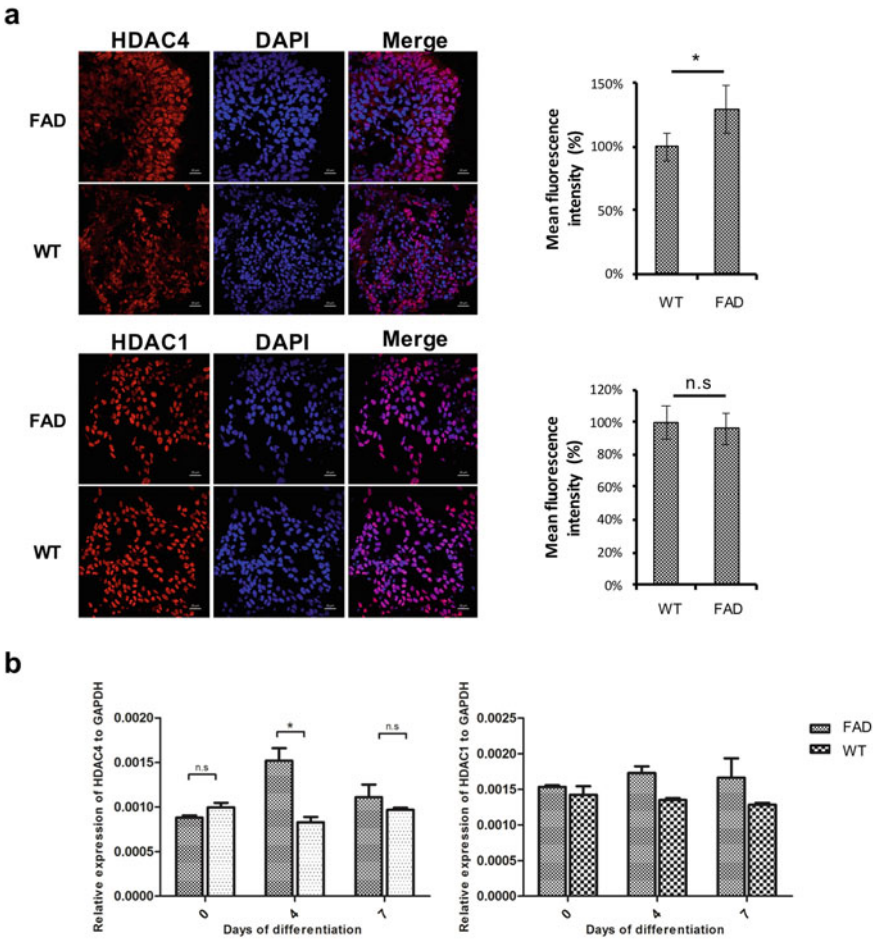

Fig. 4 The levels of HDAC4 are increased in 3D neural cell culture of AD

Tasquinimod (TasQ) is a highly specific inhibitor of HDAC4 and clinically tested oral antiangiogenic agent for therapy of castration-resistant prostate cancer. Herein, our study aimed to investigate the effect of TasQ on neuronal cells in AD. Quantitative RT-PCR analysis showed that TasQ upregulated several AD related affected genes and even dose-dependently increased the levels of Syn2, Homer1 and GluR2 (Fig. 5). Among these AD related affected genes, Lgi1, Syn2 and Homer1 belong to HDAC4 target genes [5]. Taken together, these data demonstrated that HDAC4 inhibitor treatment exhibited considerable therapeutic benefits on neuronal memory and synaptic plasticity-related genes in AD.

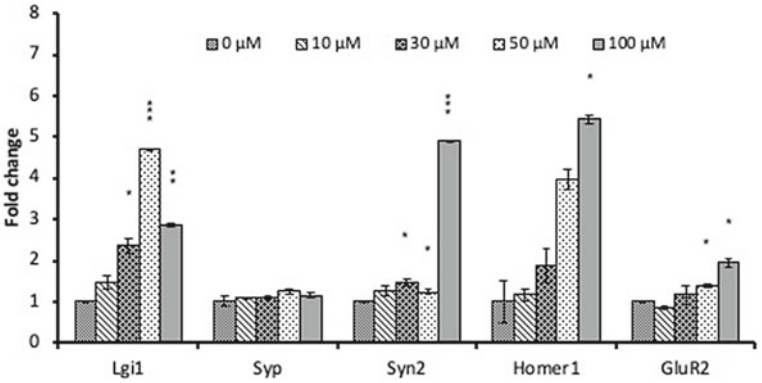

Fig. 5 HDAC4 specific inhibitor up-regulates memory and synaptic plasticity-related genes in SH-SY5Y FAD cells

4 Discussion

In this study, we demonstrated the important role that HDAC4 plays in Alzheimer's disease by analysis of its expression and treatment with specific inhibitor. These results validated that HDAC4 might be a promising for diagnosis and treatment of AD.

Despite higher uptake were found in 3xTg AD mice consistently, [^{18}F]TFAHA uptake was not positively correlated with the age (Fig. 4). We assumed that decreased level of HDAC4 at 16 months of age was attributed to neuronal loss. However, 3xTg AD mice were confirmed to expresses Aβ plaques and neurofibrillary tangles, as well as synaptic and behavioral deficits, except display significant neuronal loss [11]. [^{18}F]TFAHA-PET plus NeuN immunoreactivity and [^{18}F]FDG-PET to characterize AD pathology in 3xTg AD mouse model, may facilitate the development of AD research.

The variability of brain [^{18}F]TFAHA uptake at different age groups of AD mice was confirmed in current study. However, the progressive change of HDAC4 expression occurs in the same subject remains unknown. Thus, it is worthwhile to conduct longitudinal studies in mouse models of AD to better monitor and understand the events of epigenetic dysregulation throughout the course of the disease. Our data have shown that the level of HDAC4 coincides with the uptake of [^{18}F]TFAHA globally. However, owing to the limitation of μPET imaging for mouse brain, autoradiography assays can be used to evaluate the regional distribution and density of [^{18}F]TFAHA binding sites in the brains of the same mice that were imaged using PET.

There is growing evidence that aberrant HDAC expression and function leads to neuropathology. Previous studies showed that HDAC inhibitor specifically targeting class I, but not class IIa or IIb HDACs can significantly improve learning, memory and synaptic plasticity. Surprisingly, our results provided the first evidence that HDAC4 specific inhibition is also beneficial to AD related gene deficits. The therapeutic

effect of HDAC4 inhibition in AD transgenic mice needs to be investigated in terms of behavior and neuronal function.

5 Conclusions

Current studies demonstrated that brain [^{18}F]TFAHA uptake at different age groups of AD mice coincided with the level of HDAC4. Moreover, a significant therapeutic effect of HDAC4 specific inhibitor on neuronal cells was demonstrated by upregulation of memory and synaptic plasticity-related genes. Furthermore, PET imaging with novel histone deacetylase class IIa selective substrate-based radiotracer, [^{18}F]TFAHA revealed HDAC4 expression in aging AD brains, which may encourage the development of AD-related neuroimaging and therapy.

Acknowledgements The authors thank Prof. Yi-Chao Lee (Taipei Medical University, Taiwan) for kindly providing the mouse line. We thank the Taiwan Mouse Consortium-Molecular and Genetic Imaging Center, which is funded by the Ministry of Science and Technology (MOST) of Taiwan for technical support in PET imaging experiment.

Conflict of Interest The authors declare that they have no conflict of interest.

References

1. Korczyn AD (2008) The amyloid cascade hypothesis. Alzheimers Dement 4(3):176–178. https://doi.org/10.1016/j.jalz.2007.11.008
2. Cummings J, Lee G, Mortsdorf T, Ritter A, Zhong K (2017) Alzheimer's disease drug development pipeline: 2017. Alzheimers Dement (N Y) 3(3):367–384. https://doi.org/10.1016/j.trci.2017.05.002
3. Penney J, Tsai LH (2014) Histone deacetylases in memory and cognition. Sci Signal 7 (355):re12. doi:https://doi.org/10.1126/scisignal.aaa0069
4. Esposito M, Sherr GL (2019) Epigenetic modifications in Alzheimer's neuropathology and therapeutics. Front Neurosci 13:476. https://doi.org/10.3389/fnins.2019.00476
5. Sando R 3rd, Gounko N, Pieraut S, Liao L, Yates J 3rd, Maximov A (2012) HDAC4 governs a transcriptional program essential for synaptic plasticity and memory. Cell 151(4):821–834. https://doi.org/10.1016/j.cell.2012.09.037
6. Shen X, Chen J, Li J, Kofler J, Herrup K (2016) Neurons in vulnerable regions of the Alzheimer's disease brain display reduced ATM signaling. eNeuro 3(1). https://doi.org/10.1523/ENEURO.0124-15.2016
7. Anderson KW, Chen J, Wang M, Mast N, Pikuleva IA, Turko IV (2015) Quantification of histone deacetylase isoforms in human frontal cortex, human retina, and mouse brain. PLoS ONE 10(5):e0126592. https://doi.org/10.1371/journal.pone.0126592
8. Bonomi R, Mukhopadhyay U, Shavrin A, Yeh HH, Majhi A, Dewage SW, Najjar A, Lu X, Cisneros GA, Tong WP, Alauddin MM, Liu RS, Mangner TJ, Turkman N, Gelovani JG (2015) Novel histone deacetylase class IIA selective substrate radiotracers for PET imaging of epigenetic regulation in the brain. PLoS ONE 10(8):e0133512. https://doi.org/10.1371/journal.pone.0133512

9. Laws MT, Bonomi RE, Kamal S, Gelovani DJ, Llaniguez J, Potukutchi S, Lu X, Mangner T, Gelovani JG (2019) Molecular imaging HDACs class IIa expression-activity and pharmacologic inhibition in intracerebral glioma models in rats using PET/CT/(MRI) with [(18)F]TFAHA. Sci Rep 9(1):3595. https://doi.org/10.1038/s41598-019-40054-2
10. Kim YH, Choi SH, D'Avanzo C, Hebisch M, Sliwinski C, Bylykbashi E, Washicosky KJ, Klee JB, Brustle O, Tanzi RE, Kim DY (2015) A 3D human neural cell culture system for modeling Alzheimer's disease. Nat Protoc 10(7):985–1006. https://doi.org/10.1038/nprot.2015.065
11. Virgili J, Lebbadi M, Tremblay C, St-Amour I, Pierrisnard C, Faucher-Genest A, Emond V, Julien C, Calon F (2018) Characterization of a 3xTg-AD mouse model of Alzheimer's disease with the senescence accelerated mouse prone 8 (SAMP8) background. Synapse 72(4). https://doi.org/10.1002/syn.22025

Study of a Position Decoding Method Making Imaging Area Continuous for a Planar Positron Imaging Probe

Hsin-Chin Liang, Chen-Han Cheng, and Hsiang-Ning Wu

1 Introduction

Due to population aging became serious in the recent decades, early diagnosis of neurodegenerative diseases have been noticed its clinical need. In such need, several PET tracers and their clinical trials have been showing promising results and early diagnosis potentials. Therefore, a project of developing a planar PET scanner for brain function imaging was raised. In our current design, the planar imaging probe is equipped with an imaging area of 151 × 151 mm^2, which obviously cannot cover a whole brain. Therefore, a sliding scan scheme is arranged for the brain scanner, as shown in Fig. 1. Due to the need of imaging probe sliding, it is required the whole imaging area of the proposed imaging probe to be successive. However, from the previous test result, as shown in Fig. 2, a 2D map of the imaging probe, lack of 2 rows/columns of crystals in the cross-over regions was observed. It is because of the conventional Anger logic not able to deal with the information from neighboring detectors [1]. Therefore, there is an urgent necessity for our group to build a position decoding algorithm capable of solving crossover problems between detectors [2], to make our imaging probe have a whole successive imaging area.

2 Materials and Methods

The proposed planar PET imaging probe is composed of 9 imaging detectors, connecting with a plate of 2.5-mm-thick window laying between the scintillation and photonics layer, shown in Fig. 3. Each detector is composed of a scintillation

H.-C. Liang (✉) · C.-H. Cheng · H.-N. Wu
Institute of Nuclear Energy Research/Health Physics Division, Taoyuan, Taiwan
e-mail: sjingliang@iner.gov.tw

© The Author(s), under exclusive license to Springer Nature Switzerland AG 2022

K.-P. Lin et al. (eds.), *Future Trends and Challenges of Molecular Imaging and AI Innovation*, Springer Proceedings in Physics 272,
https://doi.org/10.1007/978-3-030-92786-8_9

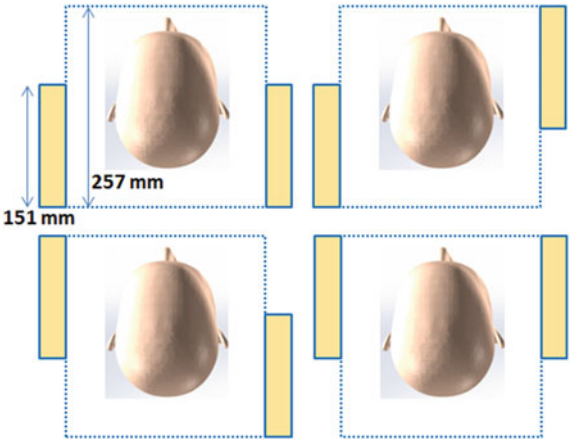

Fig.1 Sliding scan strategy for brain PET imaging

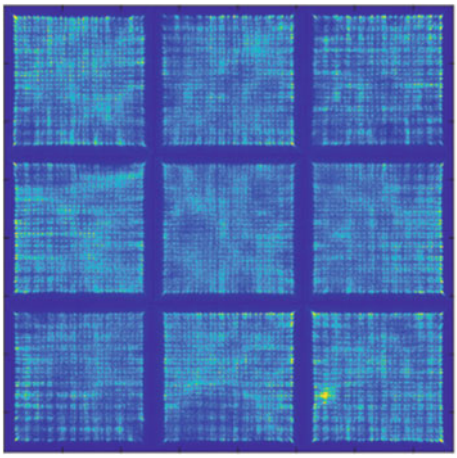

Fig.2 Crystal 2D map obtained with using Anger logic

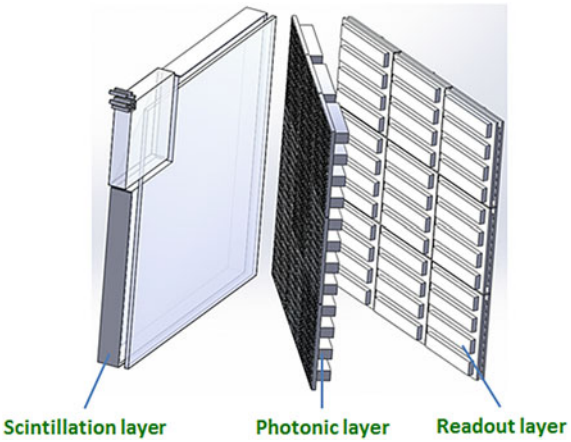

Fig.3 Layout scheme of the planar PET camera

layer composing of 31 × 31, 1.51 × 1.51 × 10 mm^3-pixel LYSO crystal array, a 144-pixels photonic layer (SensL ArrayC-30035–144-PCB), and a 1:12 linear weighting readout circuit. In this study, upper-left 4 detectors of the imaging probe were served for solution study. Although in such layout, detectors seem to be independent with each other, the transparent window does spread scintillation photons to neighbor detectors, and thus forming crossover regions when detectors leaning together. Due to lack of inter-detectors information consideration, conventional Anger logic is not capable of separating crystals in the crossover regions. Instead of the Anger logic, the ratios of the 4 acquired weighted signals, i.e. x+/x− for calculating x-positions and y+/y− for calculating y-positions, from each detector are applied to decode the event positions. Due to the pre-designed signal weights for the readout, a position mapping curve can be fitted for the weighted signal ratios (i.e. x+/x− and y+/y−),as shown in Fig. 4. Such curve is applied for position decoding of event signals to event positions (crystal 2D maps). In the proposed method, weighted signal ratios are also served as a detection of crossover region event occurrence. As shown in Fig. 5, a statistical histogram of the weighted signal ratios (x+/x−) of detector 1 (upper-left corner one).

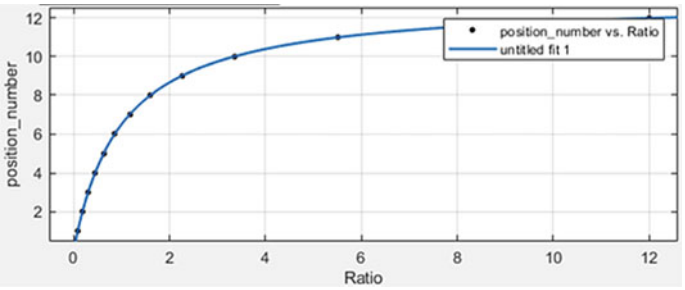

Fig. 4 Fitted curve for detector signals to find event positions

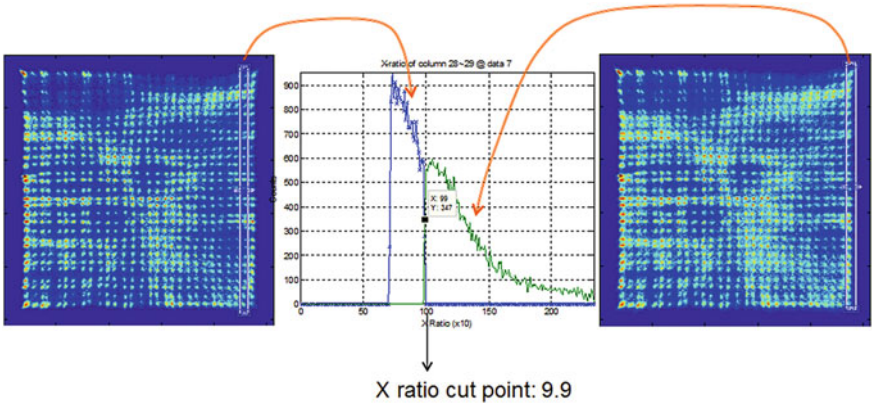

Fig. 5 A statistical histogram of the weighted signal ratios (x + /x-) of a detector

It is clearly seen that the ratio value of 9.9 can be served as a distinguishing boundary. When the weighted signal ratios approaching the ends of the mapping curve, in our case they are (larger than) 9.9 and (smaller than) 0.095, it indicates that the incident events occurred in crossover region crystals, and neighbor detector signals needed to be taken into account. For such events, position correction calculations that take neighbor detector information into account are applied, as follows:

$$X_c = X + (E_{xn}/(E_x + E_{xn}))\Delta X$$
$$Y_c = Y + \left(E_{yn}/\left(E_y + E_{yn}\right)\right)\Delta Y$$

where (Xc, Yc) are corrected event position coordinates,

(X, Y) are the uncorrected position coordinates obtained from the position mapping curve,

E_{xn} is the neighbor detector x-branch energy, i.e. $E_{xn} = (x+)_n + (x-)_n$,

E_{yn} is the neighbor detector y-branch energy, i.e. $E_{yn} = (y+)_n + (y-)_n$,

E_x is the detector x-branch energy, i.e. $E_x = (x+) + (x-)$,

E_y is the detector y-branch energy, i.e. $E_y = (y+) + (y-)$,

ΔX and ΔY are pixel numbers which represent the size of a photonic pixel in the crystal 2D map, 25 for both ΔX and ΔY is applied in the current calculations.

In such position decoding algorithm (i.e. weighted signal ratio driven), it is expected to recover the event counts of the crossover region crystals.

3 Results and Discussions

From a crystal 2D map of the proposed imaging probe exposed to a flood Cs-137 source, shown in Fig. 6, it is observed that 2 rows/columns of crystals are missing in

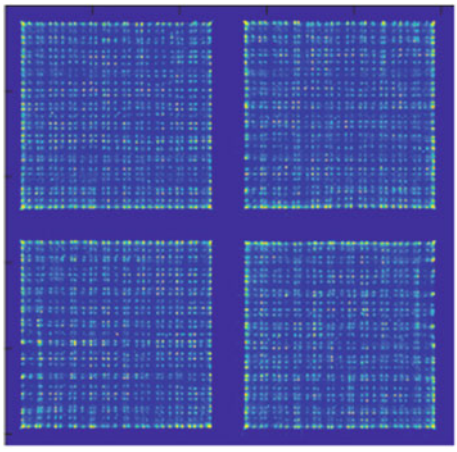

Fig. 6 Flood exposure resultant 2D map obtained with using Anger logic

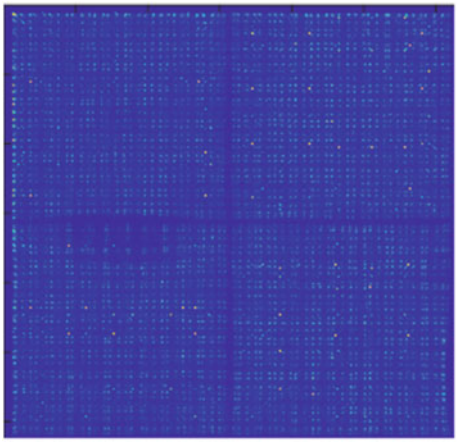

Fig. 7 Crystal 2D map with applying the proposed ratio-driven position decoding. Recovering the crossover region counts is observed

the cross-over regions, and thus makes a countable crystal array of 29 × 29 for each detector, and for the upper-left 4 detectors, it is 58 × 58. Compare to the designed array size of 62 × 62, besides 2-rows/columns loss at the peripheral region, which does not affect continuity of the imaging area, the imaging probe did exhibit 2-rows/columns loss at its center region. With applying the proposed position decoding calculation to the same imaging probe for the same experimental data, the resultant 2D map is shown in Fig. 7. It is observed that the lost 2 rows/columns of crystals in the cross-over regions are recovered, and well separations among these crystals in the 2D map are shown. It thus makes the crystal array countable element to be 30 × 30 ~ 32 × 32. And for the whole probe, it is 61 × 61. Although the loss at the peripheral region still there, the loss crystals at the probe center region are indeed recovered. It implies that the proposed new position decoding calculations work for making the imaging area our probe successive.

4 Conclusions

In this study, a set of position decoding calculations is built, and its effectiveness of making the imaging area successive is proved. The crystal array designed for our probe is 93 × 93, with the proposed calculations applying, a countable array of 91 × 91 is expected, which means the whole imaging-area of our probe is successive with the same size pixels. However, the crystals in the peripheral edges are still missing. Therefore, the following efforts will be put on searching a similar way of position decoding calculations to recover the edge rows/columns.

Acknowledgements The project budget is from AEC (Atomic Energy Commission) of the Executive Yuan. The authors would like to thank Dr. Yuan in health physics division, INER for offering

and preparing flood Cs-137 radioactive sources, which are the experimental data sources of the proposed research.

Conflict of Interest The authors declare that they have no conflict of interest.

References

1. Liang HC, Jan ML, Su JL et al (2009) Development of an LYSO based gamma camera for positron and scinti-mammography. J Instrum JINST 4:P08009
2. Liang H-C, Jan M-L, Su J-L (2012) Development of a pixelated detector for clinical positron and single-photon molecular imaging. J Med Biol Eng. https://doi.org/10.5405/jmbe972

The Evaluation of Novel PET/CT Motion Correction Technique Applied in Lung Cancer Patients

Yi-Lun Chen, Bang-Hung Yang, I-Ling Shih, and Wen-Sheng Huang

1 Introduction

Recently, 18F-fluoro-2-deoxyglucose (18F-FDG) Positron Emission Tomography/Computed Tomography (PET/CT) not only offering tumor metabolism image but also morphological image simultaneously is considered a precise modality for the evaluation of lung cancer. One of the important indications is that PET/CT can effectively evaluate the malignancy of solitary pulmonary nodules and metastatic lesions. The excellent detection abilities make PET/CT scan become a clinical examination for lung cancer patients [1, 2].

However, Respiratory motion is one of the main factors significantly impacting PET/CT image quality. Motion artifacts degrade PET image quality and lead to reduction in lesion detectability, especially in lung lesions. Quantification accuracy is also impacted by respiratory motion artifacts, resulting in reduction in standard uptake value (SUV) and overestimation in lesion volume [3, 4]. These artifacts can be eliminated by 4D gated PET scan. In the past, 4D gated PET acquired data by utilizing an external gating device, e.g., elastic chest belt, Real-time Position Management (RPM) system, abdominal compression device, respiratory temperature sensor, and

Y.-L. Chen (✉) · B.-H. Yang (✉) · W.-S. Huang
Taipei Veterans General Hospital, National PET/Cyclotron Center and Department of Nuclear Medicine, Taipei, Taiwan
e-mail: ylchen47@vghtpe.gov.tw

B.-H. Yang
e-mail: bhyang@vghtpe.gov.tw

Y.-L. Chen · B.-H. Yang
Taipei Association of Radiological Technologists, Taipei, Taiwan

I.-L. Shih
GE Healthcare, Taipei, Taiwan

© The Author(s), under exclusive license to Springer Nature Switzerland AG 2022

K.-P. Lin et al. (eds.), *Future Trends and Challenges of Molecular Imaging and AI Innovation*, Springer Proceedings in Physics 272,
https://doi.org/10.1007/978-3-030-92786-8_10

spirometer [5, 6]. Setting those external gating devices are not only time-consuming and inefficient but also increasing technologist radiation dose.

In current, a device-less data driven gated (DDG) technique (Motion free®, GE Healthcare, Waukesha, WI) was launched. It is used for deriving respiratory information from the coincidence events in each FOV. Motion is automatically detected and corrected using quiescent phase gating as the Q.Static algorithm. Then, the motion corrected images are generated. Motionfree® is an algorithm based upon principal component analysis (PCA) that determines the magnitude of respiratory impact to the data. The method analyzes the coincidence data without the need for any external device [7–10]. A respiratory waveform is derived from the PET list-mode data, and the waveform is used to derive per-cycle triggers. These triggers enable subsequent gated data processing using the existing Q.Static acquisition mode.

The Q.Static is designed to be a phase-based gating method that extracts a fraction of PET data from the end-expiration quiescent portions of patient breathing cycles. The relatively stable breathing period is acquired, in order to reduce respiratory motion. The suspicious motion area is set as the Q.Static scan mode. The respiratory motion R value was calculated in real-time. When the calculated R value was over a configured threshold, acquired time of the bed was prolonged, enabling comparable statistics as in static acquisition.

The purpose of this study was to assess that whether the novel data driven gated (DDG) technique Q.Static could improve PET respiratory motion blur in lung cancer cases.

2 Materials and Methods

A. Patient population

The current study was a retrospective study from October 2019 to February 2020. 204 patients with lung cancer were recruited. This group consisted of 105 men and 99 women with a mean age of 65.2 ± 12.6 years (range: 32–92 years) and a mean BMI of 23.7 ± 3.6 kg/m^2(range: 13.4–38.1). All patients were injected 3.7 MBq/kg ± 10% of ^{18}F-FDG after fasting a least 4 h and serum glucose concentration was less than 200 mg/dl. The PET/CT scan was obtained 60 min after injection.

B. Imaging protocol

All PET/CT scans were performed with Discovery MI DR (GE Healthcare, Waukesha, WI, USA). Acquisition protocols used clinical routine oncology whole body PET/CT protocol. Patients were requested to breathe steadily and regularly in whole body scan time. Free-breathing CT acquisition parameter was: 120 kVp, smart mA(range 30–130 mA), pitch of 0.984:1, rotation time 0.5, and 3.75 mm slice thickness (with slice increment 3.27 mm). The PET were acquired 2 min/bed from head to thigh with list-mode and time of flight (ToF) technique.

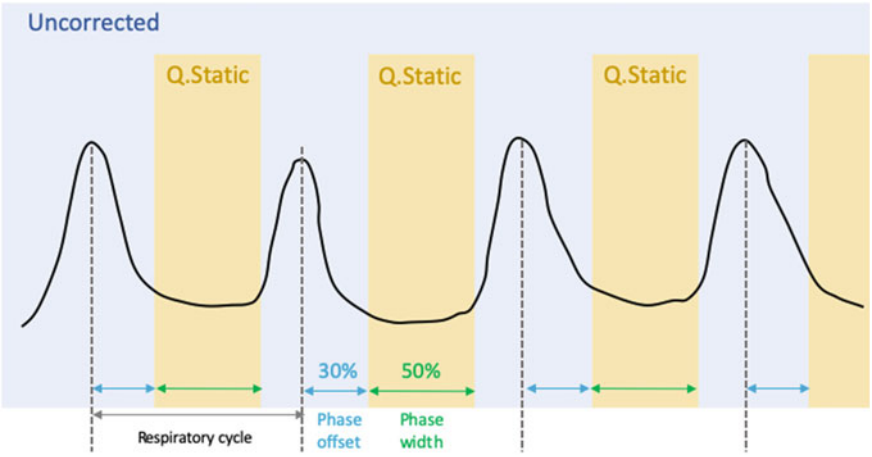

Fig. 1 Typical patient respiratory curve with a longer quiescent phase with little respiratory movement. The default Phase width is 50% and default phase offset is 30%

Data Driven Gated (DDG) Q.Static arranged to detect at Bed 3–5 which was covered whole thorax and upper abdomen. The respiratory motion R value was set 15.0 as threshold. The Q.Static parameter was modified that the phase width set 50% and phase offset set 30% which provided by the manufacturer (Fig. 1). When patients' respiratory motion R value were over than threshold, Q.Static triggered and took double acquired time to match the same image quality. At the same time, we recorded the Q.Static triggered bed for statistics.

Then we reconstructed two types of images: one was the Q.Static correction and the other was the non-Q.Static correction. Both of images used the same CT attenuation correction and the same PET reconstruction algorithm: 3-D VUE Point FX (2 iterations, 24 subsets and filter cutoff 5 mm), Sharp IR(PSF).

III. Image analysis

Image analysis was performed by AW server 3.2(GE healthcare, Waukesha, WI). Both images were drawn the 3D volume of interest(VOI) in the same size and measured the SUV_{max}、 SUV_{mean} and lesion volume. The VOI was semi-automatically drawn with a threshold 50% of SUV_{max} isocountour for each lung lesion so that reduces artificial mistakes. If the patients had more than one lesion, only the highest SUV_{max} one was included in this study.

IV. Statistical analysis

The VOI measured data were presented with mean ± standard deviation. Patients' characteristics and DDG Q.Static activation were assessed by Chi-square test. The comparison of measured data between the Q.Static corrected images and the uncorrected images was performed by Paired sample t-test. And the variation of SUV value which was corrected by the Q.Static and lesion volume were used simple linear regression analysis. P value < 0.05 was considered statistically significant.

3 Results

Table 1 shows the statistic of DDG triggered bed of all patients. The 131 out of 204 (74%) patients whose R value were over the threshold and been triggered by DDG procedure. Most of the triggered beds were bed 4 or bed 5. These beds almost covered lower lung and diaphragm area which are considered the most obvious respiratory motion area. On the contrary, Bed 3 covering the upper lung was seldom triggered in this study. We collected the relation between the DDG trigger and patients' characteristics. Patients' sex and BMI were not significant related to activate DDG procedure (Table 2). According to that, the DDG detection is only affected by breathing.

There were 131 patients mentioned above and only 60 patients' lesions located at triggered beds. These lesions were drawn VOIs and measured SUV value and volume in order to assess the Q.Static corrected ability. Table 3 shows the quantitative value of the Q.Static corrected and uncorrected images. The mean of SUV_{max} and the mean of SUV_{mean} in the Q.Static data were significantly higher than the Q.Static uncorrected data (both $P < 0.05$). Furthermore, the mean of volume in Q Static data were significantly less than uncorrected data ($P < 0.05$). The Q.Static corrected data were increased up 8.91% in SUV_{max} and 8.98% in SUV_{mean}, but decreased

Table 1 The statistic of the Q.Static triggered bed in all patients

Triggered bed	Case	Percentage (%)
Bed 3 only	0	0
Bed 4 only	37	18
Bed 5 only	45	22
Bed 3,4	0	0
Bed 3,5	0	0
Bed 4,5	46	23
Bed 3,4,5	3	1
NA	73	36
Total	204	100

Table 2 Patients' characteristic and DDG trigger

		N(%)	DDG Trigger		Significance
			yes	no	
Sex	Male	105(51.5)	67(51.1)	38(52.1)	P = 0.9
	Female	99(48.5)	64(48.9)	35(47.9)	
BMI	<18	11(5.4)	8(6.1)	3(4.1)	P = 0.196
	18–24	103(50.5)	60(45.8)	43(58.9)	
	>24	90(44.1)	63(48.1)	27(37)	

Table 3 The quantitative values and statistical significance

	SUV_{max}	SUV_{mean}	Lesion volume
Corrected images	8.77 ± 5.09	5.85 ± 3.52	4.83 ± 6.45
Uncorrected images	8.22 ± 5.04	5.47 ± 3.46	5.84 ± 7.67
Mean difference	0.54 ± 0.7	0.37 ± 0.49	−1 ± 2.11
Mean percentage difference (%)	8.91 ± 11.03	8.98 ± 10.96	−15.73 ± 20.02
Significance	P = 0.0000	P = 0.0000	P = 0.0002

down 15.73% in lesion volume. The variation of SUV_{max} and SUV_{mean} were not significantly related to lesion size ($R^2 = 0.0034$; $R^2 = 0.007$, respectively).

Figure 2 is the one interest case. According to the figure, there was one lesion in the left lower lobe. And we found that the lesion was presented blur and not concentrated in the uncorrected image. A part of lesion covered to spleen might cause a mistake. In contrast, the Q.Static corrected image showed a clear and sharp lesion. Furthermore, the quantitative data in this case was SUV_{max} increased from 8.44 to 9.82(16.35%); SUV_{mean} increased from 5.61 to 6.8(21.21%); volume reduced from 1.03 cm^3 to 0.66 cm^3(-35.92%). In other words, the Q.Static corrected image can provide better image quality and accurate quantitative data.

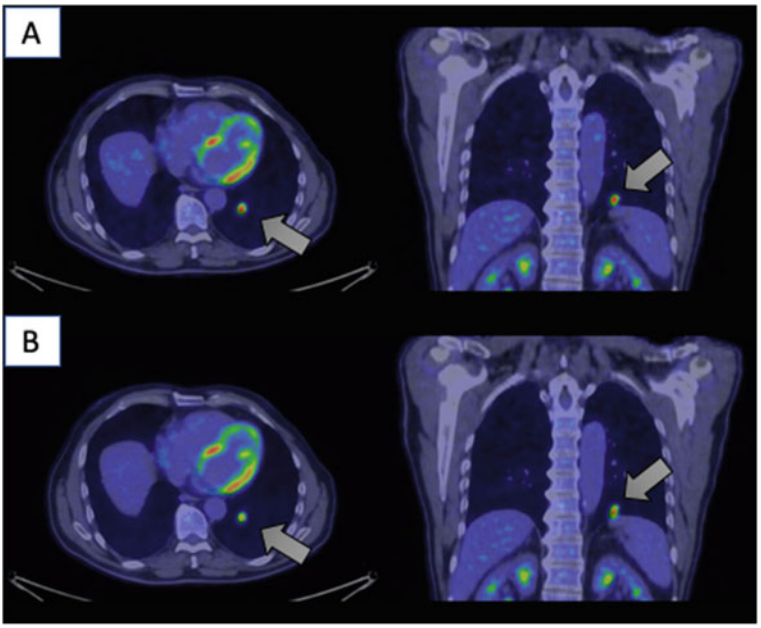

Fig. 2 A 53-year-old Male with a LLL Lung lesion. The upper row (A) was the Q.Static corrected image and the lower row (B) was uncorrected image. The arrow was shown the lesion. There were obvious blur and lengthen lesion in uncorrected image

But not all cases presented the same results. Some cases presented SUV decreasing or lesion volume increasing. We think there are two possible reasons that affect the Q.Static method. First, the lesion is located across two acquisition beds or at the overlapped area. When only one acquisition bed activates DDG, only the part of lesion is corrected and the other part is not. Thus, the quantitative values are affected. Secondly, the patient breathes irregularly and unstably. The poor breathing method has an effect on Q.Static calculation, thus causing wrong correction.

4 Conclusion

This study demonstrated that the DDG PET acquisition provides an easier way to correct motion artifacts in PET/CT scan. The quantitative SUV values increased, and lesion volumes decreased.

Acknowledgements Authors would like to express their gratitude to all patients who kindly participated in this study. And they also thank their colleague for their assistance during the study process and the imaging recruitments.

Conflict of Interest There are no conflicts of interest.

References

1. Hochhegger B, Alves GR, Irion KL et al (2015) PET/CT imaging in lung cancer: indications and findings. J Bras Pneumol 41:264–274
2. Greenspan BS (2017) Role of PET/CT for precision medicine in lung cancer: perspective of the society of nuclear medicine and molecular imaging. Transl Lung Cancer Res 6:617
3. Nehmeh SA, Erdi YE, Ling CC et al (2002) Effect of respiratory gating on quantifying PET images of lung cancer. J Nucl Med 43(7):876–881
4. Erdi YE, Nehmeh SA, Pan T et al (2004) The CT motion quantitation of lung lesions and its impact on PET-measured SUVs. J Nucl Med 45(8):1287–1292
5. Pepin A, Daouk J, Bailly P et al (2014) Management of respiratory motion in PET/computed tomography: the state of the art. Nucl Med Commun 35:113–122
6. Huang TC, Wang YC, Chou YR et al (2014) Respiratory motion reduction in PET/CT using abdominal compression for lung cancer patients. PLoS One 9(5):e98033
7. Walker MD (2019) Evaluation of data-driven respiratory gating waveforms for clinical PET imaging. EJNMMI Res 9(1):1
8. Thielemans K (2011) Device-less gating for PET/CT using PCA
9. Nehmeh SA(2004) Quantitation of respiratory motion during 4D-PET/CT acquisition. Med Phys 31(6):1333–1338
10. Walker MD, Bredley KM, McGowan DR (2018) Evaluation of principal component analysis-based data-driven respiratory gating for positron emission tomography. Br J Radiol 91(1058):20170793

Evaluation of Radiolabeling PSMA-Targeted Long Circulating Peptide as a Theranostic Agent in Human Prostate Tumor-Bearing Mice

Ming-Hsin Li, Ming-Wei Chen, Wei-Lin Lo, Yuan-Ruei Huang, Sheng-Nan Lo, Shih-Ying Lee, Su-Jung Chen, Shih-Wei Lo, Shih-Min Wang, and Chih-Hsien Chang

1 Introduction

Prostate-specific membrane antigen (PSMA) is expressed higher in prostate tumors and metastases than most normal tissue. This pathological expression pattern leads it to be a target for endoradiotherapy of prostate cancer [1, 2]. The albumin binding structure has modified to the target molecule lets the kinetic of the molecule in the blood to change. In addition, extending the circulating-time of drugs in the body is a method to enhance the efficacy of drugs [3].

In this study, we have developed a novel long-circulation PSMA-targeted molecule, MH-PC-AB-56, which PSMA binding motif (PSMA-617 structure without DOTA) covalently linked with albumin binder (4-p-tolylbutyric acid), and conjugated DOTA chelator, and labeled with radionuclide ^{111}In or ^{177}Lu. We investigated the tumor binding affinity and biodistribution by molecular imaging of radiolabeled MH-PC-AB-56 peptide. The major objective of this study was to evaluate the potential advantage of MH-PC-AB-56 in the theranostic application by NanoSPECT image.

M.-H. Li (✉) · M.-W. Chen · W.-L. Lo · Y.-R. Huang · S.-N. Lo · S.-Y. Lee · S.-J. Chen · S.-W. Lo · S.-M. Wang · C.-H. Chang
Isotope Application Division, Institute of Nuclear Energy Research, Taoyuan, Taiwan
e-mail: mhli@iner.gov.tw

C.-H. Chang
e-mail: chchang@iner.gov.tw

© The Author(s), under exclusive license to Springer Nature Switzerland AG 2022

K.-P. Lin et al. (eds.), *Future Trends and Challenges of Molecular Imaging and AI Innovation*, Springer Proceedings in Physics 272,
https://doi.org/10.1007/978-3-030-92786-8_11

2 Materials and Methods

A. Cell culture and tumor-bearing mice

The PSMA positive prostate cancer cell line, LNCaP, was obtained from Bioresource Collection and Research Center. Cells were grown in RPMI 1640 supplemented with 10% (v/v) fetal bovine serum, 100 units/mL penicillin and 100 μg/mL streptomycin in a humidified incubator at 37 °C under 5% CO_2. Six-week-old male BALB/c nude mice were obtained from BioLASCO Taiwan Co., Ltd. Mice were housed in a 12 h light cycle at 22 °C, with food and water provided ad libitum. Cells (1×10^7) was implanted right front leg of BALB/c nude mice for LNCaP tumor xenografts. The mice underwent NanoSPECT/CT study when the tumor volume reached approximately 200–600 mm^3. The animal experimental protocols were approved by INER Institutional Animal Care and Use Committee.

B. Radiolabeling with indium-111 and lutetium-177

Indium (^{111}In) chloride in 0.01 N HCl was generated from INER (Taoyuan, Taiwan). Lutetium (^{177}Lu) chloride in 0.04 N HCl purchased from ITM Medical Isotopes GmbH (Garching/Munich, Germany). The peptide (MH-PC-AB-56 and PSMA-617) purchased from Ontores Biotechnologies Co., Ltd. (Zhejiang China).

For ^{111}In-MH-PC-AB-56 labeling, the 13.9 nmole peptide (in DMSO) was incubation with 0.23–0.26 GBq $^{111}InCl_3$ in 1 M sodium acetate solution (pH 6.0) at 95°C for 15 min. The radiochemical efficiency analyzed by thin-layer chromatography (TLC) with 10% methanol and high-performance liquid chromatography (HPLC). For ^{177}Lu-MH-PC-AB-56 labeling, the 13.9 nmole peptide (in DMSO) was incubation with 0.47–0.51 GBq $^{177}LuCl_3$ in 0.4 M sodium acetate solution (pH 5.0) at 95°C for 30 min. The radiochemical efficiency analyzed by TLC with 0.1 M citric acid and HPLC. For ^{177}Lu-PSMA-617 labeling, the 19.2 nmole peptide (in water) was incubation with 0.47–0.51 GBq $^{177}LuCl_3$ in 0.4 M sodium acetate solution (pH 5.0) at 95°C for 30 min. The radiochemical efficiency analyzed by TLC with 0.1 M citric acid and HPLC. The specific activity for ^{111}In-MH-PC-AB-56, ^{177}Lu-MH-PC-AB-56 and ^{177}Lu-PSMA-617 in the range of 16.5–18.7 GBq/μmole, 33.8–36.7 GBq/μmole and 24.5–26.6 GBq/μmole, respectively.

The radiolabeled peptides were measured using a radioactive scanner (AR-2000 radio-TLC Imaging Scanner, Bioscan, France) and radio-HPLC with UV detector (280 nm) and radio detector. The column was waters T3 C18 column (3.5 μm, 80 Å, 4.6 × 250 mm). The flow rate was 0.8 mL/min with the gradient mobile phase going from 80% A buffer (0.1% TFA in water) and 20% B buffer (0.1% TFA in acetonitrile) to 90% B buffer within 10 min for ^{111}In-MH-PC-AB-56. The flow rate was 1.0 mL/min with the gradient mobile phase going from 95% A buffer (0.1% TFA in water) and 5% B buffer (0.1% TFA in acetonitrile) to 95% B buffer within 10 min for ^{177}Lu-MH-PC-AB-56. The flow rate was 1.0 mL/min with the gradient mobile phase going from 80% A buffer (0.1% TFA in water) and 20% B buffer (0.1% TFA in acetonitrile) to 60% B buffer within 10 min for ^{177}Lu-PSMA-617.

C. In vitro stability study

The stability of ^{111}In-MH-PC-AB-56 evaluated by incubation with normal saline (volume ratio 1:1) at room temperature or human serum (volume ratio 1:19) at 37°C [4]. The radiochemical purity determined by TLC and HPLC analysis at desired times (0, 1, 4, 24, 48, 72 and 96 h). The serum sample was prepared with acetonitrile/water solution and centrifuged at 13,000 rpm 2 min, then analyzed the supernatant by HPLC.

The stability of ^{177}Lu-MH-PC-AB-56 evaluated by incubation with normal saline (volume ratio 1:1) at room temperature. The radiochemical purity determined by HPLC analysis at desired times (0, 1, 2, 3, 4, 5, 6, 7, 8 and 24 h).

D. NanoSPECT/CT imaging

The procedure for NanoSPECT/CT imaging has been described, previously [5]. NanoSPECT and X-ray images were acquired using a NanoSPECT/CT plus scanner system (Mediso Medical Imaging Systems; Budapest, Hungary). The mice was anesthetized with 1–2% isoflurane during the imaging acquisition. NanoSPECT imaging was acquired using nine multipinholes gamma-detectors and high-resolution collimators. The energy window was set at 171 and 245 keV ± 10%, the image size was set at 256 ± 256, and the field of view of 60 mm × 100 mm. Each mouse was tail-vein injected with 19.4–20.7 MBq of radiolabeled peptide and scanned for 1 h, 4 h, 24 h, 48 h, 72 h and 96 h.

For calculating uptake value at an interesting organ of ^{111}In-MH-PC-AB-56 and ^{177}Lu-MH-PC-AB-56, the images of SPECT reconstructed by HiSPECT NG software (Scivis GmbH, Germany) and fused with CT datasets using InVivoScope software (Bioscan Inc.). Then, all data processed by PMOD Version 3.3 (PMOD Technologies Ltd., Zurich, Switzerland). Volumes of Interest (VOIs) drawn encompassing the tumor and reference source on the corresponding CT images. The VOIs transferred to SPECT images, and the count values of the tumor and reference source derived. The radioactivity of reference sources were 0.8 MBq ^{111}In and 1.3 MBq ^{177}Lu.

E. Statistics

Results presented as mean and standard deviation (Mean ± SD). The distribution correlation between ^{111}In-MH-PC-AB-56 and ^{177}Lu-MH-PC-AB-56 was analyzed by Pearson correlation coefficient (r) using IBM® SPSS® Statistics software version 19 [5].

3 Results

A. Radiolabeling efficiency of MH-PC-AB-56

The labeling efficiency of ^{111}In-MH-PC-AB-56 was 98.27 ± 1.29% and 99.09 ± 0.38% by TLC and HPLC analysis, respectively. In TLC, free ^{111}In was at origin front (Rf. approximately 0.000) and ^{111}In-MH-PC-AB-56 was at solvent front (Rf.

approximately 0.917) with 10% methanol as running buffer. The retention time of ^{111}In-MH-PC-AB-56 was 8.569 ± 0.010 min in radio detector by HPLC.

The labeling efficiency of ^{177}Lu-MH-PC-AB-56 was over 99.99% and 98.87 ± 0.73% by TLC and HPLC analysis, respectively. In TLC, free ^{177}Lu was at origin front (Rf. approximately 1.023) and ^{177}Lu-MH-PC-AB-56 was at solvent front (Rf. approximately 0.015) with 0.1 M citric acid as running buffer. The retention time of ^{177}Lu-MH-PC-AB-56 was 8.587 ± 0.262 min in radio detector by HPLC.

The labeling efficiency of ^{177}Lu-PSMA-617 was over 99.99% and 98.68% by TLC and HPLC analysis, respectively. In TLC, free ^{177}Lu was at solvent front (Rf. approximately 1.045) and ^{177}Lu-PSMA-617 had Rf. 0.435 with 0.1 M citric acid as eluted buffer. The retention time of ^{177}Lu-PSMA-617 was 8.247 min in radio detector HPLC.

B. In vitro stability study of ^{111}In-MH-PC-AB-56

The radio-purity of ^{111}In-MH-PC-AB-56 was greater than 95% within 96 h incubation in normal saline or human serum (Table 1).

C. In vitro stability of ^{177}Lu-MH-PC-AB-56 in normal saline

The stability of ^{177}Lu-MH-PC-AB-56 in normal saline was greater than 95% within 8 h incubation by HPLC (Table 2).

D. NanoSPECT/CT imaging

The images showed that both radiolabeled ^{111}In/^{177}Lu-MH-PC-AB-56 and ^{177}Lu-PSMA-617 were excreted mainly via the renal pathway with higher renal retention especially at early time points 1 h and 4 h injection. Higher and sustained tumor uptake was observed for radiolabeled MH-PC-AB-56 up to 96 h by imaging (Fig. 1).

The accumulated activity of radiolabeled ^{111}In/^{177}Lu-MH-PC-AB-56 in the tumor at time points was calculated from the images created by drawing the Volume of

Table 1 In vitro stability of ^{111}In-MH-PC-AB-56 at different times after incubation in normal saline at room temperature or human serum at 37°C

Time (h)	Normal Saline		Human Serum	
	TLC (%)	HPLC (%)	TLC (%)	HPLC (%)
0	99.5 ± 0.9	98.8 ± 1.1	98.3 ± 0.8	98.8 ± 0.3
1	98.6 ± 1.3	97.9 ± 1.2	98.2 ± 0.9	98.9 ± 0.6
4	98.7 ± 1.2	97.0 ± 0.8	98.8 ± 1.1	99.2 ± 0.1
24	99.2 ± 0.7	97.8 ± 0.8	98.0 ± 1.0	99.0 ± 0.4
48	99.6 ± 0.8	97.4 ± 1.1	98.3 ± 0.6	99.0 ± 0.3
72	99.0 ± 0.8	96.6 ± 0.7	98.1 ± 0.5	98.7 ± 0.6
96	96.9 ± 2.8	98.5 ± 0.9	95.5 ± 0.8	98.8 ± 0.3

(mean ± SD, n = 3)

Table 2 In vitro stability of ^{177}Lu-MH-PC-AB-56 at different times after incubation in normal saline at room temperature (mean ± SD, n = 3)

Time (h)	Normal Saline HPLC (%)
0	99.5 ± 0.6
1	98.0 ± 0.9
2	96.6 ± 2.7
3	96.9 ± 1.0
4	94.5 ± 2.5
5	96.2 ± 1.4
6	94.9 ± 1.8
7	94.3 ± 1.1
8	94.4 ± 1.2

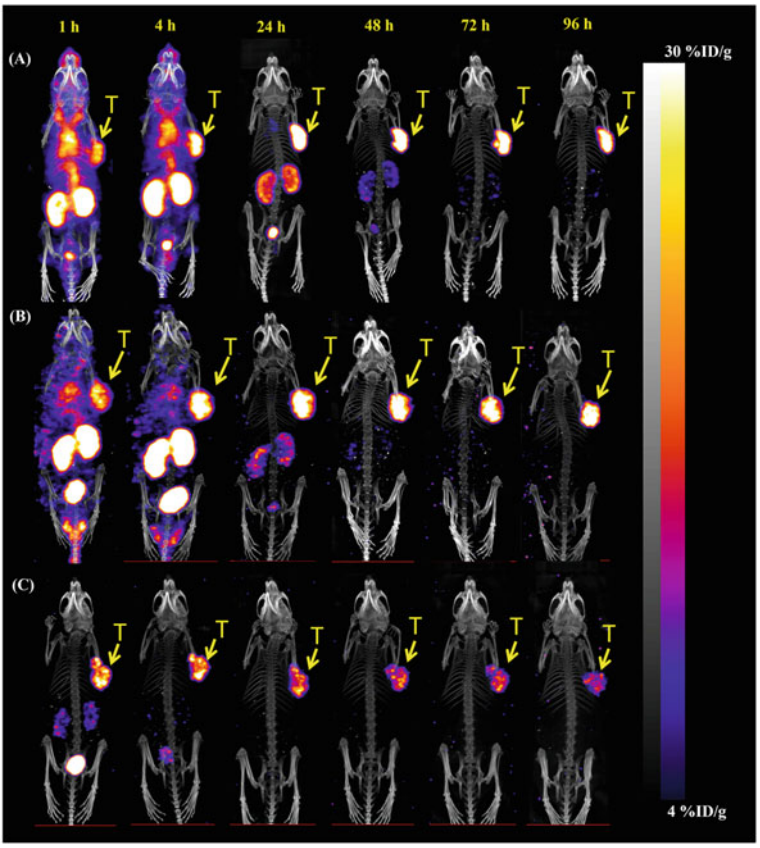

Fig.1 Comparison of NanoSPECT/CT images of ^{111}In-MH-PC-AB-56 (**a**), ^{177}Lu-MH-PC-AB-56 (**b**) or ^{177}Lu-PSMA-617 (**c**) targeting LNCaP tumor-bearing mice. The images were acquired at 1, 4, 24, 48, 72, and 96 h after injection

Table 3 Comparison of tumor uptake of ^{111}In-MH-PC-AB-56 and ^{177}Lu-MH-PC-AB-56 analyzed by NanoSPECT image

Time (h)	^{111}In-MH-PC-AB-56 (%ID/g)	^{177}Lu-MH-PC-AB-56 (%ID/g)
1	19.79 ± 2.27	12.91 ± 2.69
4	27.32 ± 2.85	17.98 ± 3.20
24	43.79 ± 6.55	22.08 ± 6.63
48	35.48 ± 4.53	21.56 ± 4.90
72	29.77 ± 4.30	22.80 ± 5.29
96	25.06 ± 3.77	23.41 ± 5.18

Interest (VOI) using the standard source as a point of reference. The image semi-quantitative analysis of ^{111}In-MH-PC-AB-56 in the tumor at 1 h, 4 h, 24 h, 48 h, 72 h and 96 h after injection was 19.79 ± 2.27, 27.32 ± 2.85, 43.79 ± 6.55, 35.48 ± 4.53, 27.77 ± 4.30, and 25.06 ± 3.77%ID/g, respectively (Table 3). The image semi-quantitative analysis of ^{177}Lu-MH-PC-AB-56 in the tumor at 1 h, 4 h, 24 h, 48 h, 72 h and 96 h after injection was 12.91 ± 2.69, 17.98 ± 3.20, 22.08 ± 6.63, 21.56 ± 4.90, 22.80 ± 5.29, and 23.41 ± 5.18%ID/g, respectively (Table 3). The trend of tumor uptake of ^{111}In-MH-PC-AB-56 is similar to ^{177}Lu-MH-PC-AB-56 before 24 h injection. After 24 h injection, the tumor uptake of ^{111}In-MH-PC-AB-56 was slightly declining, but the tumor uptake of ^{177}Lu-MH-PC-AB-56 sustained last for at least 96 h.

Pearson correlation analysis of tumor uptake of ^{111}In-MH-PC-AB-56 and ^{177}Lu-MH-PC-AB-56 by semi-quantification image analysis was moderated degree ($r = 0.576$). There was a high correlation of liver, kidney, and muscle of ^{111}In-MH-PC-AB-56 and ^{177}Lu-MH-PC-AB-56 with value 0.960 (Table 4), 0.960 (Table 5), and 0.940 (Table 6), respectively.

Table 4 Comparison of liver accumulation of ^{111}In-MH-PC-AB-56 and ^{177}Lu-MH-PC-AB-56 analyzed by NanoSPECT image (mean ± SD, n = 3)

Time (h)	^{111}In-MH-PC-AB-5 (%ID/g)	^{177}Lu-MH-PC-AB-56 (%ID/g)
1	9.89 ± 2.25	4.38 ± 1.22
4	8.31 ± 2.10	2.33 ± 0.51
24	1.84 ± 0.47	0.36 ± 0.11
48	0.53 ± 0.20	0.25 ± 0.09
72	0.32 ± 0.16	0.17 ± 0.05
96	0.23 ± 0.10	0.19 ± 0.02

Table 5 Comparison of kidney accumulation of ^{111}In-MH-PC-AB-56 and ^{177}Lu-MH-PC-AB-56 analyzed by NanoSPECT image (mean ± SD, n = 3)

Time (h)	^{111}In-MH-PC-AB-56 (%ID/g)	^{177}Lu-MH-PC-AB-56 (%ID/g)
1	37.62 ± 3.69	40.35 ± 4.89
4	39.66 ± 7.59	42.63 ± 20.14
24	16.40 ± 3.82	6.33 ± 3.51
48	6.15 ± 1.39	2.46 ± 1.39
72	3.19 ± 0.75	1.57 ± 0.95
96	2.02 ± 0.74	0.92 ± 0.68

Table 6 Comparison of muscle accumulation of ^{111}In-MH-PC-AB-56 and ^{177}Lu-MH-PC-AB-56 analyzed by NanoSPECT image (mean ± SD, n = 3)

Time (h)	^{111}In-MH-PC-AB-56 (%ID/g)	^{177}Lu-MH-PC-AB-56 (%ID/g)
1	6.58 ± 0.59	3.76 ± 1.15
4	6.70 ± 0.45	2.22 ± 0.84
24	1.29 ± 0.27	0.43 ± 0.23
48	0.41 ± 0.06	0.25 ± 0.07
72	0.21 ± 0.05	0.18 ± 0.07
96	0.17 ± 0.01	0.18 ± 0.01

4 Conclusions and Discussion

Many albumin binders (truncated Evan's blue, 4-(phenyl)butyric acid, 4-(p-bromophenyl)butyric acid, 4-(p-iodophenyl)butyric acid, 4-(p-chlorophenyl)butyric acid, 4-(p-fluorophenyl)butyric acid, 4-(p-methyl phenyl)butyric acid, and 4-(p-methoxyphenyl)butyric acid) had been used in modified PSMA-617 to enhance the circulating-time of PSMA-targeted drug to drawdown the accumulation of drug at kidney and improved tumor uptake [6]. We explored a novel linker lysine and 6-aminohexanoic acid not like PSMA-ALB-56 [7] only lysine or RPS [8] used PEG before. The structure is not only longer of length than lysine but also more lipophilic than PEG. In vitro stability study showed, the radiochemical purity of ^{177}Lu-MH-PC-AB-56 maintain to over 90% last at least 8 h without ascorbic acid addition. The SPECT image show that MH-PC-AB-56 labeled with dual-nuclide have a similar trend of metabolism or elimination organ, and demonstrated ^{177}Lu-MH-PC-AB-56 could improve tumor uptake than 177Lu-PSMA-617. These results let us know the tumor accumulated ability and elimination route of radiolabeled MH-PC-AB-56. These results indicated the ^{111}In/^{177}Lu-MH-PC-AB-56 owned the theranostic potency for diagnosis and therapy. The therapeutic efficacy, pharmacokinetics, and biodistribution would be further studied in the near future.

Acknowledgements We thanked the support from the Ministry of Economic Affairs, ROC with grant number 108-EC-17-A-22-1587.

Conflict of Interest The authors declare that they have no conflict of interest.

References

1. Rahbar et al (2018) Mol Imaging 17:1–9. https://doi.org/10.1177/1536012118776068
2. Langbein et al (2019) J Nucl Med 60:13S-19S. https://doi.org/10.2967/jnumed.118.220566
3. Kuo et al (2018) Mol Pharmaceutics 15:5183–5191. https://doi.org/10.1021/acs.molpharmaceut.8b00720
4. Lo et al (2020) Appl Radiat Isot 161:109126. https://doi.org/10.1016/j.apradiso.2020.109162
5. Chang et al (2007) Anticancer Res 27:2217–2226
6. Kuo et al (2020). J Nucl Med. https://doi.org/10.2967/jnumed.120.250738
7. Umbricht et al (2018) Mol Pharm 15:2297–2306. https://doi.org/10.1021/acs.molpharmaceut.8b00152
8. Kelly et al (2019) J Nucl Med 65:656–663. https://doi.org/10.2967/jnumed.118.221150